

Aerodynamic Design and Performance Analysis of Small Scale Horizontal Axis Wind Turbine with Different Blade Configurations

Aktham Sami Mohammad Mansi

Submitted to the
Institute of Graduate Studies and Research
in partial fulfillment of the requirements for the degree of

Master of Science
in
Mechanical Engineering

Eastern Mediterranean University
August 2021
Gazimağusa, North Cyprus

Approval of the Institute of Graduate Studies and Research

Prof. Dr. Ali Hakan Ulusoy
Director

I certify that this thesis satisfies all the requirements as a thesis for the degree of Master of Science in Mechanical Engineering.

Prof. Dr. Hasan Hacışevki
Chair, Department of Mechanical
Engineering

We certify that we have read this thesis and that in our opinion it is fully adequate in scope and quality as a thesis for the degree of Master of Science in Mechanical Engineering.

Asst. Prof. Dr. Devrim Aydın
Supervisor

Examining Committee

1. Prof. Dr. Hasan Hacışevki

2. Assoc. Prof. Dr. Hüseyin Çamur

3. Asst. Prof. Dr. Devrim Aydın

ABSTRACT

Wind energy has emerged as one of the mostly utilized renewable energy sources in recent years. The use of small-scale horizontal axis wind turbines (HAWT) as a source of electricity is a viable solution. Despite significant progress in the wind energy field, there is always space for improvement in terms of efficiency, cost and the energy extracted.

This thesis discusses the aerodynamic design and performance analysis of a small scale HAWT using two reliable methods: The blade element momentum (BEM) method and the computational fluid dynamics (CFD) method. This study is divided into two major parts. Two blade configurations with the same length of 5m are designed and analysed.

The first part discusses the aerodynamic performance analysis of the 1st blade configuration using the BEM method. The blade is designed and aerodynamically optimized using QBlade software. Power output, power coefficient, and annual yield for a given Weibull distribution is determined using QBlade software.

The second part investigates the impact of integrating a stationary sealed gap trailing edge flap to the 1st blade configuration (2nd configuration) for HAWT applications using both CFD and BEM methods. Accordingly, performance of the 3D blade with a trailing edge flap is determined. Finally, a comparative analysis is conducted to find the optimal blade design amongst both configurations based on power output and annual yield.

The BEM results show that At the design tip speed ratio of 7, the power coefficient in

the 2nd design configuration is 8.3% higher than the 1st design configuration. According to the 2nd configuration, the CFD method over-predicts the power coefficient compared with the BEM method. The power coefficient from 3D CFD simulation is approximately 12% higher. The annual yield of the wind turbine with the 1st and 2nd configuration is found as 6378 kWh/year and 6944 kWh/year respectively.

Keywords: QBlade, Wind Turbine, BEM, CFD, Trailing Edge Flap, Numerical Analysis, Blade Configuration.

ÖZ

Rüzgar enerjisi, son yıllarda en hızlı gelişim gösteren yenilenebilir enerji kaynaklarından biri olarak öne çıkmaktadır. Öte yandan, küçük ölçekli yatay eksenli rüzgar türbinlerinin (YART) elektrik üretimi amaçlı kullanımı uygulanabilir bir yöntem olarak görülmektedir. Şu ana dek rüzgar enerjisi alanında önemli yenilikler sağlanmasına rağmen, verimliliğin artırılması, maliyetlerin azaltılması ve enerji üretim performansının artırılması anlamında gelişime açık yönler bulunmaktadır.

Bu çalışmada, küçük ölçekli yatay eksenli bir rüzgar türbininin aerodinamik tasarımı ve performans analizleri gerçekleştirilmiştir. Bu amaçla Kanat Elemanı Momentum (KEM) yöntemi ve Hesaplamalı Akışkanlar Dinamiği (HAD) yöntemi olmak üzere iki farklı etkin teknik kullanılmıştır. Çalışma iki farklı temel kısma bölünmüştür. İlgili kısımlarda, 5m uzunluğa sahip iki farklı kanat konfigürasyonu tasarlanarak analiz edilmiştir.

İlk bölüm, birinci kanat konfigürasyonunun aerodinamik performansının KEM yöntemi kullanılarak incelenmesini kapsamaktadır. İncelenen kanat, QBlade programında tasarlanmış ve aerodinamik olarak optimize edilmiştir. QBlade programı kullanılarak, bu kanat konfigürasyonunun sağladığı güç çıktısı, güç katsayısı ve seçilmiş belirli bir Weibull dağılımına göre yıllık enerji üretimi belirlenmiştir.

Çalışmanın ikinci bölümünde, YERT uygulamaları için, birinci kanat konfigürasyonuna, sabit sızdırmaz boşluklu arka kenar kanatçığının entegre edilmesinin (ikinci konfigürasyon) etkisi, KEM ve HAD yöntemleri kullanılarak incelenmiştir. Bu bağlamda, arka kenar kanatçıklı üç boyutlu kanadın performansı

analiz edilmiştir. Son olarak, her iki konfigürasyon, güç çıktısı ve yıllık enerji üretimi parametrelerine göre karşılaştırmalı olarak incelenmiş ve ideal kanat tasarımı belirlenmiştir.

KEM sonuçlarına göre, kanat ucu hızının 7 olduğu durum için, ikinci kanat konfigürasyonunun güç katsayısı birinci konfigürasyona göre 8.3% daha yüksek olarak bulunmuştur. İkinci kanat konfigürasyonu için uygulanan iki farklı analiz yöntemi karşılaştırıldığında, HAD yönteminin, güç katsayısını, KEM yöntemine göre yaklaşık 12% daha yüksek olarak hesapladığı görülmüştür. Son olarak, birinci ve ikinci kanat konfigürasyonunu kullanan bir YERT'nin yıllık enerji üretimi, sırasıyla 6378 kWh/yıl ve 6944 kWh/yıl olarak hesaplanmıştır.

Anahtar Kelimeler: QBlade, Rüzgar Türbini, KEM, HAD, Arka Kenar Kanatçığı, Sayısal Analiz, Kanat Konfigürasyonu.

... *Dedicated to my wife Raneem and my parents*

ACKNOWLEDGMENT

First of all, I would like to express my deepest appreciation and gratitude to my supervisor Assist. Prof. Dr. Devrim Aydin for giving me complete guidance during my research to accomplish this work. It was a big honor to work under his guidance..

Finally, a special thanks to my caring and supportive family that stood with me and gave all the encouragement when things got rough.

TABLE OF CONTENTS

ABSTRACT	iii
ÖZ.....	v
DEDICATION	vii
ACKNOWLEDGMENT	viii
LIST OF TABLES.....	xi
LIST OF FIGURES	xii
LIST OF SYMBOLS AND ABBREVIATIONS	xv
1 INTRODUCTION	1
1.1 Background	1
1.2 Historical Overview	3
1.3 Wind Energy in Turkey	6
1.4 Aim and Objectives.....	8
1.5 Scope of the Work	8
1.6 Thesis Structure and Workflow Diagram	10
2 LITERATURE REVIEW	12
2.1 Wind Turbine Classification.....	12
2.2 One-dimensional Momentum Theory.....	16
2.3 Blade Element Momentum (BEM) Method	18
2.4 QBlade Software.....	20
2.5 Computational Fluid Dynamics (CFD) Method.....	23
2.5.1 Previous Studies in the Literature	25
3 METHODOLOGY	28
3.1 Turbine Blade Design: 1st Configuration	28
3.1.1 Wind Turbine Power	29

3.1.2	Wind Speed	30
3.1.3	Rotor Radius	30
3.1.4	Aerodynamic Characteristics of S809 Airfoil	31
3.1.5	Design Tip Speed Ratio	38
3.1.6	Blade Design and Optimization	40
3.2	Turbine Blade Design: 2nd Configuration	45
3.3	Annual Yield	49
3.4	CFD Method	51
3.4.1	2D CFD Validation and Analysis	51
3.4.2	3D CFD Analysis: 2nd configuration	58
4	RESULTS.....	61
4.1	BEM Results and Analysis: 1st Configuration	61
4.2	BEM Results and Analysis: 2nd Configuration	64
4.3	CFD Results and Validation: 2nd Configuration	65
4.4	Annual Yield Results	73
5	CONCLUSIONS	74
5.1	Findings and Conclusions	74
5.2	Future Works.....	76
	REFERENCES	77
	APPENDICES	86
	Appendix A: The Blade Radial Position, Chord, and Twist Angle Distribution of the 2nd Configuration	87
	Appendix B: QBlade Graphical User Interface	89
	Appendix C: CFD Data Visualisation	92

LIST OF TABLES

Table 2.1: Categories of Small Scale Wind Turbine.	13
Table 2.2: Comparison between HAWT and VAWT.	13
Table 2.3: Impact of Number of Blades on Efficiency of HAWT.....	14
Table 3.1: The Relation between the Number of blades and the Tip Speed Ratio. ...	38
Table 3.2: The Power Coefficient at Reynolds number of 500 000	39
Table 3.3: The Blade Radial position, Chord, and Twist Angle Distribution of the 1st Configuration.	42
Table 3.4: The Parameters and Assumptions of the 1st Blade Configuration.....	43
Table 3.5: Drag Coefficient at zero AoA and Re of 1×10^6 for S809 Airfoil.....	53
Table 3.6: Lift Coefficient at zero AoA and Re of 1×10^6 for S809 Airfoil.	54
Table 3.7: A 3D Meshes for Wind Turbine with Different Sizes.	59
Table 4.1: The Torque, Power and Power Coefficient at the Design Condition.....	66
Table 4.2: Annual Yield for both Design Configurations.	73

LIST OF FIGURES

Figure 1.1: Contribution to the Rise in Global Sea Level	2
Figure 1.2: Consumption of Annual Primary Energy from 2008 to 2018.	3
Figure 1.3: Hero’s Windmill	4
Figure 1.4: Smeaton’s (1759) Experimental Arrangements	5
Figure 1.5: Wind Turbine Research and Development.	6
Figure 1.6: Wind Electricity Generation, Turkey 1998-2019.	7
Figure 1.7: Electricity Generation of Wind Power Plants in Turkey in the First Half of 2020.	8
Figure 1.8: Workflow Diagram of this Project.	11
Figure 2.1: Power Curve for Different Control Strategies.	15
Figure 2.2: HAWT Rotor Orientation.	16
Figure 2.3: A Model of Wind Turbine.	17
Figure 2.4: Schematic of Blade Elements.	19
Figure 2.5: Lift Coefficients for Rotating Blade Compared with 2D Steady Curve	20
Figure 2.6: The BEM Parameters Dialog	22
Figure 2.7: Data Flow in QBlade	23
Figure 3.1: A schematic representation of a small scale HAWT	29
Figure 3.2: The Losses of Power in Wind Turbine Components	31
Figure 3.3: The S809 Airfoil by NREL.	32
Figure 3.4: Comparison of XFOIL Lift Coefficient and TUDelft Wind Tunnel Lift Coefficient for S809 Airfoil	33
Figure 3.5: Comparison of XFOIL Drag Coefficient and TUDelft Wind Tunnel Drag Coefficient for S809 Airfoil	33

Figure 3.6: The Polar curves for S809 Airfoil In QBlade "XFOIL Direct Analysis" Tab	34
Figure 3.7: Coefficient of Lift versus AoA for Different Values of Re Number. ...	35
Figure 3.8: Coefficient of Drag versus AoA for Different Values of Re Number ..	36
Figure 3.9: Lift to Drag Ratio versus AoA for Different Values of Re Number	36
Figure 3.10: Extrapolation of Polar Curves	37
Figure 3.11: The Relation between the Power Coefficient and the Tip Speed Ratio	39
Figure 3.12: Optimizing HAWT Blade Geometry Dialog	40
Figure 3.13: The Final Design of the 1st Blade Configuration	43
Figure 3.14: The Rotor Model of HAWT	43
Figure 3.15: The Chord and Twist Distribution of the 1st Blade configuration	44
Figure 3.16: 2D and 3D Gurney Flap	46
Figure 3.17: The S809 Airfoil with a Flap Angle of 10°	47
Figure 3.18: The Lift to Drag Ratio of Airfoil S809 with and without Flap for Reynolds Number of 500 000.....	48
Figure 3.19: Airfoil Sections and a Blade with a Flap Angle of 10°	49
Figure 3.20: The Weibull Distribution of Wind Speed at Height of 20m at INCEK Region-ANKARA	51
Figure 3.21: Domain Size and Block Strategy in ICEM CFD	52
Figure 3.22: Mesh around the Airfoil with and without Flap	52
Figure 3.23: Drag Coefficient Comparison between CFD, XFOIL and Experimental Results for the Airfoil S809.	54
Figure 3.24: Lift Coefficient Comparison between CFD, XFOIL and Experimental Results for the Airfoil S809.	55

Figure 3.25: Pressure and Velocity Contour and Velocity Streamlines for AoA of 6° and 14° for Airfoil S809.	56
Figure 3.26: Pressure and Velocity Contour and Velocity Streamlines for AoA of 6° and 14° for Airfoil S809 with a Flap of 10°.....	57
Figure 3.27: The 2nd Configuration Coordinates and Geometry	58
Figure 3.28: Domain Size and Boundary Conditions	59
Figure 3.29: Unstructured Mesh #2 for the Wind Turbine.	60
Figure 4.1: Power Coefficient versus Tip Speed Ratio	62
Figure 4.2: Power versus Tip Speed Ratio	62
Figure 4.3: Power versus Wind Speed	63
Figure 4.4: Power Coefficient versus Tip Speed Ratio for both Configurations ...	64
Figure 4.5: Power versus Tip Speed Ratio for both Design Configurations	65
Figure 4.6: Power Coefficient Comparison for both Design Configurations	67
Figure 4.7: The Power Output for both Design Configurations.....	67
Figure 4.8: The Velocity Streamlines in a Stationary Frame of Reference.....	68
Figure 4.9: The Velocity Streamlines Plot.	68
Figure 4.10: Velocity Vector in Standard Frame of Reference.	69
Figure 4.11: Pressure Distribution on the Surface of the Blade.....	70
Figure 4.12: Y+ Distribution on the Surface of the Blade.....	70
Figure 4.13: The Velocity Vectors and Pressure Contours of Different Sections of the Blade at the Design Conditions.	71
Figure 4.13: The Velocity Vectors and Pressure Contours of Different Sections of the Blade at the Design Conditions	72

LIST OF SYMBOLS AND ABBREVIATIONS

ρ	Air Density (kg/m^3)
σ	Solidity
ω	Angular Velocity (Rad/Sec)
λ	Tip Speed Ratio
ε	The Rate of Dissipation of Turbulent Kinetic Energy
α_{loc}	Local Inflow Angle of Attack ($^\circ$)
η_{mech}	Mechanical Efficiency
\dot{m}	Mass Flow Rate
(C_L/C_D)	Lift to Drag Ratio
a	Axial Induction Factor
C_D	Drag Coefficient
C_L	Lift Coefficient
C_P	Power Coefficient
C_T	Thrust Coefficient
p	Pressure (Pa)
P_D	Design Power (W)
P_{rated}	Rated Power (W)
R	Rotor Radius (m)
U_D	Design Wind Speed (m/s)
A	Scale Parameter of Weibull Distribution
AoA, α	Angle of Attack ($^\circ$)
B	Number of Blades
BEM	Blade Element Momentum
c	Chord Length (m)

CFD	Computational Fluid Dynamics
F	Prandtl's tip loss factor
FPVS	Fixed Pitch Variable Speed
HAWT	Horizontal Axis Wind Turbine
K	Turbulent Kinetic Energy
k	Shape Factor of Weibull Distribution
Ma	Mach Number
P	Power (W)
r	Local Radius (m)
RANS	Reynolds-averaged Navier–Stokes
Re	Reynolds number
T	Thrust Force (N)
U	Wind Speed (m/s)

Chapter 1

INTRODUCTION

1.1 Background

Energy is necessary for the advancement of human civilization. Because of the remarkable progress in various fields such as industry, transportation and economy, energy demand has increased. As a result of the rising demand, the world tends to utilize renewable energy as a clean and environmentally friendly alternative, such as solar, tide, wave and wind energy. The latter plays an essential role as one of the most important forms of sustainable energy derived from nature. Furthermore, in the last few decades, the world began to shine a spotlight on global warming and environmental damage due to the emissions resulting from the daily use of fossil fuels.

Even today, the world is attempting to concentrate on climate change and its effects on polar regions and glaciers to avoid rising water levels, leading to floods and the inundation of coastal areas and islands. As a result of climate change, the global mean sea level jumped 87.6 mm from 1983 to 2019 [1]. From the foregoing, it clearly appeared that the nations must take the responsibility to follow alternatives that reduce the above mentioned risks. Figure 1.1 shows the global sea-level rise's contribution from 1983 to 2019.

To understand the significance of renewable energy, consider the world statistics in the last decade, which shows that the world is consuming more and more primary

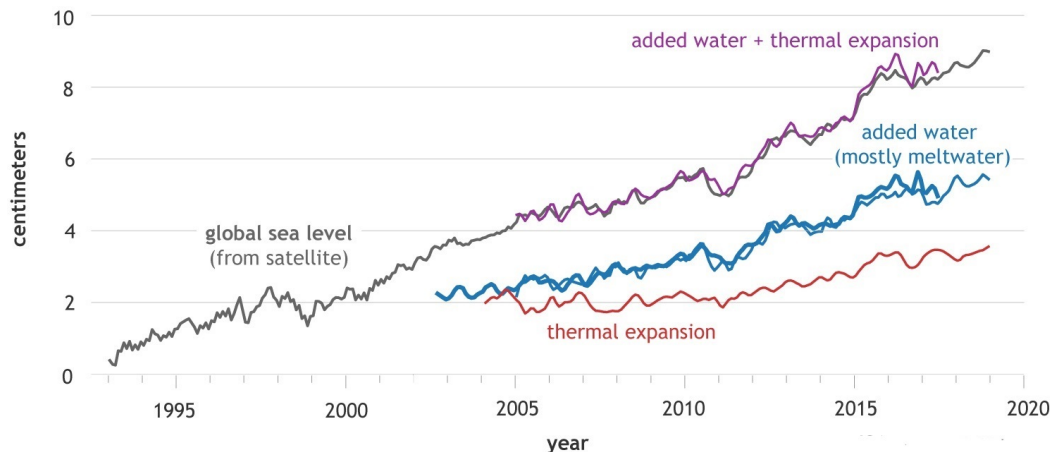
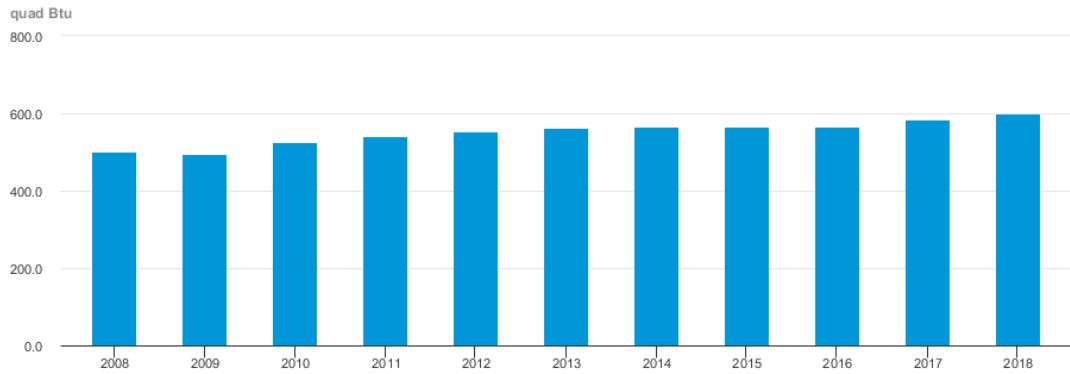


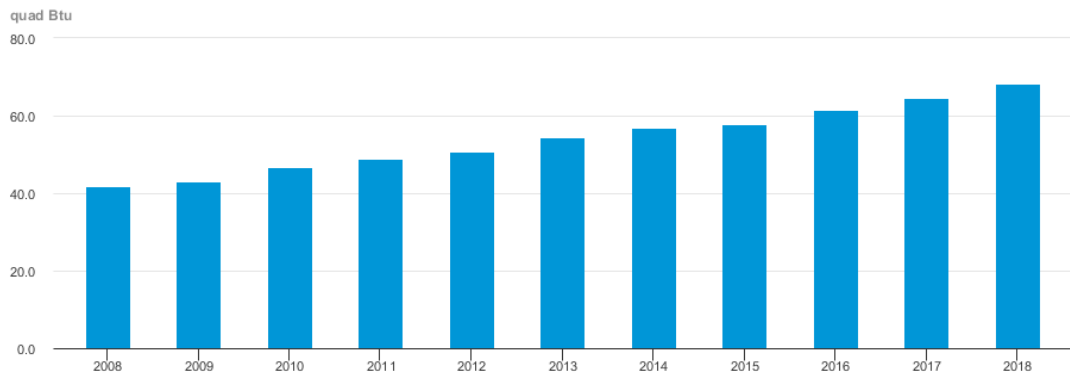
Figure 1.1: Contribution to the Rise in Global Sea Level [1].

energy. According to The US Energy Information Administration (EIA), the world consumed about 600 quads Btu of primary energy (coal, natural gas, petroleum, nuclear and renewable energy) in 2018, while 11% of this consumption was produced by renewable energy (68 quads Btu) [2]. New wind and solar capacities and continuous cost reductions in solar and wind technologies, as well as motivated climate policies in the EU, the US and China, have helped to boost renewable energy capacity and generation [3]. Figure 1.2 shows the total annual primary energy consumption from 2008 to 2018.

Wind is a pollution-free green energy source that creates no pollutants in the water or air. Because wind is free, once a turbine is installed, operating costs are negligible. Turbines are becoming more affordable as a result of mass production and technological advancements, and many governments are providing financial incentives to encourage the growth of wind energy.



(a) World-Total Energy Consumption.



(b) World-Total Energy Consumption from Renewable Energy.

Figure 1.2: Consumption of Annual Primary Energy from 2008 to 2018 [2].

1.2 Historical Overview

There is no doubt that people have been using wind energy for thousands of years. It is logically assumed that wind exists before human exists; the wind was begun after the sun radiated and heated the earth's surface. Since the beginning of the Pharaonic civilization, people have used wind energy as a power source to help them sail along the Nile. According to the old Greek and Roman culture, the wind was the first fundamental element to expand and trade. It is worth noting that Hero of Alexandria invented the first windmill in the first century of the common era. In truth, Hero did not build it completely but built a prototype and connected it to an air pump.

Therefore, the best word to describe the Hero's small scale windmill was a toy [4].

Figure 1.3 shows Hero's windmill description from Woodcroft.

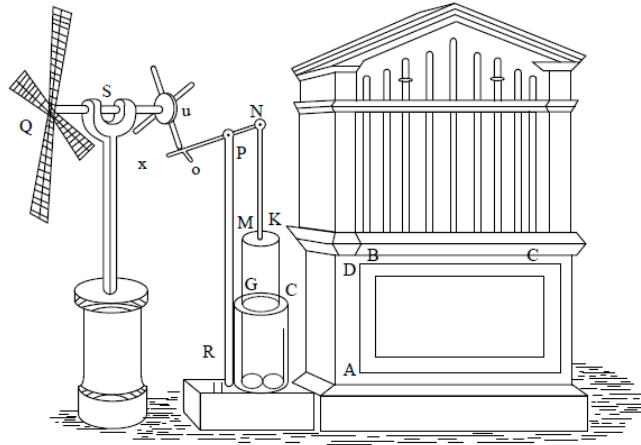


Figure 1.3: Hero's Windmill [5].

Afterward, the first appearance of windmills takes place in northern Europe in the 12th century. This windmill and the early north European windmills all had horizontal axes. Additionally, posts usually were the type of construction of these mills, and four blades and yaw systems were typically used. This type diminished just before the industrial revolution because of its non-transportability [6]. Windmills of a new style can be found in France by the 14th century. They are called tower mills because they are bigger and more rigid than post mills. Just the upper part of the mill rotates. It sits on top of the mill tower like a loose hat, supporting the sails' horizontal axle. It can be turned using either the traditional pole from outside or a lever inside the cap. During the 18th century, the windmills witnessed remarkable progress in design, and the cross section of the blades began to become similar to the airfoil. John Smeaton, an Englishman, conducts a scientific experiment on windmills in the 1750s, and his conclusions still applicable now. His observations are interpreted as maxims [7, 8]. Consequently, Smeaton concluded that there is a relationship between the blade tip speed and the wind speed, and also observed that the power is proportional to the

speed of wind cubed and the area of the blade disk. Figure 1.4 shows Smeaton's (1759) experimental arrangements.

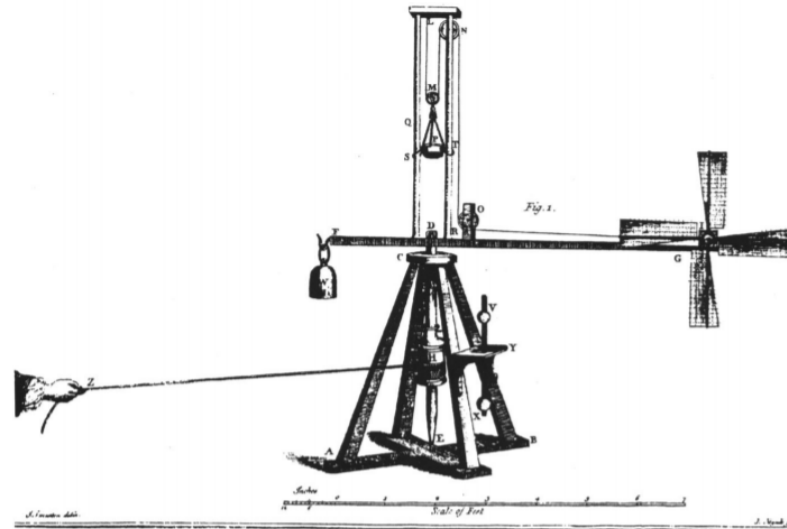


Figure 1.4: Smeaton's (1759) Experimental Arrangements [8].

Historically, windmills were used to pump water and agricultural purposes, but during the 21st century, there was a connection between wind power and electricity. Charles Brush, a scientist from Cleveland, Ohio, was the first to build a practical large wind turbine, but the lack of electricity constrained his studies. His turbine consists of 144 slender blades with 18m tower height and 17m disk diameter and connected with 100 light bulbs and a set of motors [9]. Many wind turbines were built or conceptualized in the first half of the last century, which significantly impacted today's technology. The Smith–Putnam turbine, designed at Grandpa's Knob in Vermont in the late 1930s, was the most notable early large turbine in the US. With a diameter of 53.3m and a power output of 1.25MW, it is the largest wind turbine in the world until that time [10]. Commercial wind turbines have grown in scale in recent years, from about 10kW to 10MW. As of 2009, the world's overall installed capacity was about 115000MW [10], with the majority of installations in Europe. Economically, the cost of wind energy

has fallen to the point that it is now almost comparable with traditional sources in many locations. The advancement in other fields such as computer science, materials and aerodynamics have an impact on wind turbine technology. Figure 1.5 shows the development in the diameter, height, size and wind turbine capacity since 1980.

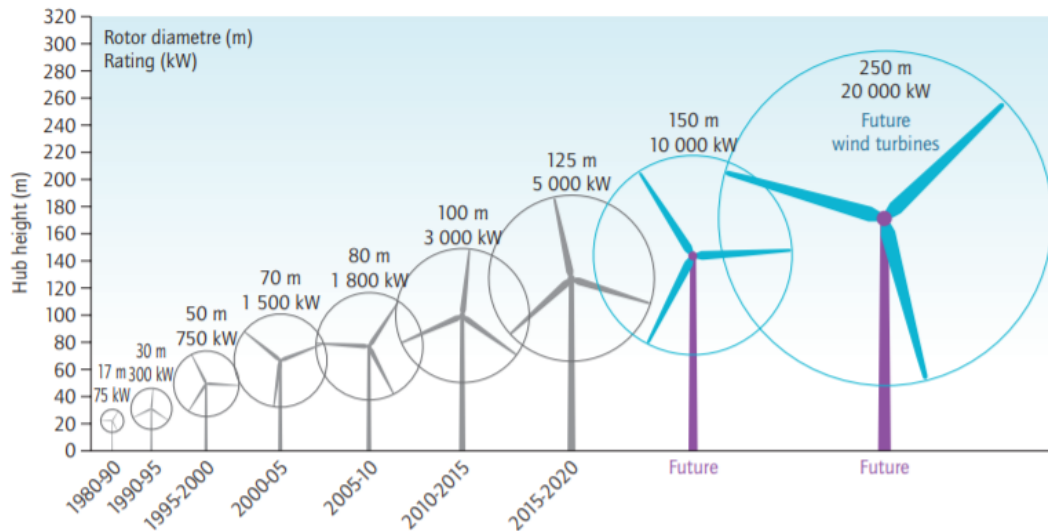


Figure 1.5: Wind Turbine Research and Development [11].

1.3 Wind Energy in Turkey

Renewable energy sources are generally recognized as crucial to a country's long-term success. Turkey is becoming a major transit route for oil and natural gas supplies flowing from Central Asia, Russia, and the Middle East to Europe and other Atlantic markets. Turkey was one of the earliest investors in the wind energy sector since its national fossil fuel resources are severely restricted, and its geographical position offers numerous benefits for the long-term usage of wind power. The first wind farm in Turkey was built in İzmir in 1998 [12]. According to the Turkish Wind Energy Association (TUREB), the total installed capacity of 9305 MWm Wind Power Plant and Sum of 239 operational wind power plants with 3591 installed wind turbines are located in Turkey, which meets 8.44% of electricity generation from the wind in 2020 [13]. In 2019, more than 21 GWh of electricity were produced by wind power plants

[14]. Soma wind power plant in Manisa, the largest wind energy power plant in Turkey with 312.1 MWe installed power and 181 turbines, meets all electrical energy needs of an average of 160 thousand people. Obviously, the majority of wind power plants (WPP's) are located in İzmir, Balıkesir and Manisa.

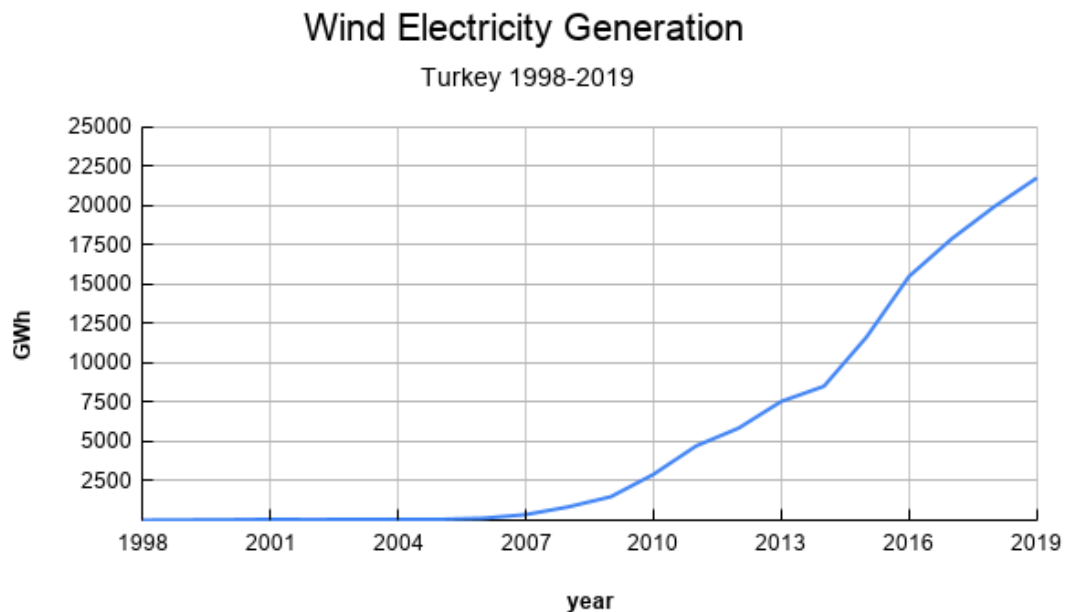


Figure 1.6: Wind Electricity Generation, Turkey 1998-2019. Adapted from Turkish Wind Energy Association (TUREB) [13].

Turkey, like the rest of the world, lives in exceptional circumstances as a result of the epidemic that has changed people's lives considerably. This pandemic also had a noticeable impact on the progress in the field of wind energy. Covid-19 has unfortunately jeopardized the completion of wind projects due to disruptions, especially in procurement, permitting procedures, and funding. However, Turkey has the vision to reach 25GW wind installed capacity by 2030 [13]. Figure 1.7 shows the effects of Covid-19 on electricity generation of wind power plants in Turkey in the first half of 2020.

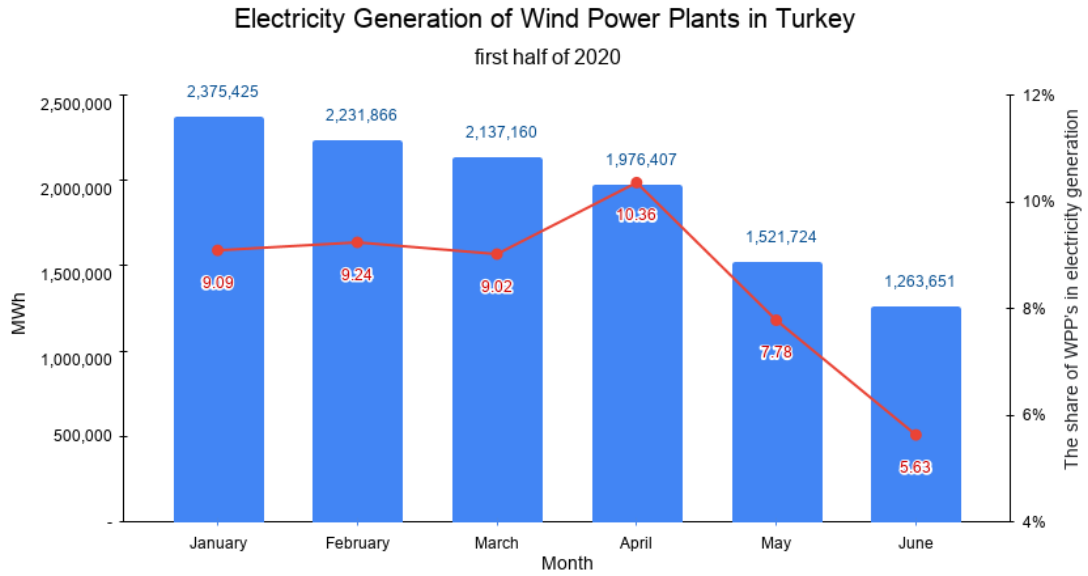


Figure 1.7: Electricity Generation of Wind Power Plants in Turkey in the First Half of 2020. Adapted from Turkish Wind Energy Association (TUREB) [13].

1.4 Aim and Objectives

This study aims to provide a method for designing a 5m small scale HAWT with different blade configurations. In addition, a fixed training edge flap is used to improve the efficiency and the energy extracted. The main objectives of the thesis are:

- To analyse the aerodynamic performance of S809 airfoil with and without flap.
- To offer a user guide for the QBlade wind turbine software.
- To use trailing edge flap for the applications of wind turbine.
- To predict the output power and annual yield of a wind turbine.
- To compare different blade geometries to choose the efficient blade.

1.5 Scope of the Work

Wind turbines should be designed to have the lowest possible energy cost. During the design process, it is essential to keep the Levelized Cost Of Energy (LCOE) as low as possible. This approach is carried using multidisciplinary design optimization for all turbine components. Since a turbine blade rotates and subjected to cyclic and aerodynamic loads, it is the critical component of this approach.

The scope of the study is to provide a detailed investigation on aerodynamic design and performance analysis of HAWT using the CFD approach and BEM approach. There are two main parts in this thesis. The first part of the thesis discusses the aerodynamic design and performance of a stall regulated, fixed pitch variable speed, 5m horizontal axis wind turbine using the blade element momentum theory (BEM). The S809 airfoil is used in this study. The aerodynamic data and polar curves are obtained using the XFOIL software. The XFOIL data will be validated and compared with experimental data. Afterward, the 1st blade configuration will be designed and aerodynamically optimized using QBlade software. Thanks to QBlade software, power output, power coefficient and annual yield for a specific Weibull distribution (i.e. shape factor and scale parameter) will be investigated. For the 1st design configuration, the CFD study will not be implemented due to the time limit.

The second part of the thesis investigates the usage of the trailing edge flap for wind turbine applications. To show the effect of the flap, some design parameters will be kept same as the 1st configuration. The trailing edge flap used in this study is stationary, i.e., sealed gap flap. Since XFOIL does not assume any gap, the flap is only accounted for the modified lift and drag coefficient tables that result from the XFOIL simulation of the airfoil S809. Therefore, the flap is fixed and the flap angle δ is set to 10° clockwise. A comprehensive 2D study of the airfoil S809 with and without flap is implemented. Both CFD and BEM methods are applied to evaluate the performance of a 3D blade with flap. Finally, a comparative study between both configurations depending on the power output and annual yield is done to determine the optimum blade design.

1.6 Thesis Structure and Workflow Diagram

In this thesis, the design of a small scale wind turbine is divided and organized into 5 chapters.

Chapter 1 provides a historical overview and some statistical data about energy consumption and green energy production.

Chapter 2 provides the classifications, literature review, software and theories related to wind turbine and its applications.

Chapter 3 provides the design procedure of 10 kW small scale HAWT with and without flap using QBlade and CFD software.

Chapter 4 provides the results and comparison between design configurations and the approaches that used during the design process.

Chapter 5 provides an overview of the thesis and the methods used in the study and gives some recommendations and future works. Figure 1.8 shows the work flow diagram for this thesis.

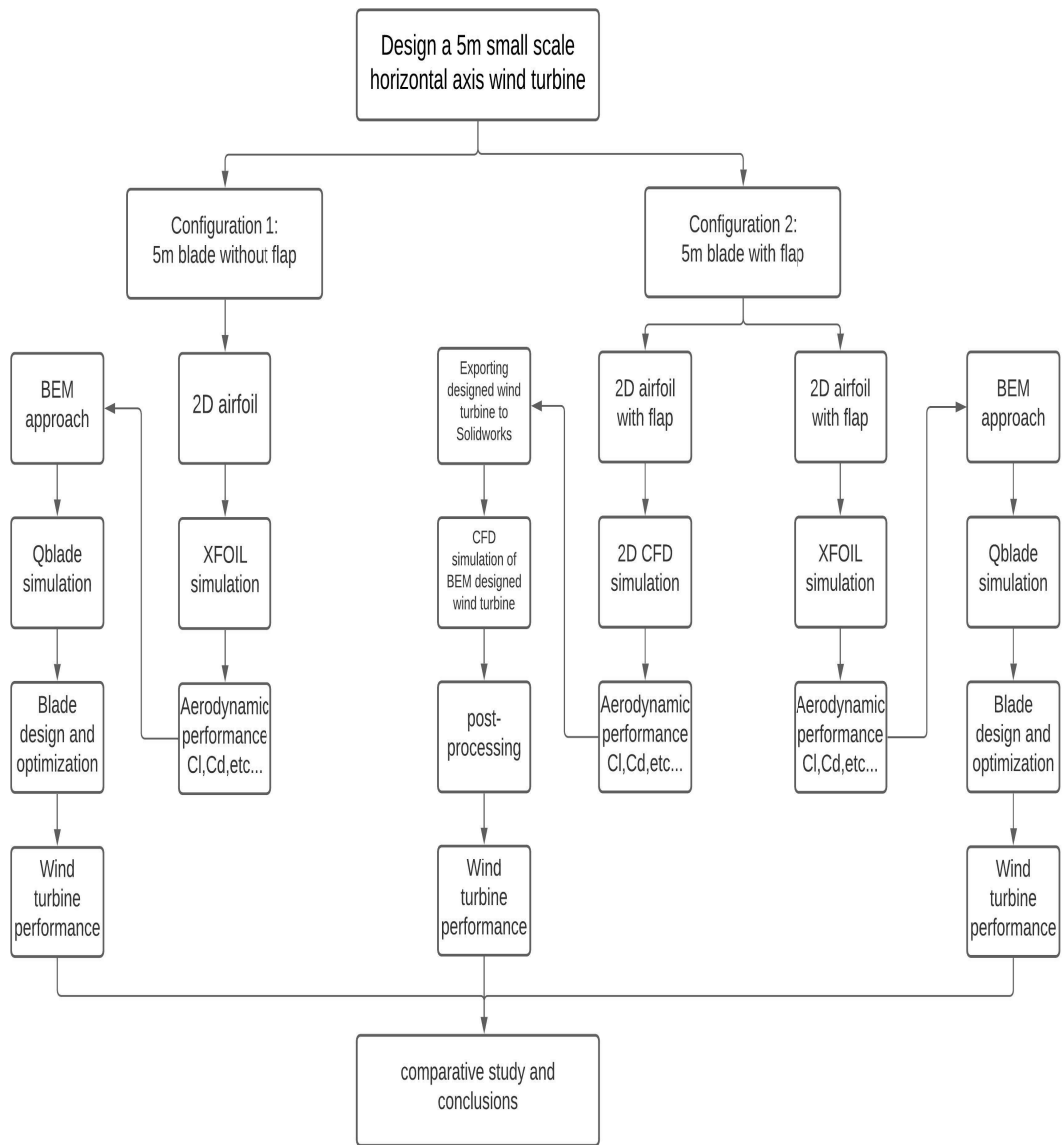


Figure 1.8: Workflow Diagram of this Project.

Chapter 2

LITERATURE REVIEW

2.1 Wind Turbine Classification

A wind turbine is a machine that converts wind energy into electricity. A windmill, on the other hand, is a machine that converts the energy of the wind into mechanical power. Today, modern wind turbines are classified into different categories based on the size, orientation, number of blades, hub design, rotor control, etc.... This section provides a detailed discussion for each classification with its benefits and drawbacks.

The first classification of modern wind turbines is based on the size of the rotor disk. Large modern wind turbines, which are primarily used in wind farms to generate power for large grids, represent a large proportion of wind electricity generation. On the other hand, wind turbines with a power output up to 50kW are mostly located in remote areas to generate power to small grids. The small scale turbines operate at a low Reynolds number, high angle of attack and high rotational speed. As shown in table 2.1, small scale turbines are divided into three categories: micro, mid-range, and mini turbines, depending on the power output and blade radius [15]. . In contrast with large wind turbines, small turbines have fewer movable parts than large turbines. Some components used in a large turbine may be omitted to reduce the cost of material, operation and maintenance and increase the lifetime.

The second essential classification of a modern wind turbines is based on the axis of rotation. Mainly, there are two types of wind turbines: horizontal axis wind turbines

Table 2.1: Categories of Small Scale Wind Turbine.

Category	Power output (kW)	Radius (m)	Max, rotor speed (RPM)
Micro	1	1.5	700
Mid-range	5	2.5	400
Mini	10-50	5	200

(HAWT) and vertical axis wind turbines (VAWT). Turbines with horizontal axis have proven to be the most efficient [16]. In many parts of the world, they are used for commercial electricity production. Besides, HAWT is usually accompanied by a yaw system to adjust the turbine to the flow stream. However, vertical axis wind turbines contain few movable parts and not efficient as HAWT, it suitable for building applications and urban areas. Since vertical wind turbines run at low wind speeds, their performance is limited. Table 2.2 compares the two types.

Table 2.2: Comparison between HAWT and VAWT [16].

Comparison between HAWT and VAWT	
HAWT	VAWT
• More efficient	• Less efficient
• A yaw system is mandatory	• No need to turn the rotor toward the wind
• Suitable for remote areas	• Suitable for remote and urban areas
• The machine is self-starting	• A push is needed to start
• On the tower, the gearbox, generator, etc..., are installed.	• It does not require a huge tower because the gearbox, generator, etc..., may be put on the ground.
• Tip speed ratio is considerably high	• Tip speed ratio is low

The next classification of modern wind turbines is based on the number of blades. In order to determine the number of blades in the turbine, the cost-efficiency should be considered. Adding blades to the turbine means an additional cost in terms of material, manufacturing, transportation and installation. On the other hand, the number of blades (B) has an impact on the power output performance of wind turbines as shown in table

2.3. Additionally, as the number of blades increases, the blades get slenderer, requiring structural considerations [17]. Today, modern wind turbines have designed with two or three blades.

Table 2.3: Impact of Number of Blades on Efficiency of HAWT.

Number of blades	Efficiency impact
2	43%
3	47%
4	50%

Turbines are built to withstand strong winds in a static state. This implies that as long as they are not rotating, they can withstand a high wind speed. They are not made to withstand high rotational speeds. The stresses on the blades and other turbine components are high at high aerodynamic torques or rotational speeds, and can break the turbine blades. Wind turbines are designed with a cut-out wind speed to slow down the turbine at high wind gust to avoid the catastrophic situations. Wind turbines use different active and passive control strategies to limit the power output at high wind speeds. Pitch-regulated and stall-regulated are two types of control strategies.

Pitch-regulated wind turbine has a pitch mechanism operates using hydraulics to limit the power at high wind speed. When the speed of the wind becomes too high, An active pitch control pitch the blades of turbine out of the wind. Thus, the rotor blades move longitudinally i.e., the blades are pitched into stall. This method of regulation is normally used only when there is high wind speed. Since the rotors move out of the wind, the lift force decreases while the drag force increases due to flow separation. As a result, the rotational speed of the rotor or the torque transmitted to the shaft is reduced, allowing the rotational speed to remain stable.

On the other hand, the stall-regulated strategy relies on the rotor blades' aerodynamic design to limit the power output at high wind velocity. The rotor blades are bolted at a fixed angle to the hub in passive stall wind turbines. The blades are designed and twisted to be less aerodynamically efficient by creating turbulence on the back side of the rotor blades at high wind speed. Figure 2.1 shows the power curves for both control strategies.

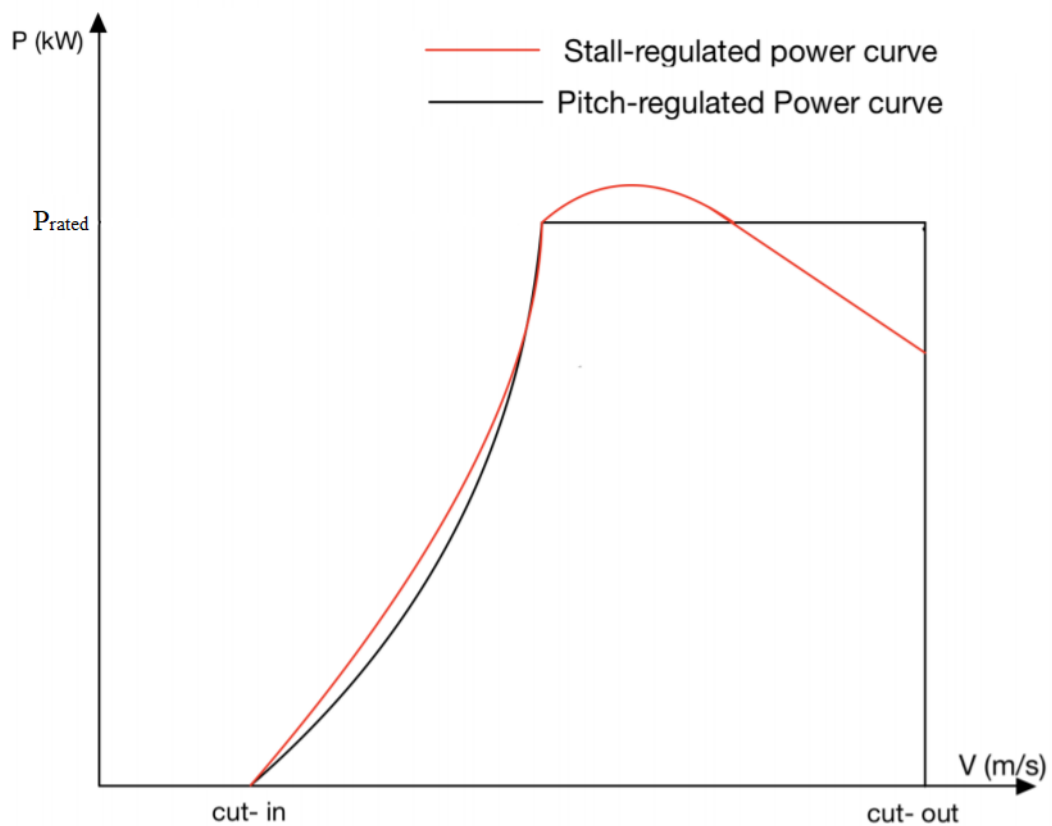


Figure 2.1: Power Curve for Different Control Strategies.

Rotor blades can be set to face the upstream wind (upwind) or directed toward downstream wind (downwind). The primary benefit of upwind structures is that the wind shade behind the tower is avoided. On the other hand, downwind turbines have the benefit of not requiring a yaw mechanism since the nacelle and rotor are constructed to passively follow the wind.

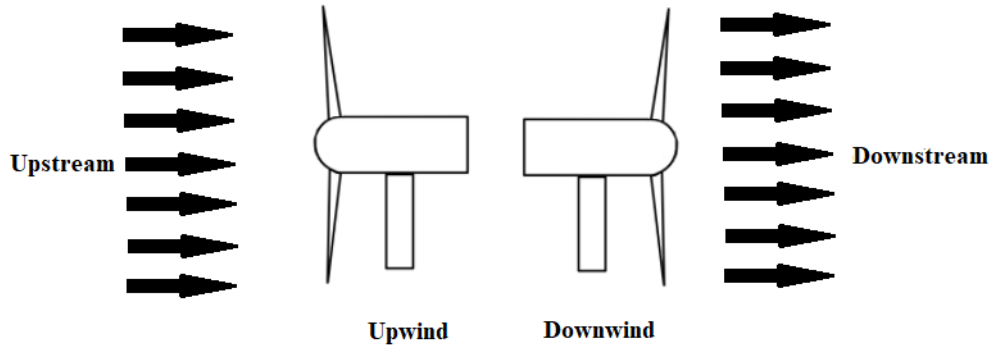


Figure 2.2: HAWT Rotor Orientation.

To sum up, modern wind turbines can be classified into different groups. In this study, the focus will be on small scale wind turbines with a rated power of 10 kW, three rotor blades, stall-regulated power controlling and upwind orientation.

2.2 One-dimensional Momentum Theory

In HAWT design, airfoils are used to convert kinetic energy in the wind into usable energy. Methods for calculating wind turbine rotor output in steady state have been developed by a variety of authors. Betz and Glauert were the first to establish a classical wind turbine study [18].

In 1926, Albert Betz generalized a model to determine the extracted power from an ideal rotor based on a linear momentum theory [18]. In his model, a uniform actuator disc represents the rotor, and the fluid is assumed to be incompressible, homogeneous and steady state. The disc is assumed ideal since it is frictionless and does not have a rotational velocity component. The rotor disc reduces the wind speed from U_1 far upstream to U_3 at the rotor plane and U_4 in the wake [19]. As a result, as seen in Figure 2.3, the streamlines must diverge.

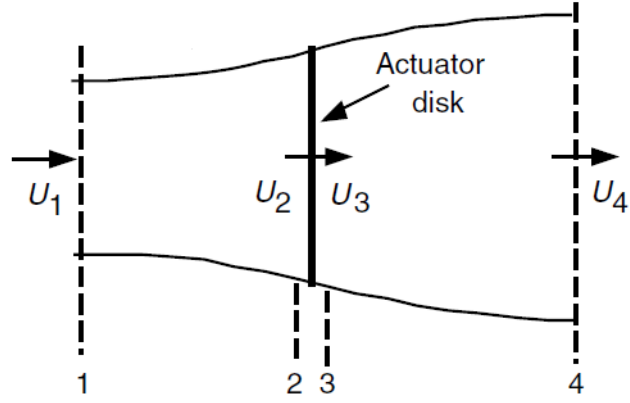


Figure 2.3: A Model of Wind Turbine [6].

The conservation of linear momentum surrounding the entire system may be used to calculate the net thrust on the contents of the control volume. Assuming a steady state flow, then the thrust :

$$T = \dot{m}(U_1 - U_4) \quad (2.1)$$

Since no work is added to the control volume, the Bernoulli equation is valid upstream and downstream of the actuator disc. By using Bernoulli equation and the assumption of $p_1 = p_4$ and $U_2 = U_3$, the thrust can be written as:

$$T = \frac{1}{2}\rho A_2(U_1^2 - U_4^2) \quad (2.2)$$

By using equation (2.1) and (2.2):

$$U_2 = \frac{U_1 + U_4}{2} \quad (2.3)$$

That is, the speed of wind at the disk equal the average of upstream and downstream wind speed. The fractional decrease in wind velocity between the free stream and the rotor plane is known as the axial induction factor a . Thus:

$$U_2 = U_1(1 - a) \quad (2.4)$$

$$U_4 = U_1(1 - 2a) \quad (2.5)$$

The non-dimensional power coefficient, C_p , describes the performance of a wind

turbine:

$$C_P = \frac{P}{\frac{1}{2}\rho AU^3} \quad (2.6)$$

Where P is the power output from the wind turbine which equal to the thrust times the velocity at the disc. Hence, C_P can be written as:

$$C_P = 4a(1 - a)^2 \quad (2.7)$$

By taking the first derivative of C_P (Equation (2.7)) with respect to a and setting it to zero, the maximum C_P can be calculated as:

$$C_{P,max} = \frac{16}{27} = 0.5926 \quad (2.8)$$

According to Betz law, a wind turbine can only convert less than 59% of the wind kinetic energy into useful energy. A linear momentum theory assumed a non-rotating wake, while in a real case, the flow behind a rotating wind turbine rotates in the opposite direction to the rotor as a result of the torque exerted by the flow on the rotor.

2.3 Blade Element Momentum (BEM) Method

To examine wind turbine models, several aeroelastic codes are used in researches and industry. These models are based on the BEM theory, explaining how a wind turbine rotor behaves in a steady and unsteady state. In the previous section, the conservation of linear and angular momentum were used to determine the flow field around a wind turbine rotor defined by an actuator disc. A momentum theory is based on the conservation of angular and linear momentum. A study of forces at a segment of the blade geometry is referred to as blade element theory. Strip theory, also known as blade element momentum (BEM) theory, combines both methods. In this theory, the one-dimensional momentum theory is applied to a blade which is divided into annular segments (N), then the forces on the blade are integrated and calculated based on the aerodynamic data of the airfoil, and the twist angle and the chord of the blade

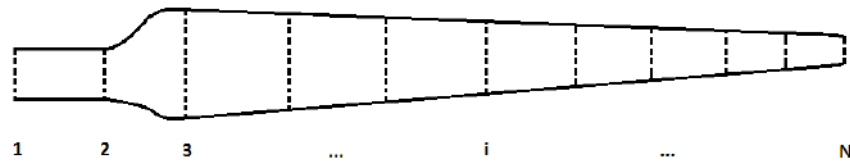


Figure 2.4: Schematic of Blade Elements.

geometry. The 2D aerodynamic data is calculated using wind tunnel or using software such as XFOIL. The BEM assumes that there is no radial flow, thus, there is no aerodynamic interaction between segments.

Many researchers agree that the BEM method is the most commonly used and effective method for designing and analyzing wind turbine blades [20–25]. This approach is an analytical approach that relies on pure 2D flow to determine the forces of the blade segments. Thus, less computational time and effort is needed.

However, the BEM method becomes inefficient at turbulent wake conditions and does not provide accurate results at stall conditions [6]. This is because the momentum theory fails to describe the turbulent flow downstream of the disk. According to the equation (2.5), the equation gives a negative downstream velocity (U_4) when the axial induction $a \geq 0.5$ which is illogical. Also, the BEM method assumes that no radial flow between the blade segments; therefore, there are no interactions, but in fact, the annular segments appear to interact, resulting in span-wise flow.

Another limitation of the BEM method, it depends on the 2D aerodynamic data to simulate the 3D flow. It is noted that the 2D flow characterizations cannot be able to simulate the 3D flows. Using a wind tunnel or a software such as XFOIL, the 2D aerodynamic data is measured. However, testing the airfoil in a wind tunnel for wide

range of angle of attack and Reynolds number is impractical, and therefore time-consuming. In reality, the rotating blade's pressure distribution differs from the steady 2D aerodynamic results. A rotating blade is subjected to a Coriolis force, which works in the same way as a favorable pressure gradient and delays the stall [26]. Himmelskamp [27] was the first to note this phenomenon in helicopter propellers in his thesis in 1945. In comparison to the steady 2D case, the lift is higher and the drag is lower. In classical BEM theory, to get accurate results, Prandtl's tip loss factor (F) and Glauert correction model must be applied to the algorithm [19]. These correction models will be discussed further in section 2.4.

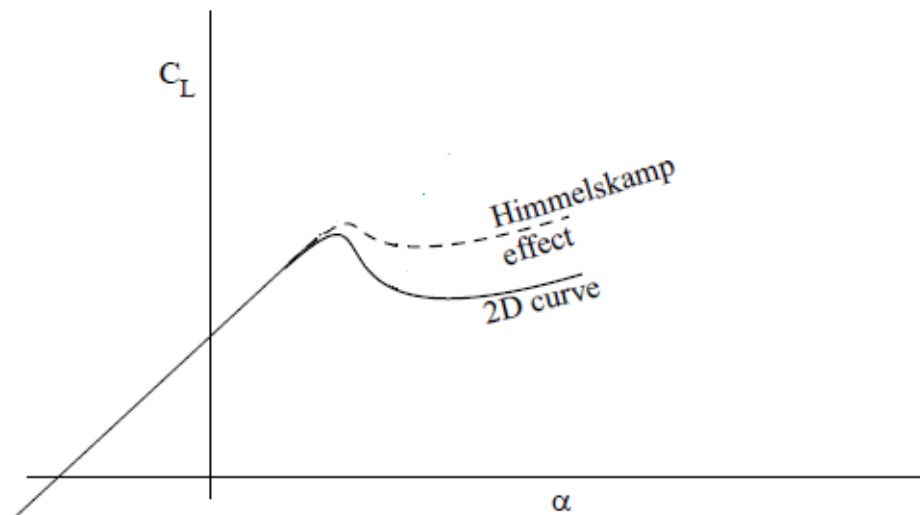


Figure 2.5: Lift Coefficients for Rotating Blade Compared with 2D Steady Curve.

2.4 QBlade Software

Wind turbine rotor design are derived from the aircraft design industry and uses the same techniques. However, the flow conditions that affect a turbine blade are entirely different from those that affect the Airplane. The flow around a wind turbine is complex, unsteady, incompressible and turbulent. A complete CFD analysis that meets these criteria takes a long time and expensive. The BEM model allows the

designer to quickly create and test various rotor designs against one another and determine the optimum design that can later be tested in greater detail using other techniques, such as CFD. Thus in the industry field, design and analysis of HAWT is based on the BEM method [28].

The QBlade software was created by a wind energy team at the Technical University of Berlin as an open-source and flexible platform for wind turbine simulation. QBlade software works with XFOIL to provide one software for the aerodynamic analysis and blade design of wind turbine. Users will design or import airfoils and generate their polar curves in XFOIL, then extrapolate the polar curves to 360° angle of attack and directly implement them into a wind turbine simulation. QBlade has several functions and friendly GUI that allows the users to select manually all simulation parameters. A wind turbine blade is subjected to higher angles of attack than an airplane wing. Thus, to guarantee the continuation of the BEM algorithm, polar curves for all necessary 360° angle of attack must be available. In QBlade, Users are allowed to extrapolate the polar curves with Montgomery extrapolation algorithm or Viterna-Corrigan post stall model. Both algorithms are carried out as described in references [26] and [29].

When defining a simulation in QBlade, the user has to set some parameters and choose the correction models manually from the Simulation dialog. In classical BEM theory, the 3D results can not be considered due to its 2D nature. Different correction algorithms are used to account the 3D effects. Several correction models are available in the QBlade simulation dialog. The most famous models are Prandtl's tip loss factor, which corrects the infinite number of blades assumption, and the Glauert correction model which gives an empirical relations between the thrust coefficient, C_T , and the induction factor, a , when the momentum theory does not valid. The

vortex phenomenon in the wake of a rotor with a finite number of blades differs from that of a rotor with an infinite number of blades. Prandtl came up with the correction factor to correct the infinite number of blades:

$$F = \frac{2}{\pi} \cos^{-1}(e^{-f}) \quad (2.9)$$

where f :

$$f = \frac{B}{2} \frac{R-r}{r \sin(\phi)} \quad (2.10)$$

where B is number of blades, r is the local radial position, ϕ is the angle of flow, R is the blade radius. The momentum theory becomes no longer valid when the axial induction factor increases. Glauert correction model provides an empirical relations between the thrust coefficient C_T and the induction factor a :

$$C_T = \begin{cases} 4a(1-a)F & a \leq \frac{1}{3} \\ 4a(1 - \frac{1}{4}(5-3a)a)F & a > \frac{1}{3} \end{cases} \quad (2.11)$$

In QBlade, the user can choose any combination from the list of correction models during the simulation process as shown in Figure 2.6. The details of these algorithms can be found in [18, 30–32].

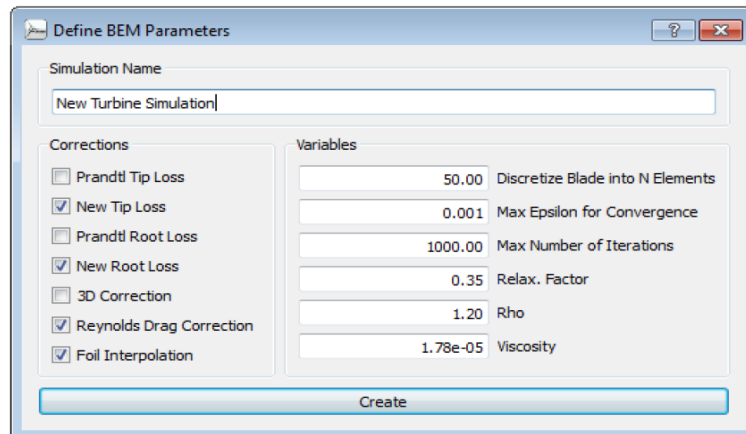


Figure 2.6: The BEM Parameters Dialog.

To design a HAWT in QBlade, the following general steps must be followed:

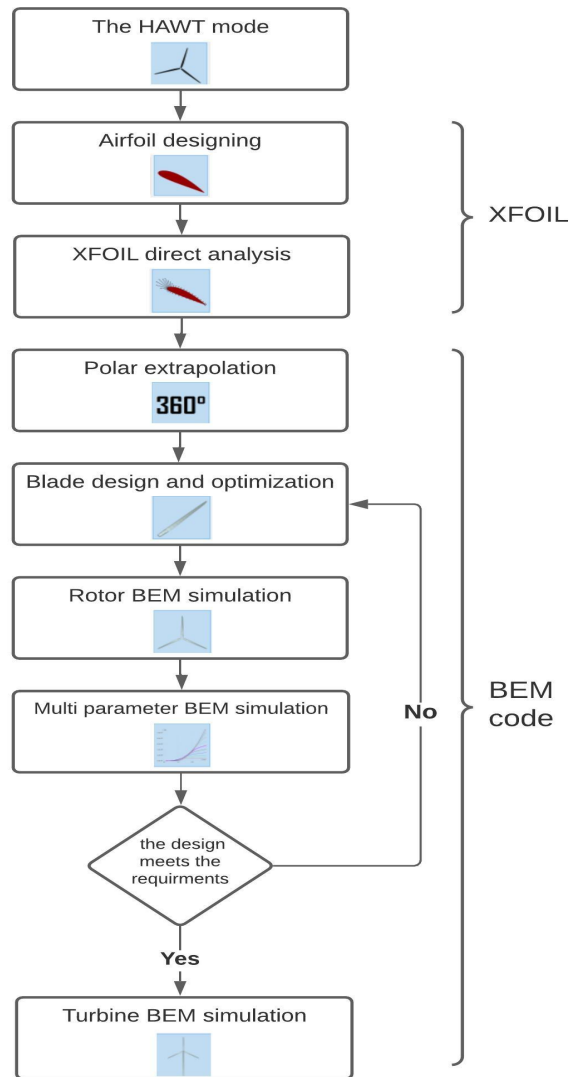


Figure 2.7: Data Flow in QBlade.

2.5 Computational Fluid Dynamics (CFD) Method

In the previous section, the BEM method failed to simulate the 3D flow. Moreover, it assumed that no interaction between the blade segments. Thus, the CFD approach is an alternative method that provides a deeper understanding of the nature of the 3D flow. In previous years, computational fluid dynamics (CFD) for wind turbine applications was primarily based on solving the incompressible Navier-Stokes equations [33]. In

wind turbine applications, the flow is assumed incompressible since the atmospheric velocities ranging from 5-25 m/s. So, the incompressible Navier-Stokes equations are:

$$\nabla \cdot \mathbf{u} = 0 \quad (2.12)$$

$$\frac{\partial \mathbf{u}}{\partial t} + (\mathbf{u} \cdot \nabla) \mathbf{u} = -\frac{1}{\rho} \nabla p + \nu \nabla^2 \mathbf{u} \quad (2.13)$$

Along with other equations such as the Boussinesq approximation equations and empirical viscosity equations, a complete model for the description of turbulent flows is established. This set of equations are difficult to solve because of the non-linear convective term. Depending on the Reynolds number, the turbulent scales are very small inside the boundary layer of the blade and very large in the atmospheric boundary layer. Thus, direct numerical simulation (DNS) that resolves all scales in the flow is both costly and time-consuming. Turbulence models provide reduction in the cost while resolving the small scales based on large scales behaviour [34]. There are several existing models encountered in wind energy applications for turbulence modelling such as standard $k-\epsilon$ model, $k-\omega$ model, $k-\omega$ (SST) model and Spalart-Allmaras (S-A) model. Menter [35] has developed the shear-stress transport (SST) $k-\omega$ model to smartly blend the robust and accurate formulation of the $k-\omega$ model near the wall area with the free-stream independence $k-\epsilon$ model in the far field. The $k-\omega$ (SST) model is more precise near the blade surfaces. This model matches with experimental results as compared to other turbulence models [36]. Cantoni [24] study the airfoil S809 for different turbulence models with a range of flap angles from -10° to 10° . Compared with the experimental results, Cantoni found that The SST $k-\omega$ turbulence model was much more accurate than the other models in predicting the flow conditions. The transition SST model is based on coupling the SST $k-\omega$ transport equations with two additional transport equations, one for intermittency γ and the other for the parameters of transition onset. This model is

more time-consuming because of the two additional equations.

Another important factor affects the simulation results is the meshing quality. Meshing is nothing more than a discrete representation of the geometry. Mesh generation is the most difficult and time-consuming in the entire CFD simulation process. Ansys ICEM CFD meshing software is preferable and easy to generate a high-quality surface or volume mesh with minimal effort. To solve the boundary layer around the surface of the blade, the boundary layer mesh must be of adequate resolution. The dimensionless cell Y PLUS should be less than or close to one to ensure a better solution in the boundary flow. The "converged" solution would be more accurate if the mesh and boundary conditions are accurate.

The wind turbine CFD simulation requires no empirical corrections models compared with the BEM method. The CFD simulation can also be used to validate existing correction models and development of new models. In addition, complex phenomena like stall delay and 3D complex flow can be solved with high fidelity. The effects of tower, hub, nacelle and yaw mechanism can be added to the rotor in the CFD simulation to provide a better understanding of a complete HAWT.

2.5.1 Previous Studies in the Literature

In recent years, researches on small scale HAWT using experimental and computational approaches has grown in interest. This subsection describes researches on the performance analysis of small-scale HAWTs conducted by various authors.

M. Hasan. [37] have performed an analysis on a small scale HAWT. First, the BEM method is used to design a 5m blade with a single airfoil S833 using Matlab coding. Next, the study focused on increasing blade performance by changing the blade

geometry with mixed airfoils configuration. The BEM method is validated by CFD method. The hub and tower were not included in the study. The blade with mixed airfoils has a better performance than a blade with single airfoil. Md. Robiul Islam [38] designed 1m blade with QBlade software and validated with Matlab. With a cut-in wind speed of 2 m/s, the QBlade results reveal that the rotor can extract up to 48% of wind energy.

Refan et al. [39] tested the aerodynamic performance of a small scale HAWT rotor with a radius of 1.1 m experimentally and theoretically to assess if the BEM theory could be used to describe the rotor performance for small HAWTs. When the theoretical and experimental data are compared, it was clear that the prediction of the BEM theory is within an acceptable range of accuracy. Tobin, N. [40] tested The effects of winglets on the power and thrust coefficients of a HAWT model experimentally in the wind tunnel. The results show an improvements in the power and thrust coefficients of 8% and 15% respectively for the wingletted case. Ozair, M. [41] designed a 5kW small-scale HAWT with a linear taper and nonlinear twist blade. The BEM method is used for the design process and the CFD method is used to determine the blade performance. At wind velocity of 10 m/s, C_p is determined to be 0.48.

Troldborg [42] studied in his master thesis three shapes of flaps applied to wind turbine blades; soft curved, strongly curved and rigid flap. Troldborg recommended to use the short flaps because it have been shown to be more robust than longer flaps and they can operate at a higher lift to drag ratio. In addition, short flaps are subjected to lower flap hinge moments. The movable flap is hinged so that it can move to pressure side and suction side of the airfoil. However, the hinged flap is accompanied with a flap hinge moment, and with increasing flap deflection angle and increasing the gap between the

main blade and the flap, noise will increase [43]. There are several studies discussed the active/passive flow control for the wind turbines applications, such as a blade with a movable leading/trailing edge flap and active/passive Gurney flap. These studies are done by using experimental method and computational method such as a 2D and a 3D modelling on CFD. The predicted slow response of the trailing edge flap and the noise produced by the gap between the main blade and the flap are the main problems when dealing with the flexible trailing edge flaps [24]. However, there is no study on the investigation of a wind turbine blade with a stationary, sealed gap (gapless) trailing edge flap at fixed angle for the entire life time of the wind turbine.

Cantoni [24], discussed the influence of the movable trailing edge flap on the aerodynamic loads. A study of the unsteady aerodynamic loads caused by a wind gust passing over the blades is assessed. The airfoil S809 is used, and the flap length was set at 20% of the airfoil chord, with a 10 mm gap distance between the airfoil and the flap. Cantoni noticed from the 2D study that the lift increases proportionally as the wind speed velocity increases, particularly in the configuration with the flap moving to the pressure side (clockwise angle).

The non-standard modelling techniques are required for advanced wind turbine blade design. The traditional blade planforms may be rapidly modelled using BEM. Its capability to evaluate non-conventional or non-planar blade planforms, including the effects of blade sweep, winglet, active flaps and dihedral, is nonetheless restricted. In this study, two similar turbines with and without fixed flap with the same radius were operated under the same conditions. Thus, the BEM method is still applicable when dealing with a fixed flap.

Chapter 3

METHODOLOGY

A HAWT rotor has more than one blade with a set of airfoil shapes. Under the flow conditions, the efficiency of the rotor is determined by the airfoil, blade twist, and chord length. It is essential to emphasize the objectives while optimizing the design. A wind turbine rotor is typically designed for a variety of objectives and purposes. Firstly, it was designed to give a maximum design power by choosing different airfoil shapes and series such as NACA airfoils. Each airfoil has lift, drag, moment and thickness different than the others. Under certain conditions, this method produced an aerodynamically efficient rotor, but it produced less-than-optimal performance under off-design conditions.

Next, rotors were designed to have maximum output energy. This method requires a good control system over a range of wind speeds. Rotors have recently been designed to have the lowest possible energy cost. In this method, The multidisciplinary design approach is implemented for all significant components of the wind turbine. This section provides a detailed discussion and investigation of designing a fixed pitch-variable speed (FPVS), stall regulated, horizontal axis wind turbines with and without a trailing edge flap application using the BEM method and CFD method.

3.1 Turbine Blade Design: 1st Configuration

In this analysis, a small horizontal axis wind turbine will be installed. Since this turbine has a fixed pitch, it does not require a pitch mechanism. All the aerodynamic data and design parameters will be presented and discussed for this configuration. Small-

scale wind turbines are simpler than large-scale wind turbines, which means that some components can be eliminated from the structure. A schematic representation of a small scale HAWT is shown in Figure 3.1.

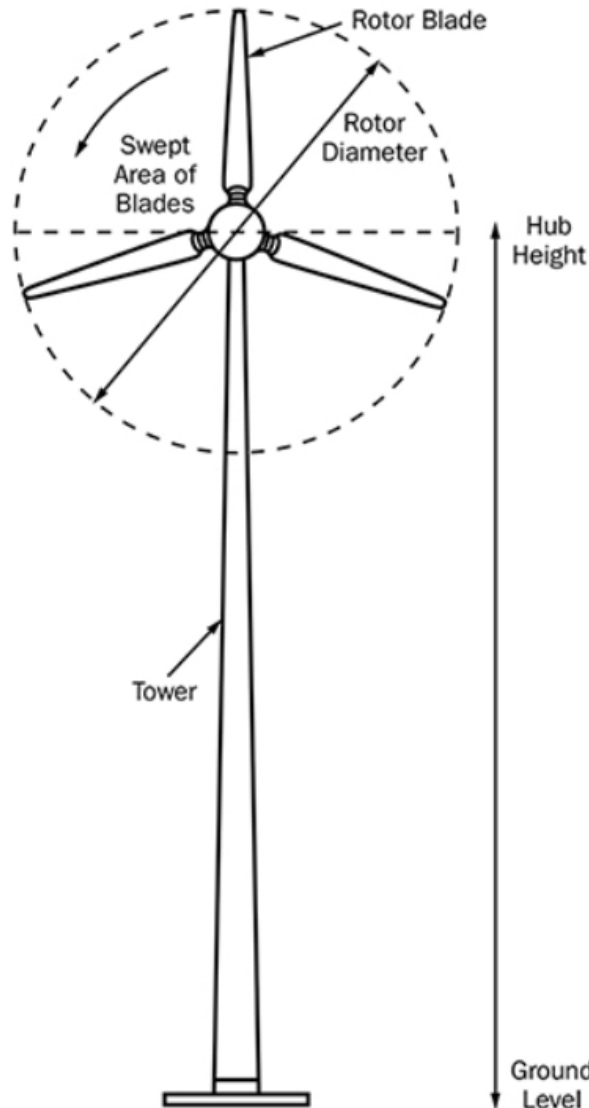


Figure 3.1: A schematic representation of a small scale HAWT [37]

3.1.1 Wind Turbine Power

The rated power is the first parameter to consider during the design process. Small-scale HAWT have a maximum rated power of 50 kW, whereas a large wind turbines have rated power of 1-3 MW when the wind velocity is in the designed range. The designed power coefficient C_{PD} for small scale HAWT is usually in the range of 0.4-

0.5. In this case, the designed power will be 10 kW at rated wind speed, and the assumed designed power coefficient C_{PD} is 0.45.

3.1.2 Wind Speed

The fixed pitch-variable speed (FPVS) wind turbine operates at maximum power coefficient C_P from the cut-in to its rated wind speed. The rated wind speed U_{rated} , is the speed when the turbine reaches its rated power P_{rated} , whereas the designed wind speed is the speed when the turbine operates at maximum power coefficient C_P . Thus, the rated wind speed and the design wind speed in this work will be the same as 8 m/s for FPVS speed wind turbine.

3.1.3 Rotor Radius

The rotor swept area determines the power output of a wind turbine. The length of the rotor blades must be increased to increase the power output. the power output of the turbine can be calculated as:

$$P_{out} = \frac{1}{2} \rho A U^3 \eta_{mech} C_P \quad (3.1)$$

Thus the radius of the blade can be estimated as:

$$R = \sqrt{\frac{2P_D}{C_{PD} \eta_{mech} \rho \pi U_D^3}} \quad (3.2)$$

Where P_D is the designed power, η_{mech} is the mechanical efficiency (including electrical efficiency), ρ is the air density, C_{PD} is the designed power coefficient and U_D is the designed wind speed. The shaft of the turbine are mounted to a gear box which control the blade rotational speed. Some energy are lost at the gear trains and the bearings which support the shaft due to the friction. The gearbox shaft drives the generator, which converts mechanical energy into electricity. The generator also have losses which refers to electrical efficiency. Figure 3.2 shows the power losses in the components of the wind turbine.

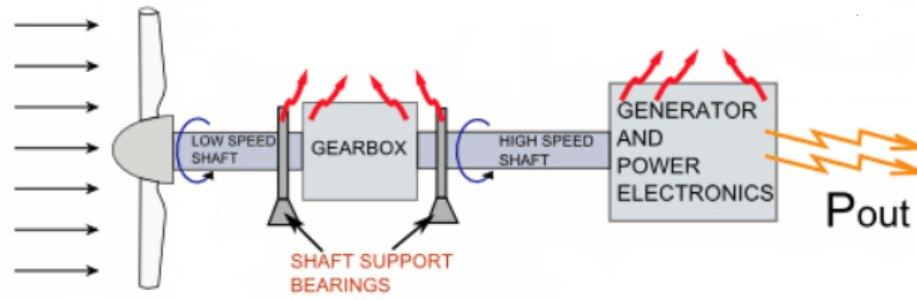


Figure 3.2: The Losses of Power in Wind Turbine Components [44].

In this case, the combined electrical and mechanical efficiency, η_{mech} , is considered to be 0.9. From equation (3.2) and by using 10 kW for P_D , 0.45 for C_{PD} , 0.9 for η_{mech} , 1.225 kg/m^3 for the density and 8 m/s designed wind speed U_D , the radius, R , is calculated to be 5m.

3.1.4 Aerodynamic Characteristics of S809 Airfoil

In the early 1980s, the researches were focused on improving the blades performance of HAWT by airfoil selection task [45]. This method gave a slight difference in the performance compared with optimizing the blade twist and taper. As a result, the task of selecting airfoils for wind turbines received little consideration. Hence, airfoils used in the aviation industry such as the NACA series, were selected for wind turbine applications. To ensure that the blades of large-scale turbines were strong enough, thick airfoils were used in the late 1990s. Designers at National Renewable Energy Laboratory (NREL) have designed new series (S-series) for wind turbine applications. This new series that tested on blades with 8 m long has shown increasing annual yield by having a greater rotor radius without increasing in peak power [46]. Because of their smooth stall nature, these airfoils are common in stall-regulated wind turbine blades. Similarly, new airfoil series were designed and tested at the Delft University of Technology specifically for HAWT applications [47].

The objective of this study is not to select or design the best airfoil for a wind turbine. Obviously, by using different airfoils, the power and performance will be different. The NREL in the USA was one of the first institutions to study wind turbine airfoils in details. the S-series contains 35 airfoils with majority of them are thick [48]. In this study, the most well-known NREL airfoil S809 is used. This airfoil has maximum thickness of 21% at 39.5% of the chord and maximum camber of 1% at 82.3% of the chord. Figure 3.3 shows the S809 airfoil.

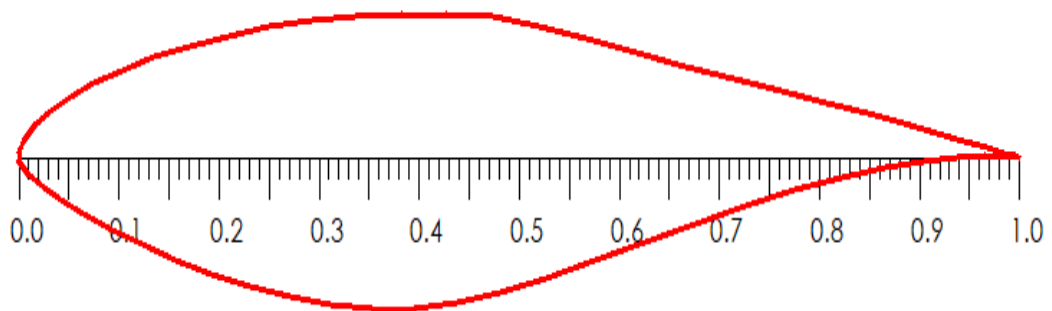


Figure 3.3: The S809 Airfoil by NREL.

Before starting the aerodynamic analysis of S809 airfoil, validation between XFOIL data and wind tunnel experimental data are presented. The experimental data from Delft University of Technology (TUDelft) wind tunnel for Reynolds number of 1×10^6 are used for validation [25]. The lift coefficient C_L and drag coefficient C_D versus angle of attack α are shown in Figures 3.4 and 3.5. In most cases, the wind turbine is designed to run at the angle of attack which gives the maximum lift to drag ratio.

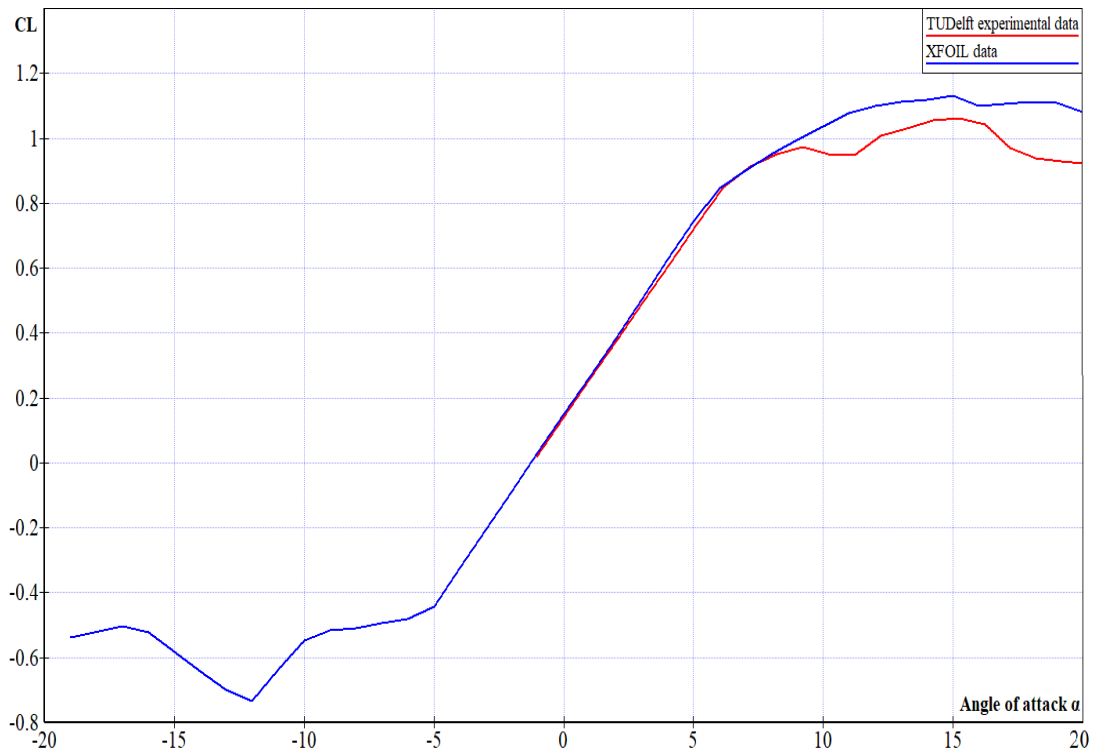


Figure 3.4: Comparison of XFOIL Lift Coefficient and TUDelft Wind Tunnel Lift Coefficient for S809 Airfoil.

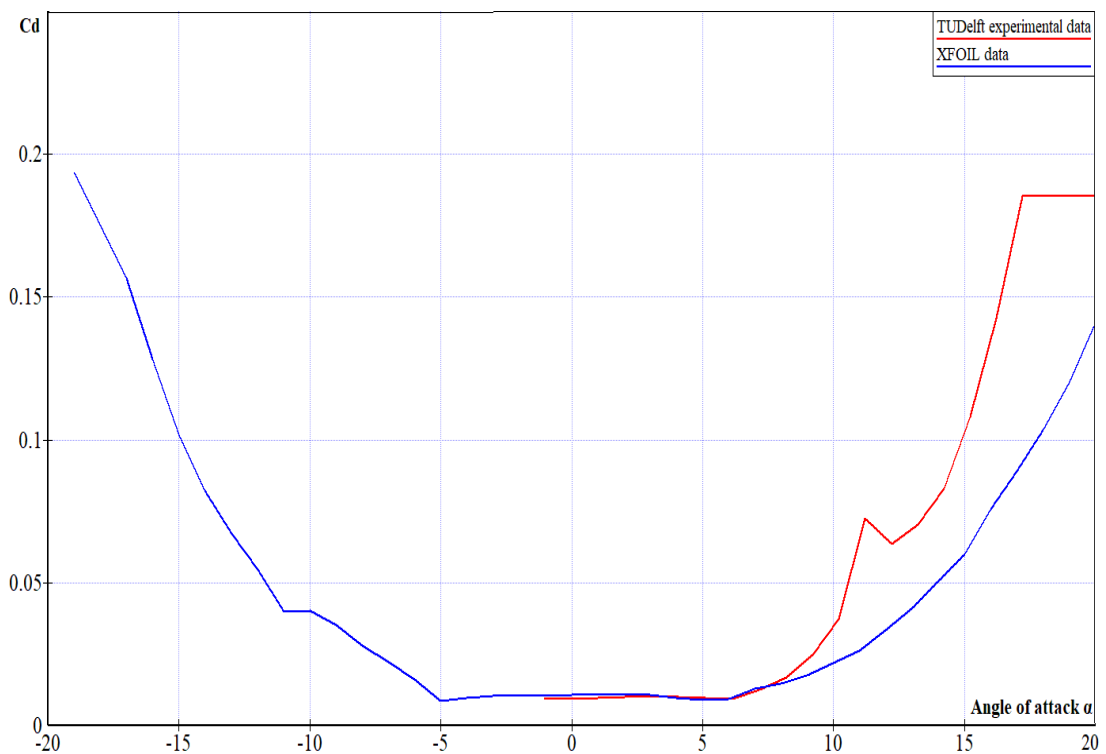


Figure 3.5: Comparison of XFOIL Drag Coefficient and TUDelft Wind Tunnel Drag Coefficient for S809 Airfoil.

From the two Figures above, it is clear that XFOIL gives the same measurements as the wind tunnel up to 10° AoA. Above 10° AoA, the XFOIL gives higher values of lift coefficient and lower values of drag coefficient compared with wind tunnel measurements for Reynolds number (Re) of 1×10^6 . XFOIL is considered to have a low fidelity for higher values of Reynolds number, making it particularly suitable for low Reynolds number (Re) airfoils [49]. Wind turbine blades work at a considerably lower Reynolds number (Re) compared with an airplane wing. As a result, XFOIL can be trusted for aerodynamic analysis in this work. The airfoil S809 is tested in "XFOIL Direct Analysis" tab In QBlade software, the Reynolds number varies from 2×10^5 to 1×10^6 . The Ncrit is set to 9 and the Mach number (Ma) is set to be 0.02. The Polar curves for S809 airfoil is shown in Figure 3.6.

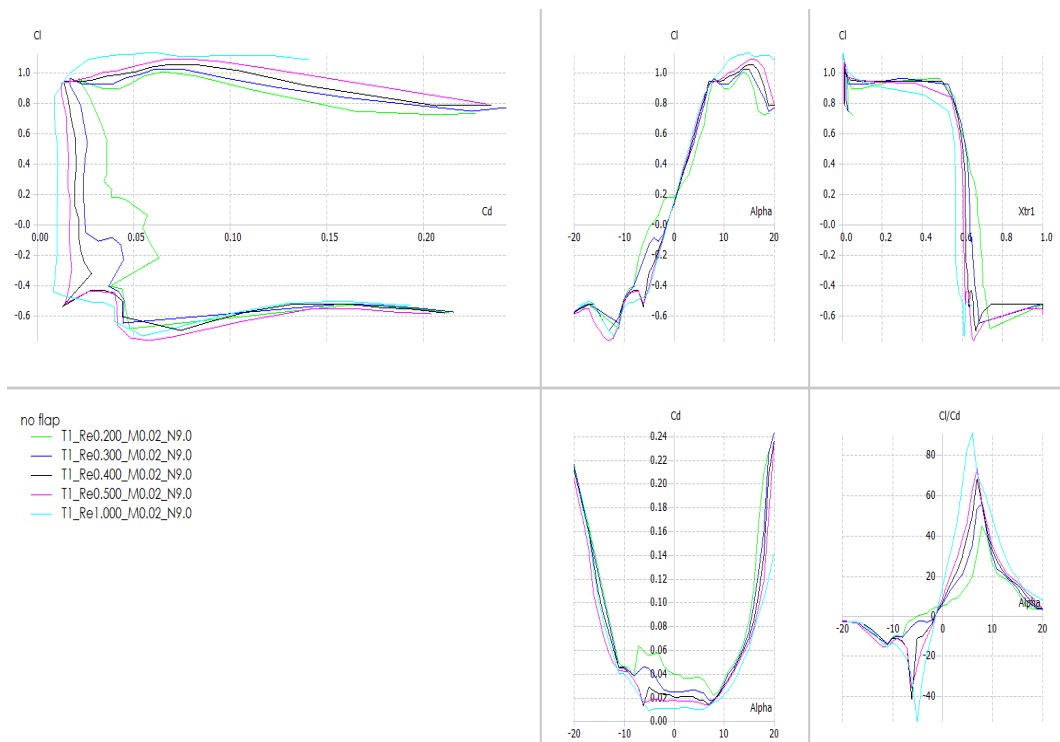


Figure 3.6: The Polar curves for S809 Airfoil In QBlade "XFOIL Direct Analysis" Tab.

Airfoils for turbine blades are often designed to be used at low AoA, with relatively high lift coefficient and low drag coefficient. At various Reynolds numbers, there are major variations in airfoil behaviour. In comparison to inertial forces, viscous forces rise in magnitude as Reynolds numbers decreases. For accurate study of a wind turbine rotor system, wind turbine designer must ensure that enough Reynolds number data are available. In this study, five different values of Reynolds numbers are tested. The lift and drag coefficient and coefficient of lift to drag ratio ($\frac{C_L}{C_D}$) are presented versus AoA in the Figures 3.7, 3.8 and 3.9. However, typical Reynolds numbers vary between 5×10^5 and 1×10^7 for the wind turbines applications [50]. In this analysis, the Reynolds number will be chosen to have a low value, resulting in a high lift coefficient and a low drag coefficient. Thus, a Reynolds number of 500 000 is chosen.

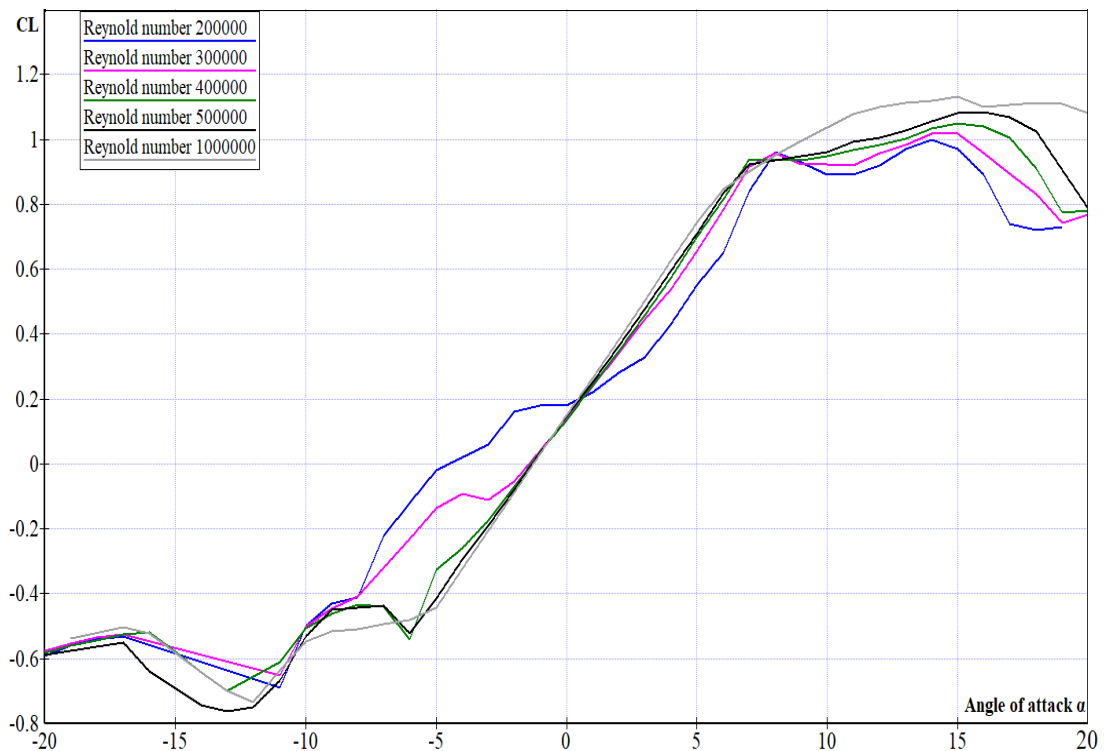


Figure 3.7: Coefficient of Lift versus AoA for Different Values of Reynolds Number.

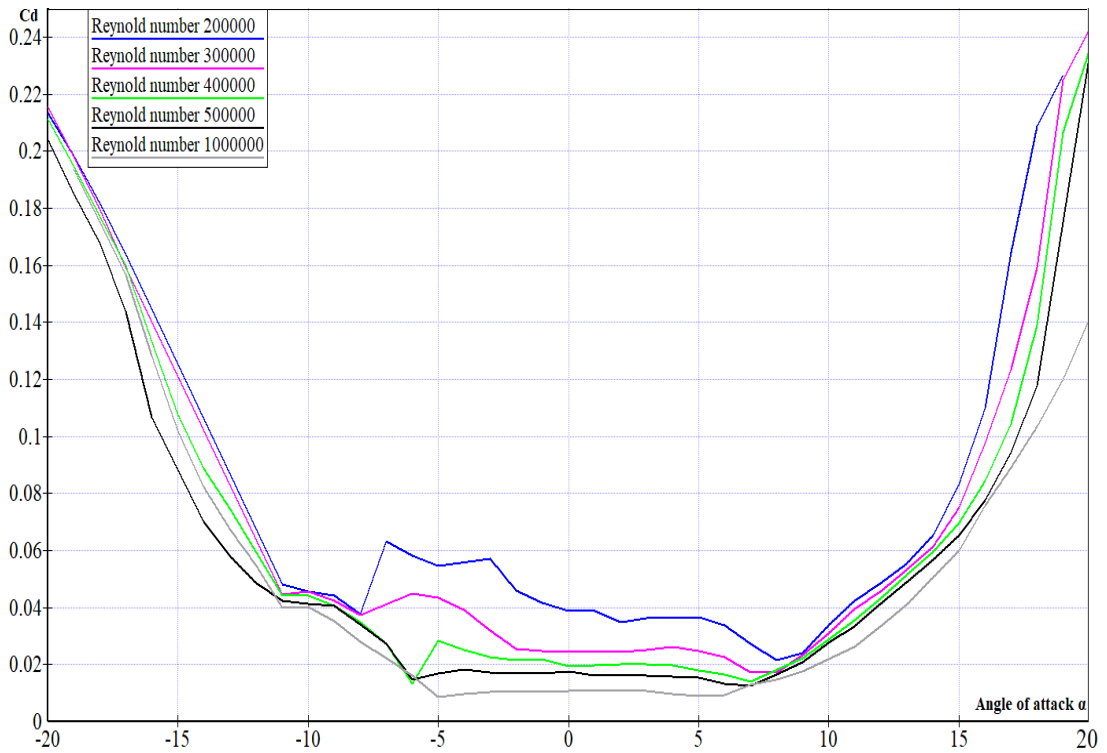


Figure 3.8: Coefficient of Drag versus AoA for Different Values of Reynolds Number.

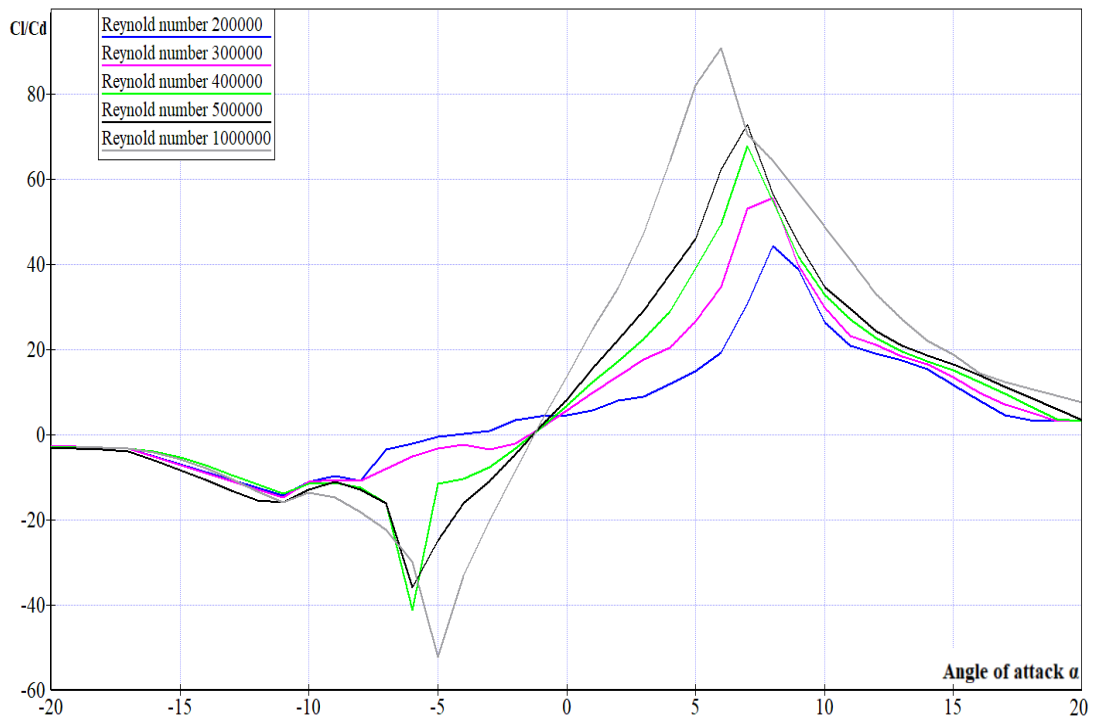


Figure 3.9: Lift to Drag Ratio versus AoA for Different Values of Reynolds Number.

From the polar curves above, at a given value of AoA, the lift coefficient increases as the Reynolds number increases. Airfoils for wind turbine applications are often designed to be used at low AoA, with relatively high lift coefficient and low drag coefficient. At Reynolds number of 500 000 and AoA of 7°, the lift coefficient of 0.93 is considerably high, whereas the drag coefficient of 0.013 is low enough. From the Figure 3.9, the maximum coefficient of lift to drag ratio $(\frac{C_L}{C_D})_{max}$ occurs at 6° to 7° AoA for all tested values of Reynolds number. At 7° AoA and Reynolds number of 500 000, the $(\frac{C_L}{C_D})_{max}$ equal to 72.86. Thus, in this work, the designed AoA and $(\frac{C_L}{C_D})_{max}$ are considered to be 7° and 72.86 respectively.

After analyzing the S809 airfoil in XFOIL, the polar's AoA must be extrapolated 360°. In QBlade, users are allowed to extrapolate the polar curves with Montgomery extrapolation algorithm or Viterna-Corrigan model. In this study, Montgomery extrapolation algorithm is used with slope of 0.11 and the drag coefficient at 90° AoA (C_{D90}) of 1.8, then the extrapolated polar curves are shown in Figure 3.10.

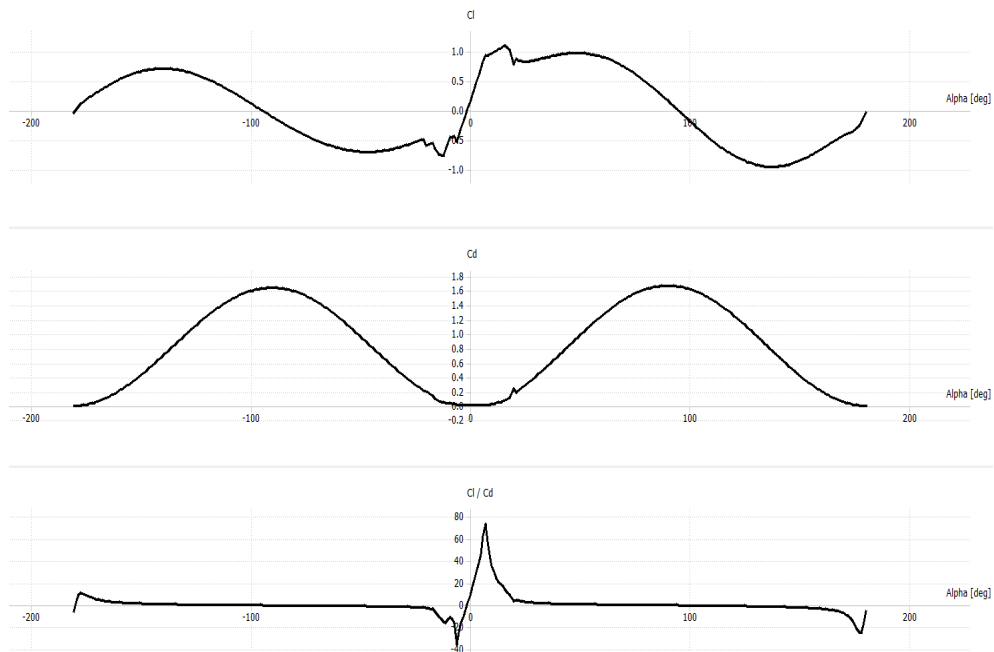


Figure 3.10: Extrapolation of Polar Curves.

3.1.5 Design Tip Speed Ratio

The rotor blades of a stall-regulated wind turbine are fixed, allowing the turbine to operate efficiently only at the design wind speed. The blade length is proportional to the design wind speed and rated power. Tip speed ratio λ , refers to the ratio between the blade's tip speed and the wind speed, $\lambda = \frac{\omega R}{U}$. Having a high tip speed ratio is normally desirable. A low solidity σ (the ratio between the chord length of the blade and spacing) is caused by a high tip speed ratio. Thus, the blades are slender and less expansive. However, a higher tip speed is associated with increased turbine aerodynamic noise. For three blades rotor, the turbine will operate at tip speed ratio λ between 4-10. the relation between the number of blades B and λ is presented in table 3.1.

Table 3.1: The Relation between the Number of blades and the Tip Speed Ratio.

Tip Speed Ratio λ	Number of blades B
1	8-24
2	6-12
3	3-6
4	3-4
4-10	1-3

To select an initial guess of tip speed ratio, Wilson estimated the overall power coefficient for a turbine with an optimal blade shape and a finite number of blades [51]. The empirical relation provided by Wilson is accurate to within 0.5% for tip speed ratio $4 \leq \lambda \leq 20$, lift to drag ratio $25 \leq \frac{C_L}{C_D} < \infty$, and number of blades $1 \leq B \leq 3$. The Wilson empirical relation :

$$C_{P,max} = \left(\frac{16}{27}\right)\lambda \left[\lambda + \frac{1.32 + \left(\frac{\lambda-8}{20}\right)^2}{B^{\frac{3}{2}}} \right]^{-1} - \frac{(0.57)\lambda^2}{\left(\frac{C_L}{C_D}\right) \cdot \left(\lambda + \frac{1}{2B}\right)} \quad (3.3)$$

Similarly, Çetin proposed a related method for determining the optimal tip speed ratio

[52]. The Çetin empirical relation:

$$C_{P,max} = \left(\frac{16}{27}\right) \cdot \left(1 - \frac{\lambda}{\left(\frac{C_L}{C_D}\right)}\right) \cdot \left(1 - \frac{1.84}{B \cdot \lambda}\right) \quad (3.4)$$

From the equations (3.3) and (3.4), the relation between the power coefficient and the tip speed ratio for Reynolds number of 500 000 is given in the table 3.2 ad Figure 3.11.

Table 3.2: The Power Coefficient at Reynolds number of 500 000 .

Tip Speed Ratio λ	$C_{P,max}$ Çetin relation	$C_{P,max}$ Wilson relation
1	0.225993	-
2	0.399591	-
3	0.452035	-
4	0.474191	0.479304
5	0.484231	0.486998
6	0.488213	0.489861
7	0.488733	0.489878
8	0.487091	0.487742
9	0.484005	0.484371
10	0.479911	0.480038

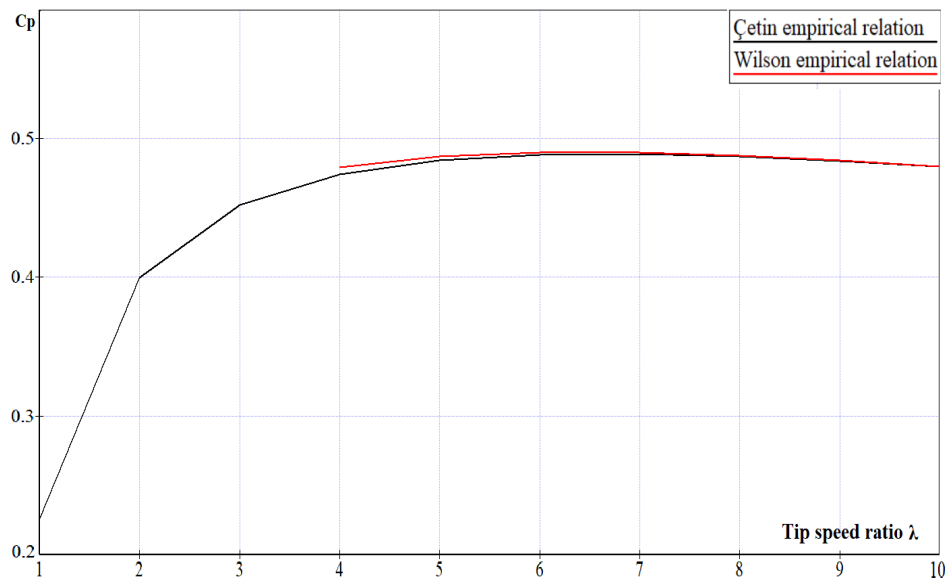


Figure 3.11: The Relation between the Power Coefficient and the Tip Speed Ratio.

From the tip speed ratio from 5 to 10, both Wilson and Çetin empirical relations give the same power coefficient, as seen in Figure 3.11. Furthermore, at a tip speed ratio of 7, the power coefficient reaches its optimum value. As a result, the design tip speed ratio will be considered as 7.

3.1.6 Blade Design and Optimization

In this analysis, the blade design and optimization is done in QBlade software. The blade is discretized into a number of segments. The torque and thrust of each segments are calculated, then the forces of each segments can be added up to give the final torque and thrust. The position, twist, chord, airfoil, and the related 360 polar describe each segment. The number of blades and the hub radius have to be defined in the design process. The blade is optimized in the optimization dialog in QBlade as shown in Figure 3.12.

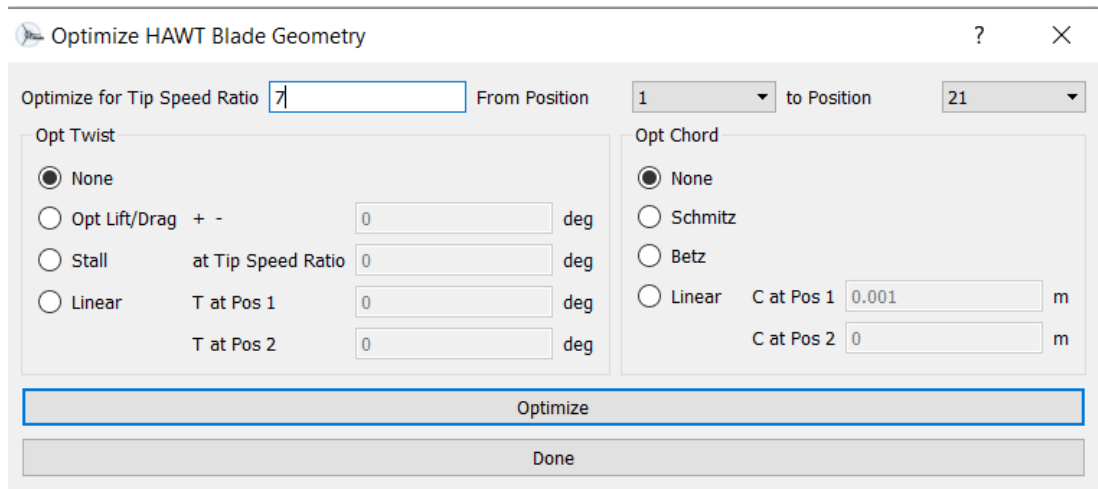


Figure 3.12: Optimizing HAWT Blade Geometry Dialog.

From the Figure 3.12, the user has to choose λ_o and the positions to be optimized. For each segment, the assumed inflow angle is calculated using tip speed ratio λ_o :

$$\alpha_{loc} = \tan^{-1} \left(\frac{1}{\lambda_{o,loc}} \cdot \frac{2}{3} \right) \quad (3.5)$$

where α_{loc} is the local inflow angle of attack for each segment. For twist optimization,

the user has to choose one of the three options: Optimize for lift to drag ratio, optimize for stall, and linear twist optimization. The first option, adjust the twist angle to an AoA which gives the maximum lift to drag ratio (in this case, the AoA is 7°). According to a stall-regulated HAWT, optimizing for stall option in the optimization dialog is a good place to start the optimization process. Optimizing for stall option set the twist so that all of the segments encounter stall at specified λ_\circ at the same time. Linear twist optimization set a linear twist profile for the blade which makes it easy to manufacture [37].

Similarly, the optimization of the chord can be done according to Schmitz and Betz [53]. the chord for each method is calculated as:

$$c_{Schmitz}(r) = \frac{16\pi r}{BC_L} \cdot \sin^2\left(\frac{1}{3}\tan^{-1}\left(\frac{R}{\lambda_\circ r}\right)\right) \quad (3.6)$$

$$c_{Betz}(r) = \frac{16}{9} \frac{\pi R}{BC_L \lambda_\circ} \cdot \frac{1}{\sqrt{(\lambda_\circ \frac{r}{R})^2 + \frac{4}{9}}} \quad (3.7)$$

Where r is the local radius. Betz and Schmitz have identical conditions, but the latter has a lower thrust coefficient, resulting in lower power for small wind turbines [54]. It is worth noting that C_L is calculated for each segment separately from the twist angle and λ_\circ . The Betz and Schmitz equations both result in high chord values in the root region, so the user has to check the value of solidity, $\sigma = \frac{cB}{2\pi r}$ to be less than unity. In this study, the blade of $5m$ is discretized into 21 equal segments, The hub radius is $0.2m$ and the number of blades is 3. In the optimization dialog, the value of λ_\circ is 7. The twist angle is optimized for stall, and the Schmitz method for the chord optimization is used. The design and optimization of the blades of wind turbines is an iterative process; the designer has to check the output power to meet the design requirements. After the design and optimization procedure is done, the blade radial position, chord, and twist angle are presented in table 3.3.

Table 3.3: The Blade Radial position, Chord, and Twist Angle Distribution of the 1st Configuration.

Radial distance (m)	Radial position (r/R)	Chord (m)	Twist angle
0.25	0.05	0.8047	41.0149
0.50	0.10	0.8013	28.7259
0.75	0.15	0.7269	20.1229
1.00	0.20	0.6438	14.0184
1.25	0.25	0.5693	9.5553
1.50	0.30	0.5064	6.1878
1.75	0.35	0.4540	3.5731
2.00	0.40	0.4104	1.4923
2.25	0.45	0.3738	-0.1988
2.50	0.50	0.3428	-1.5982
2.75	0.55	0.3163	-2.7739
3.00	0.60	0.2935	-3.7749
3.25	0.65	0.2736	-4.6369
3.50	0.70	0.2562	-5.3866
3.75	0.75	0.2408	-6.0444
4.00	0.80	0.2271	-6.6262
4.25	0.85	0.2148	-7.1442
4.50	0.90	0.2038	-7.6084
4.75	0.95	0.1938	-8.0266
5.00	1.00	0.1848	-8.4054

The blade of the rotor wind turbine is made of a single airfoil S809 only. The 360° polar at Reynolds number of 500 000 is used during the design process in QBlade to calculate the aerodynamic coefficients for each segment. The blade is twisted to a positive angle at the root and a negative angle at the tip. The circular foil with a drag coefficient of 1.2 and zero lift coefficient is used at blade root. The 3D blade geometry is exported from the QBlade in .STL format to CAD software. The rotor blade and the wind turbine rotor are shown in Figures 3.13 and 3.14.

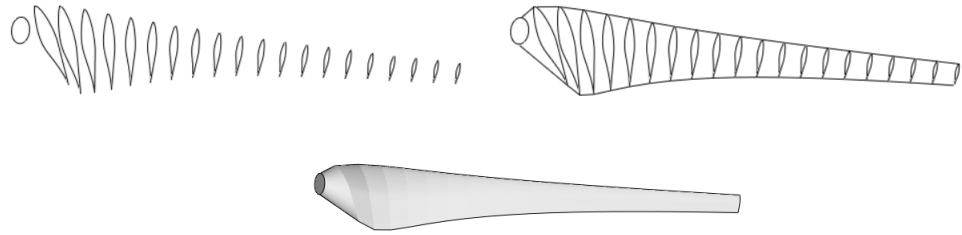


Figure 3.13: The Final Design of the 1st Blade Configuration.

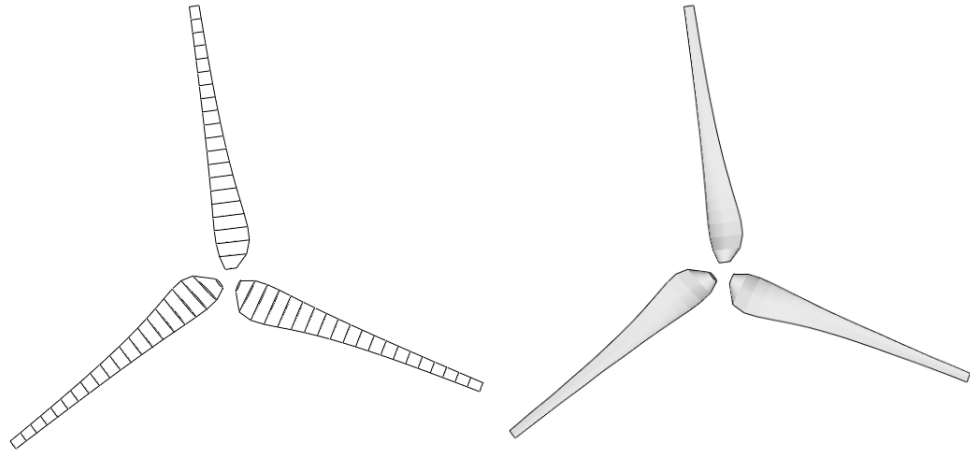


Figure 3.14: The Rotor Model of HAWT.

Finally, it is important to review all the design parameters and the assumptions that required during the design process in the table 3.4. The chord and twist distribution of the 1st blade configuration is shown in the Figure 13.15.

Table 3.4: The Parameters and Assumptions of the 1st Blade Configuration.

Parameter	Value/option	Parameter	Value/option
Power (kW)	10	Design power coefficient	0.45
Wind speed (m/s)	8	Design tip speed ratio	7
Lift to drag Ratio	72.86	Design angle of attack (°)	7
Blade radius (m)	5	Number of blades B	3
Twist optimization	Stall	Chord optimization	Schmitz

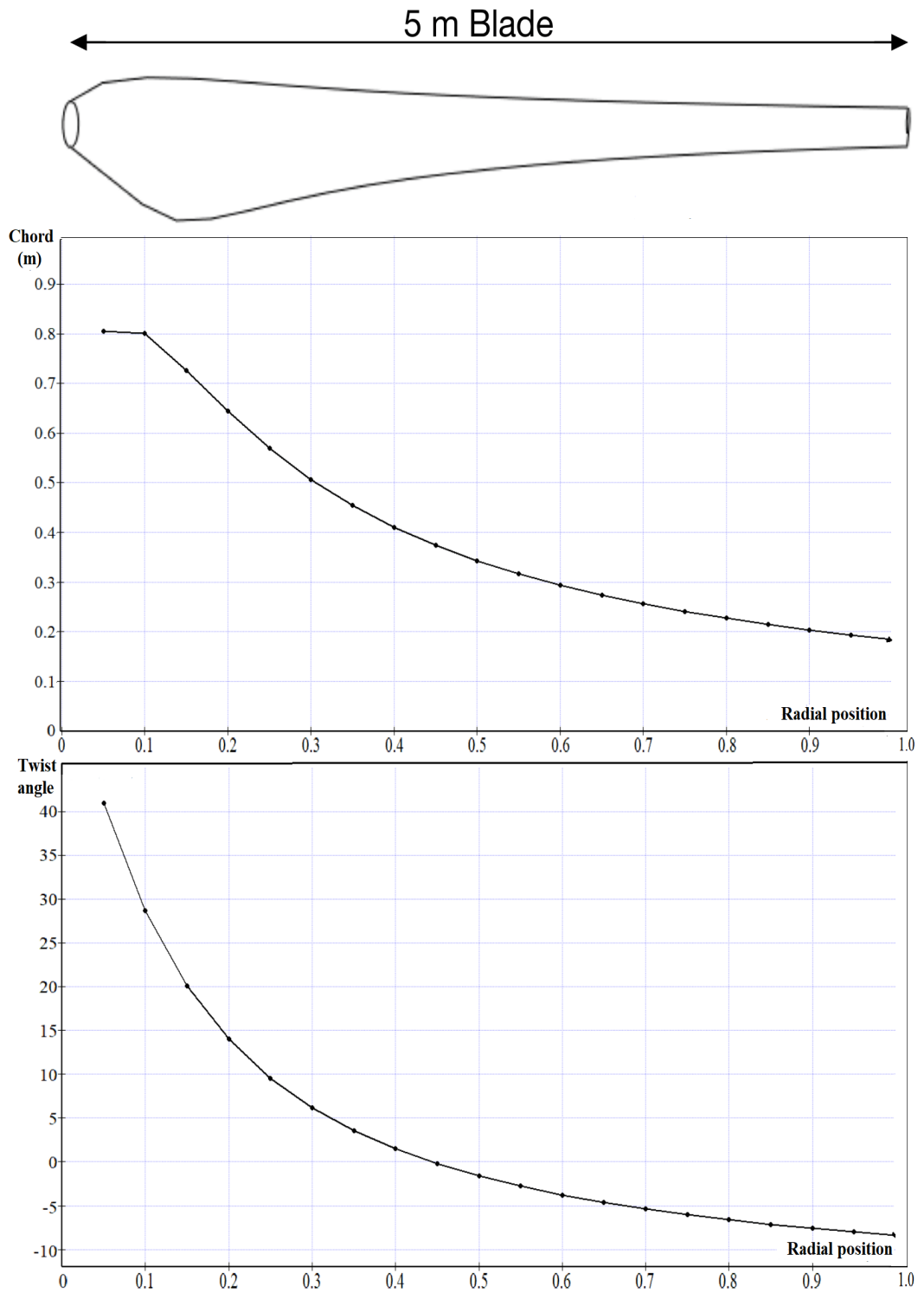


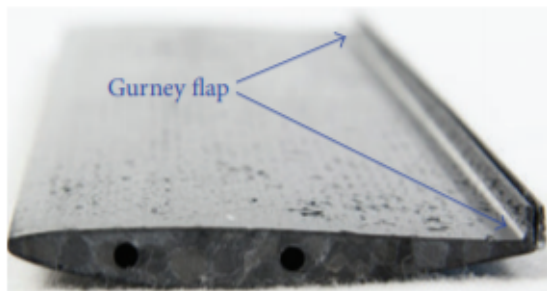
Figure 3.15: The Chord and Twist Distribution of the 1st Blade Configuration.

3.2 Turbine Blade Design: 2nd Configuration

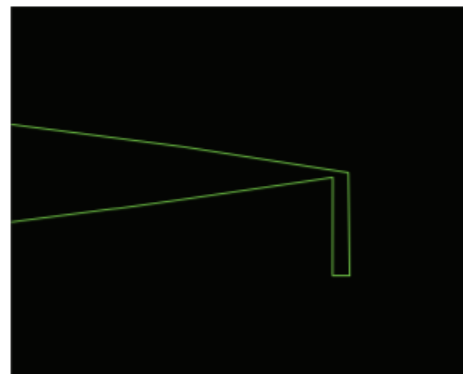
A detailed discussion on the design and optimization of a 5 m blade, stall-regulated HAWT using QBlade software was given in the previous section. Flaps are movable surfaces hinged on a wing or a blade that vary the airfoil camber to modify the aerodynamic performance. By varying the chordwise pressure distribution, these surfaces effectively improve the aerodynamic lift. The National Renewable Energy Laboratory (NREL) began working on flap-based control systems for wind turbines in the 1990s with the aim of improving efficiency [55, 56]. In wind turbines, flaps were used generally for load control. Cantoni [24], discussed the influence of the movable trailing edge flap on the aerodynamic loads. A study of the unsteady aerodynamic loads caused by a wind gust passing over the blades is assessed. The airfoil S809 is used, and the flap length was set at 20% of the airfoil chord, with a 10 mm gap distance between the airfoil and the flap. Cantoni noticed from the 2D study that the lift increases proportionally as the wind speed velocity increases, particularly in the configuration with the flap moving to the pressure side (clockwise angle).

Troldborg [42] studied in his master thesis three shapes of flaps applied to wind turbine blades; soft curved, strongly curved and rigid flap. Troldborg recommended to use the short flaps because it have been shown to be more robust than longer flaps and they can operate at a higher lift to drag ratio. In addition, short flaps are subjected to lower flap hinge moments. In term of noise generated, rigid flap was found to emit more noise than the other shapes. A detailed discussion of these flaps can be founded in reference [42]. The movable flap is hinged so that it can move to pressure side and suction side of the airfoil. However, the hinged flap is accompanied with a flap hinge moment, and with increasing flap deflection angle and increasing the gap between the main blade and the flap, noise will increase [43].

One of the well-known trailing edge flaps is a Gurney Flap. A Gurney flap (GF) is a microtab attached to the airfoil's pressure side near the trailing edge. Dan Gurney used a Gurney flap (GF) on the top trailing edge of his race car's rear wing to produce additional rear-end down force with a minor aerodynamic disturbance. According to wind turbines applications, Gurney flap has been tested experimentally and numerically and both method showed promising results [57–59]. A Gurney flap can be used for wind turbine to improve the lift to drag ratio, improve the starting performance of a wind turbine, and control the load by undeflected or deflected GF [58]. the Gurney flap is shown in Figure 3.16.



(a) 3D GF on the Trailing Edge Wing



(b) 2D Airfoil with a GF

Figure 3.16: 2D and 3D Gurney Flap [57]

It's worth noting that a full-scale wind turbine with a blade and a fixed trailing edge flap has never been tested in reality [60]. There are several studies discussed the active/passive flow control for the wind turbines applications, such as a blade with a movable leading/trailing edge flap and active/passive Gerney flap. Theses studies are done by using experimental method and computational method such as a 2D and a 3D modelling on CFD. The predicted slow response of the trailing edge flap and the noise produced by the gap between the main blade and the flap are the main problems when dealing with the flexible trailing edge flaps [24]. However, there is no study on the

investigation of a wind turbine blade with a sealed gap (gapless) trailing edge flap at fixed angle for the entire life time of the wind turbine. In addition, comparative simulation and validation of this type blade design (a blade with a fixed flap) in BEM method is new. In this section, the design and optimization of a blade accompanied with a flap adjusted at 10° clockwise will be discussed in details. Some design parameters will be kept the same as the 1st configuration to demonstrate the flap's impact. The trailing edge flap used in this analysis is a sealed gap flap that is stationary. Since XFOIL does not presume any gap, the flap is only accounted for the modified lift and drag coefficient tables that result from the XFOIL simulation of the airfoil S809. The flap with a fixed inclined angle of 10° clockwise will be the point of focus of this study. The flap is adjusted at 20% of the chord from the blade root to blade tip. the angle of flap will not be changed for the entire life time of the wind turbine. A 2D airfoil with flap and a 3D blade with flap will be studied in details. The power output, annual yield and the stall behaviour will be discussed. The sealed gap flap is shown in Figure 3.16

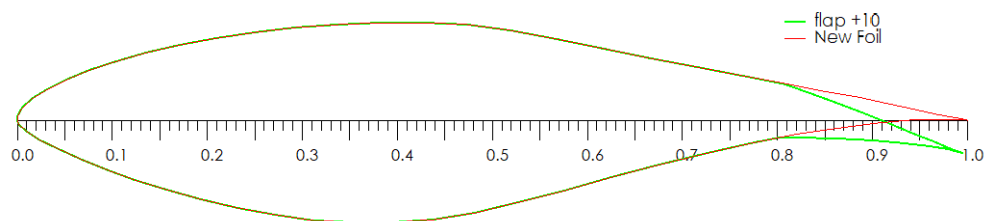


Figure 3.17: The S809 Airfoil with a Flap Angle of 10° .

The design procedure for the 2nd configuration is the same as the 1st configuration. First, the BEM method is done in QBlade software. In this configuration, some parameters will be kept the same as the 1st configuration such as Reynolds number, design power coefficient, rotor radius, hub radius and the design or rated wind speed. Moreover, the design and optimization options will be the same.

Wind turbine blades work at a considerably lower Reynolds number (Re) compared with an airplane wing. The XFOIL software is used to generate the polar curves for the airfoil S809 with a flap angle of 10° clockwise. The lift to drag ratio at Reynolds number of 500 000 is shown in Figure 3.18.

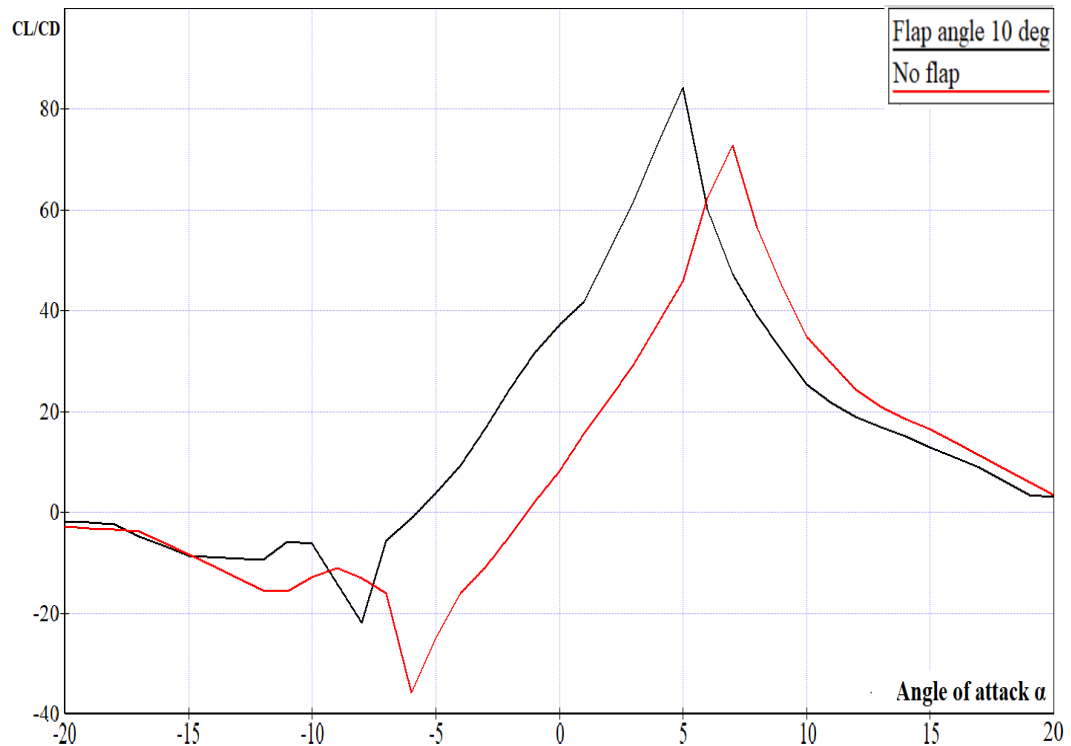


Figure 3.18: The Lift to Drag Ratio of the Airfoil S809 with and without Flap for Reynolds Number of 500 000.

It is clear from the Figure above that the maximum lift to drag ratio increases from 72.86 at 7° AoA for the airfoil without a flap to 84.22 at 5° AoA for the airfoil with a flap of 10° clockwise. Thus, the design AoA will be 5° and the $(\frac{C_L}{C_D})_{max}$ will be 84.22 for this configuration. The extrapolation algorithm (Montgomery) is used as the 1st configuration. By using equations (3.3) and (3.4), both empirical relations give the maximum power coefficient $C_{P,max}$ at tip speed ratio of 7. In the blade design and optimization dialog in QBlade, the same optimization options are used to optimize the twist angle and the chord length (optimization twist angle for stall, and Schmitz

optimization for chord). The blade radial position, chord, and twist angle are presented in Appendix A. Figure 3.19 shows the 2nd configuration of the blade.

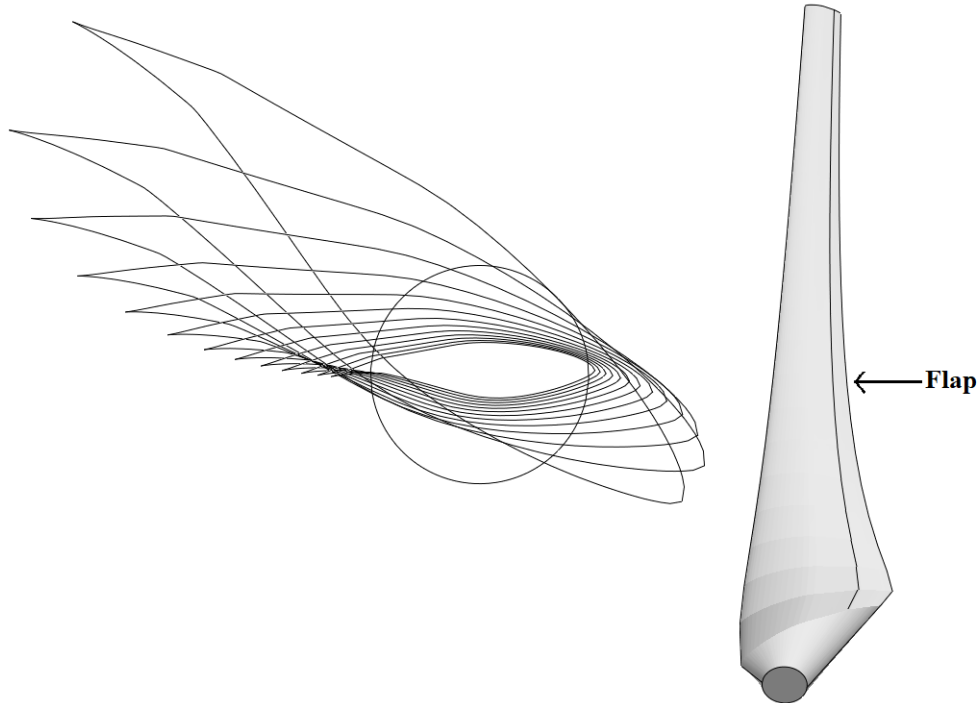


Figure 3.19: Airfoil Sections and a Blade with a Flap Angle of 10°.

3.3 Annual Yield

If a turbine simulation has been performed, the annual yield of the turbine can be calculated by setting an annual wind speed distribution using the WEIBULL distribution's parameters k and A . The wind speed changes continuously. Hence, to accurately predict the output of a wind turbine, it is important to know the local wind speed distribution for a specific site. The annual power is depend on the annual wind speed distribution. Xinzi [25] found that with a mean wind speed higher than 3 m/s, lower value of k gives higher annual yield. An acceptable approximation for the wind speed distribution is the Weibull distribution:

$$f(v) = \frac{k}{A} \left(\frac{v}{A}\right)^{k-1} \exp\left(-\left(\frac{v}{A}\right)^k\right) \quad (3.8)$$

Where k is the shape factor, and A (m/s) is the scale parameter proportional to the mean wind speed. The wind velocity is normally measured with an anemometer, and the mean wind speed is computed every 10 minutes. The data is sorted into classes. The frequency distribution can then be used to express the energy in the wind at a given location. The annual yield or the annual energy product (AEP) is calculated in this study in QBlade software by choosing the values of k and A for a specific location which is described by the WEIBULL distribution. The annual energy ($\frac{kW}{year}$) is calculated according to the relations (6.09 - 6.11) in the QBlade Manual in reference [61].

Levent [62] determined the WEIBULL parameters k and A at INCEK region-ANKARA (Latitude= 39.828540, Longitude=32.736850). The data is collected for a period of one year and for different heights (20m, 30m and 50m). Five different methods were used to determine the WEIBULL parameters. The values of WEIBULL parameters k and A are determined as 1.4743 and 3.303 respectively. The yearly average wind speed was found as 2.9859 m/s at height of 20m. In this study, the assumed hub height is twice the diameter of the rotor which is also 20m. The Weibull distribution of wind speed at height of 20m at INCEK region-ANKARA is shown in Figure 3.20.

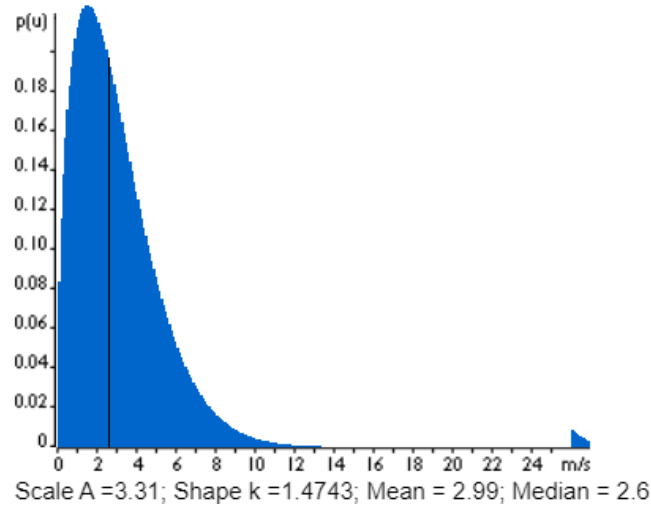


Figure 3.20: The Weibull Distribution of Wind Speed at Height of 20m at INCEK Region-ANKARA.

3.4 CFD Method

In this section, the 2D CFD study is done for the airfoil S809 with and without flap. Two turbulence models are applied and the comparison between XFOIL, experimental and CFD results is presented. Moreover, the geometry of the 2nd configuration blade is imported into ICEM CFD and the simulation process is done into Ansys Fluent.

3.4.1 2D CFD Validation and Analysis

The discretization of the flow domain is the key point in CFD simulation. The quality of the mesh do affect the accuracy of results. The domain must contain enough cells and must be large enough to avoid the effects of far field boundary. A mesh independence test was performed over three mesh resolutions prior to conducting the CFD simulations. Thus, three types of mesh, from coarse to dense, were generated to ensure that the simulation results were sufficiently mesh-independent. Different mesh topologies have appeared in the literature such as "O mesh" and "C mesh". The topology used here is "C mesh". A structured quadrilateral mesh in ICEM CFD is applied to the model. The airfoil is situated in the domain with 19C from the inlet and 35C from the outlet as shown in Figure 3.21.

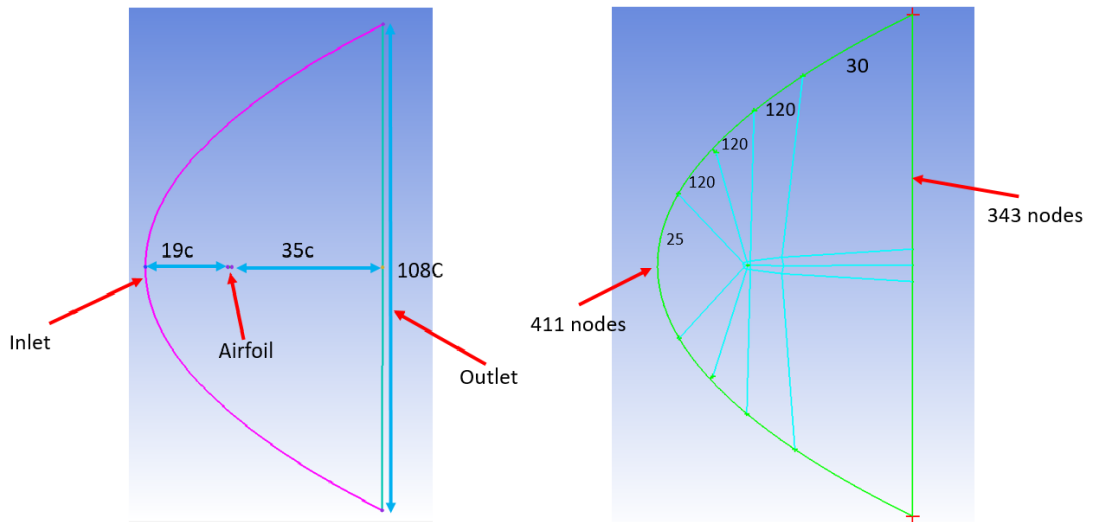


Figure 3.21: Domain Size and Block Strategy in ICEM CFD.

In terms of accuracy and computational cost, A structured quadrilateral mesh is more efficient than tetrahedral unstructured mesh. Figure 3.22 shows the mesh for the entire domain and near the airfoil with and without flap.

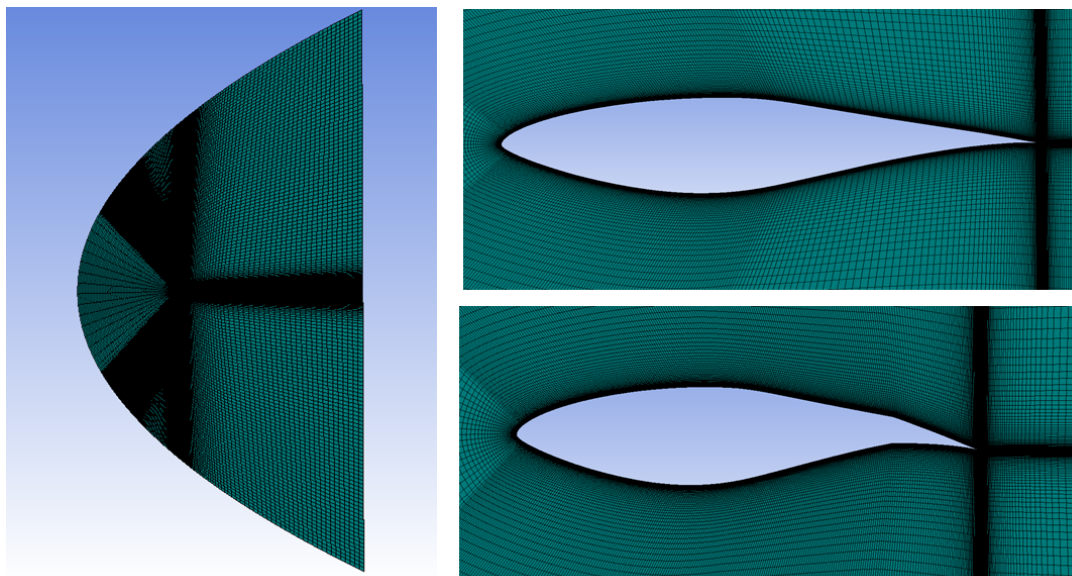


Figure 3.22: Mesh around the Airfoil with and without Flap.

In 2D airfoil simulation, the RANS approach has been commonly used. In wind turbine applications, the flow is assumed incompressible since the Mach number (Ma) is below 0.3. As a result, the flow rate has no effect on the temperature or density of the air. To model the flow field around an airfoil, several turbulence models have been developed. The analysis of transition phenomenon requires an appropriate approach. Most aerodynamic applications use the SST $k - \omega$ model, which is a two-equation eddy-viscosity model. It is a hybrid model that combines both the $k - \omega$ and $k - \epsilon$ models. The Transition SST turbulence model, a correlation-based model, is one of the most current approaches to modelling transition phenomena established in recent years. The Transition SST turbulence model, in contrast to previous transition model, finds the transition based on local flow conditions by using a transport equation [63]. In this study, SST $k - \omega$ model and transition SST model are used to determine the aerodynamic coefficients at zero AoA. The aerodynamic coefficients are then compared with the experimental results from TUDelft wind tunnel. The mesh independent study was done first for zero AoA, and then for the entire range of AoA, the mesh with the least error relative to experimental results was used. In Ansys Fluent, the turbulent intensity was set to 3.5% to simulate the wind tunnel inflow conditions. Tables 3.5 and 3.6 show the aerodynamic coefficients at zero AoA.

Table 3.5: Drag Coefficient at zero AoA and Re of 1×10^6 for S809 Airfoil.

Drag Coefficient at $AoA=0^\circ$, $Re = 1 \times 10^6$ for S809 Airfoil				
Mesh	Cells	SST $k - \omega$	Transition SST	TUDelft test
Coarse	29766	0.013420919	0.008125902	0.0094
Medium	52420	0.013902441	0.009306172	
Fine	136935	0.014039344	0.009439314	

Table 3.6: Lift Coefficient at zero AoA and Re of 1×10^6 for S809 Airfoil.

Lift Coefficient at $AoA=0^\circ$, $Re = 1 \times 10^6$ for S809 Airfoil				
Mesh	Cells	SST $k - \omega$	Transition SST	TUDelft test
Coarse	29766	0.11317252	0.14295974	0.139
Medium	52420	0.11401878	0.13405274	
Fine	136935	0.11422267	0.13382947	

From the tables above, its clear that the transition SST turbulence model with a fine mesh has better agreement with the wind tunnel results. Thus, the fine mesh with 136935 cells and the transition SST model are used for a complete range of AoA. Figures 3.23 and 3.24 show lift and drag coefficients comparison between CFD, XFOIL and experimental results for the airfoil S809 with and without flap.

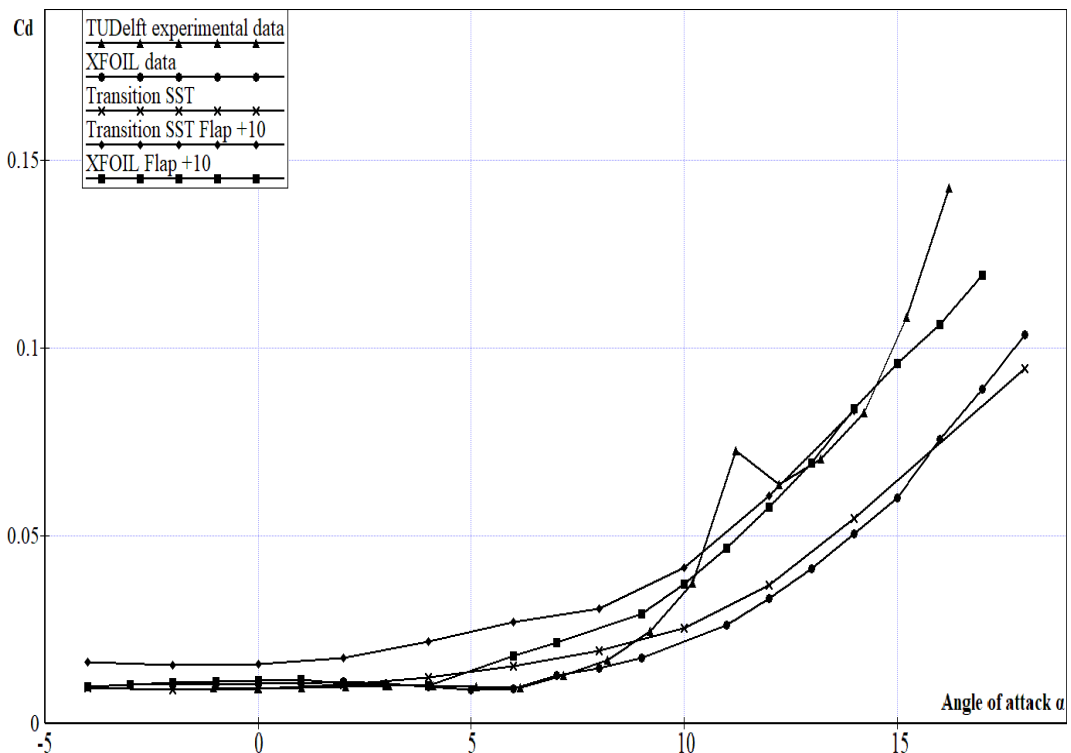


Figure 3.23: Drag Coefficient Comparison between CFD, XFOIL and Experimental Results for the Airfoil S809.

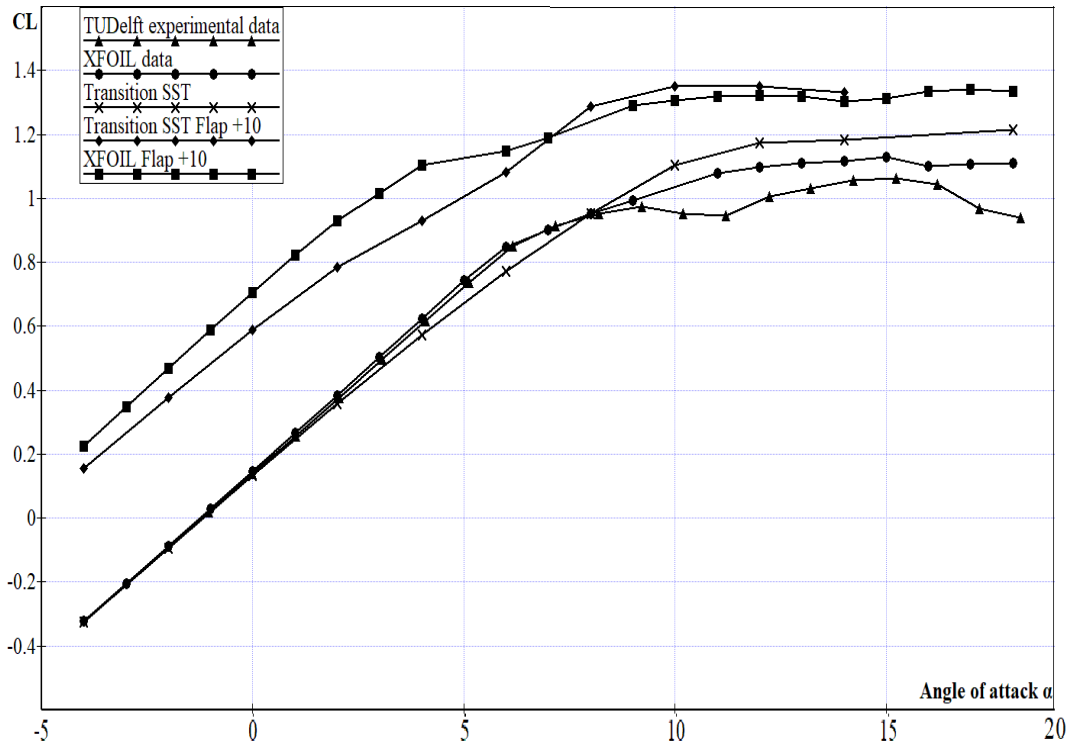
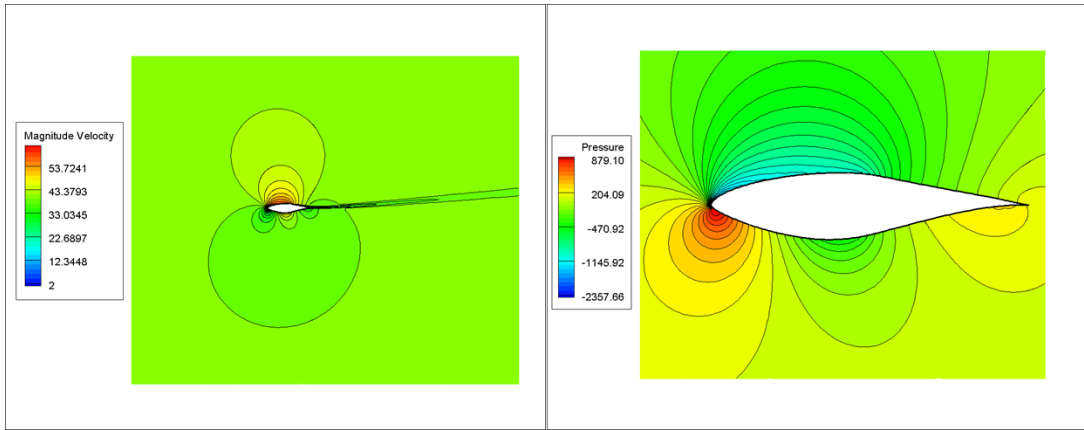
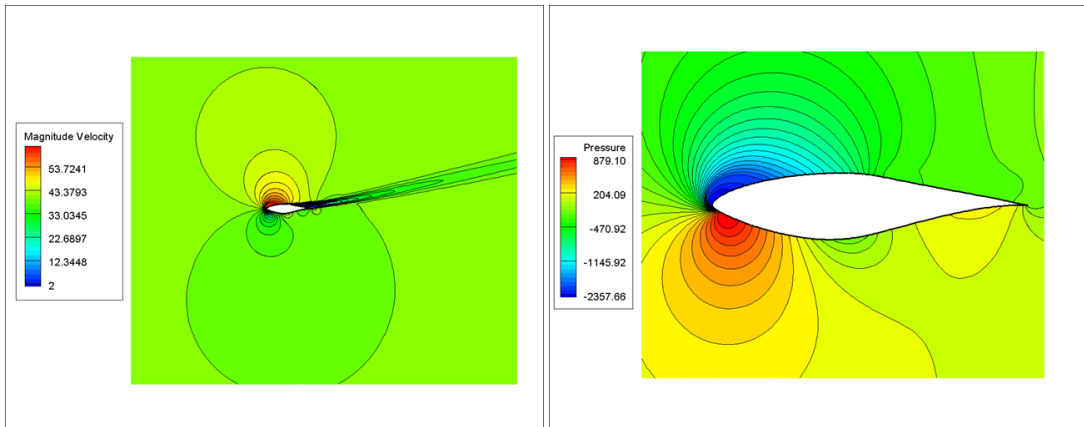


Figure 3.24: Lift Coefficient Comparison between CFD, XFOIL and Experimental Results for the Airfoil S809.

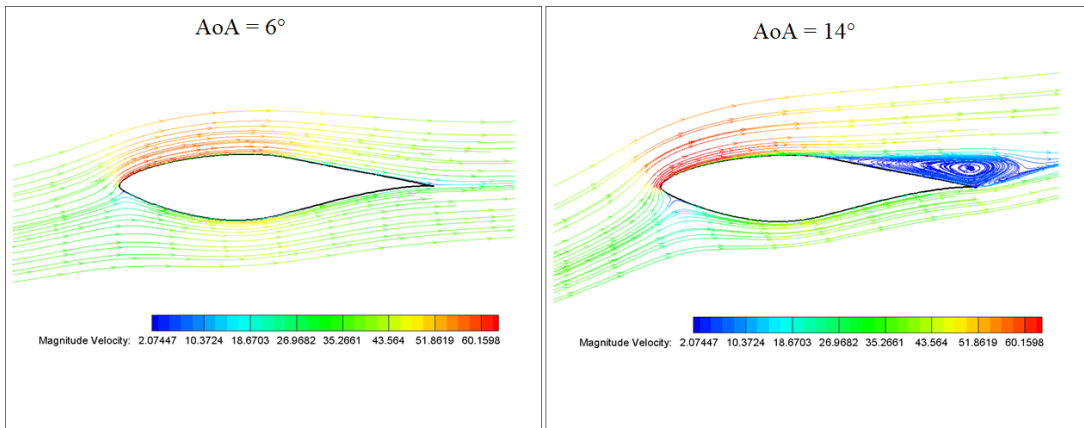
In the Figures above, the transition SST model shows better agreement with XFOIL. The XFOIL results and the CFD results are very similar to the wind tunnel results up to AoA of 7° . Both XFOIL and CFD under-predict the drag coefficient after the AoA which gives maximum lift to drag ratio, while Both XFOIL and CFD over-predict the lift coefficient after the same AoA. Figures 3.25 and 3.26 show the pressure and velocity contour and velocity streamlines for AoA of 6° and 14° for the airfoil S809.



(a) velocity and pressure contour for AoA of 6° .

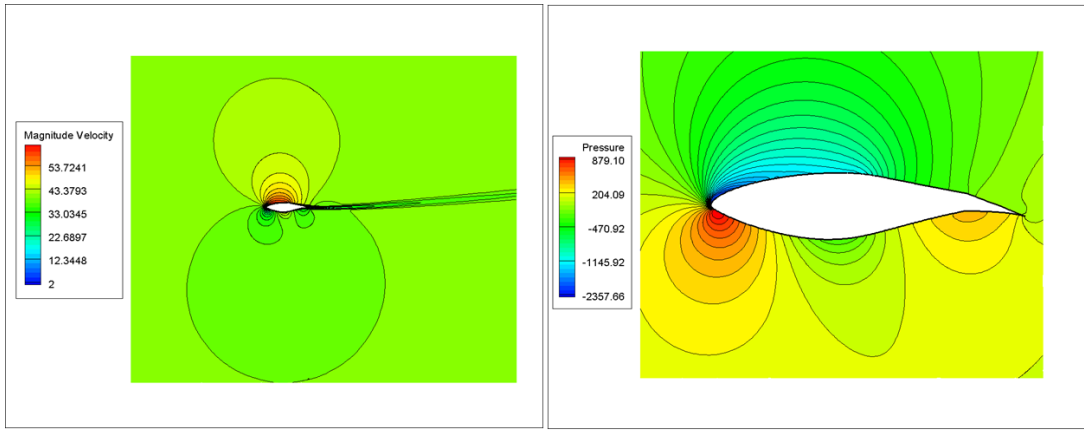


(b) velocity and pressure contour for AoA of 14° .

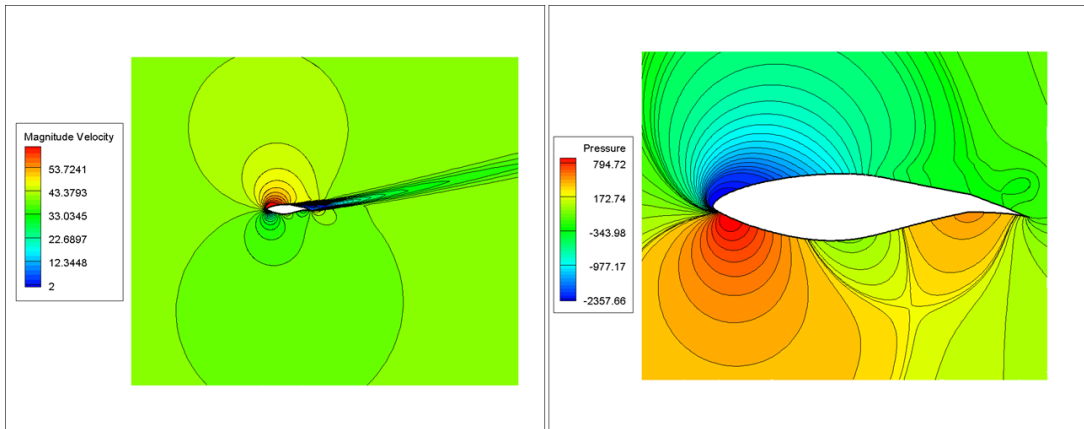


(c) velocity streamlines for AoA of 6° and 14° .

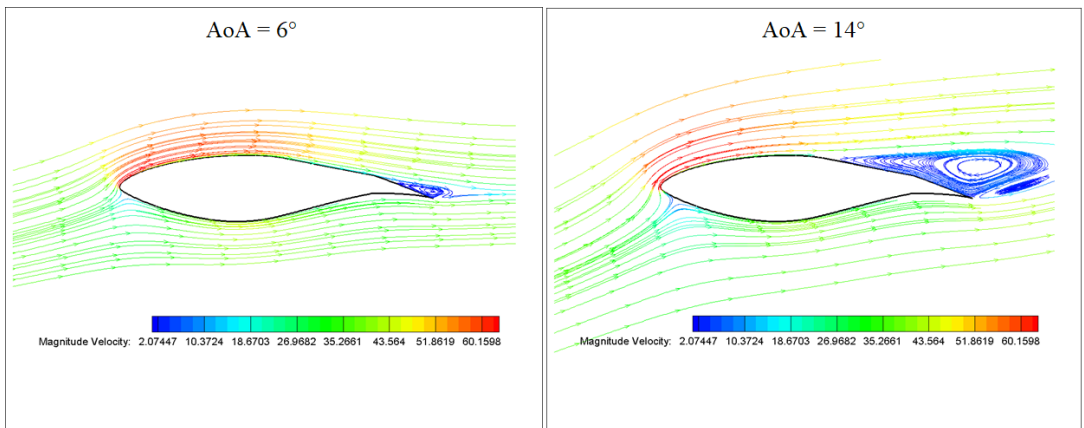
Figure 3.25: Pressure and Velocity Contour and Velocity Streamlines for AoA of 6° and 14° for Airfoil S809.



(a) velocity and pressure contour for AoA of 6° .



(b) velocity and pressure contour for AoA of 14° .

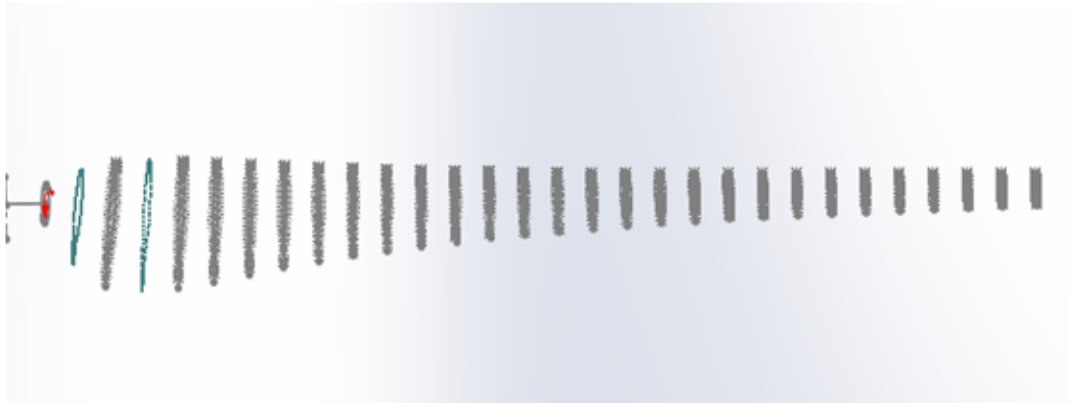


(c) velocity streamlines for AoA of 6° and 14° .

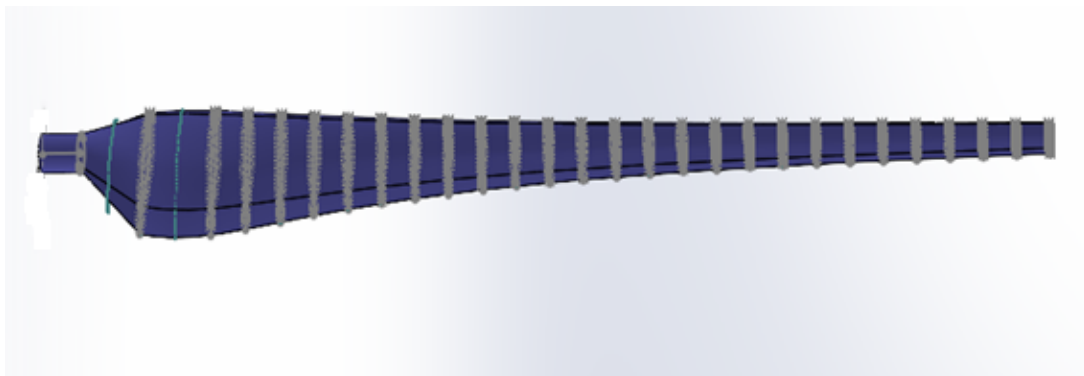
Figure 3.26: Pressure and Velocity Contour and Velocity Streamlines for AoA of 6° and 14° for Airfoil S809 with a Flap of 10° .

3.4.2 3D CFD Analysis: 2nd configuration

In this subsection, the 3D modelling of a FPVS stall-regulated wind turbine is discussed in details. The coordinates of the geometry is imported from QBlade software to SolidWorks as shown in Figure 3.27.



(a) Blade Coordinates from QBlade Software.



(b) Blade Geometry in SolidWorks Software .

Figure 3.27: The 2nd Configuration Coordinates and Geometry.

Only one blade is imported to CFD. the domain in CFD represents one-third of the full domain. The entire domain is split into two domains: Inner domain and outer domain. The domain outer radius is kept 30 m and the domain inner radius is 5.75 m. The inner domain is situated at 45 m from the velocity inlet and 100 m from the pressure outlet as shown in Figure 3.28.

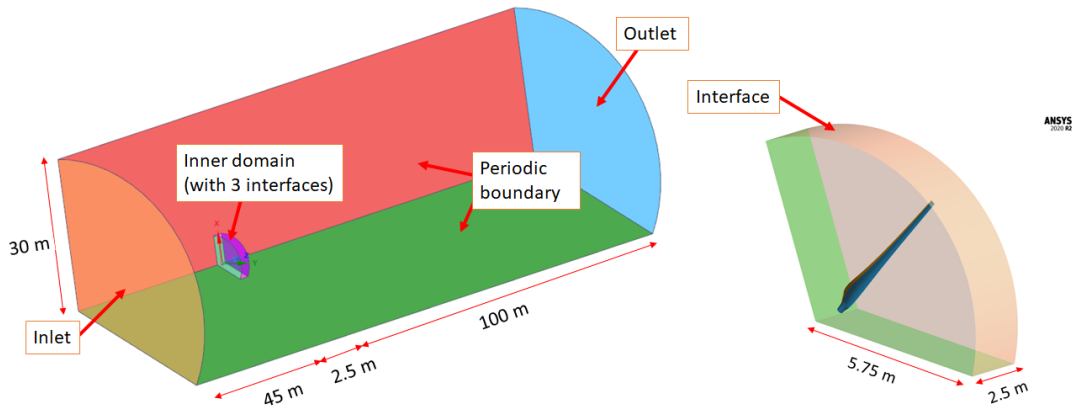


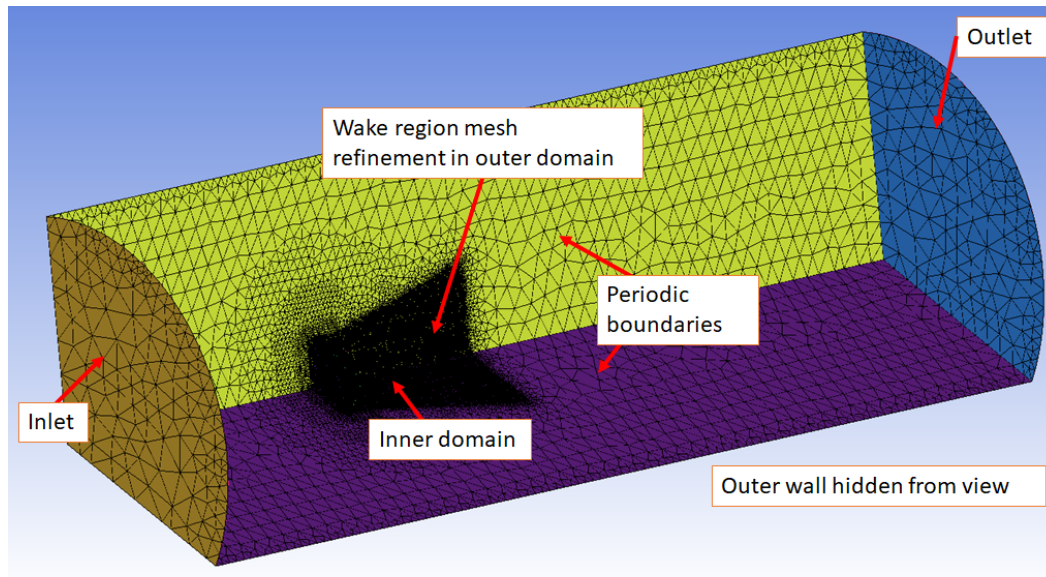
Figure 3.28: Domain Size and Boundary Conditions.

The mesh quality determines The accuracy of the results. In this work, the mesh is done in ICEM CFD. The density box is used to refine the cells at the blade and wake region. The effect of wind turbine hub is studied also. The wind shear effect and the tower effect are not discussed in this study. A 3D solid cylindrical hub with a length of 0.6m and a radius 0.2 m is shown in appendix C. The tetrahedral unstructured mesh is used. Mesh Independence study with different mesh sizes are applied. To capture the boundary layer properly, prism layers are used. the details of the meshes are presented in table 3.7.

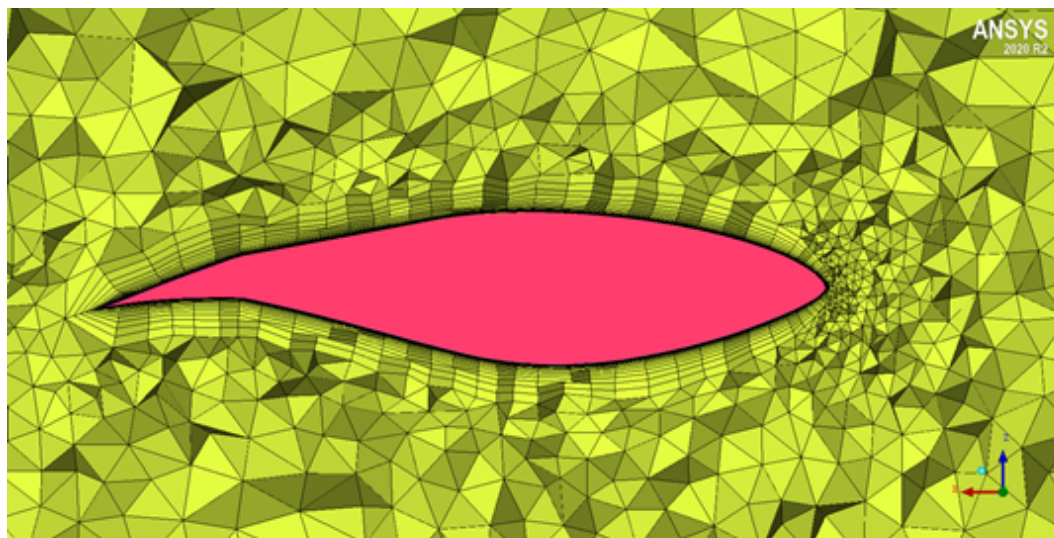
Table 3.7: A 3D Meshes for Wind Turbine with Different Sizes.

Mesh	Hub included	Prism layers	Cells
Mesh #1	No	7	5,670,860
Mesh #2	No	15	14,154,195
Mesh #3	Yes	5	6,780,947

From the table 3.7, the difference between mesh #1 and mesh #2 is the sizes and number of cells. In addition, mesh #2 contains more prism layers to capture boundary layer properly. To study the effect of the hub, mesh #3 contains a solid cylindrical hub. Figure 3.29 shows the unstructured mesh #2. More figures are included in appendix C.



(a) The Domain Unstructured Mesh.



(b) Inner View Showing the Prism Layers.

Figure 3.29: Unstructured Mesh #2 for the Wind Turbine.

For all cases, the Transition SST turbulent model is used. The results of the simulations and the comparison between both design configurations are presented in chapter 4.

Chapter 4

RESULTS

The design and performance analysis of small scale HAWT are discussed in two parts in this thesis. The first part of this study discussed the design and optimization of a FPVS stall-regulated HAWT using QBlade software. QBlade software is based on the Blade Element Momentum (BEM) algorithm. The pitch angle is fixed and the twist angle is optimized for stall. The power coefficient, power (torque), and annual yield are calculated by BEM method. The second part discussed the fixed trailing edge flap for wind turbine applications. This part is done by QBlade software and validated by the commercial CFD tool Ansys Fluent.

4.1 BEM Results and Analysis: 1st Configuration

The design of the 1st configuration is carried out in QBlade software only. The blade is discretized into 21 annular segments. The 3D correction, Prandtl tip loss, and Reynolds drag correction models are used in the BEM method. The BEM is an iterative process. The maximum of the difference of axial and tangential induction factor between the previous and the current iteration has to be below the convergence criterion ϵ . Thus, $\epsilon = 10^{-5}$ is used for convergence with 100 maximum number of iterations in the QBlade simulation. Once the blade has been designed for design conditions at specified design tip speed ratio, the performance of the rotor has to be determined. The results are shown as a graph of C_p versus the λ .

The curve shown in Figure 4.1 is very important for wind turbine. A wind turbine of three blades operates at tip speed ratio from $4 \leq \lambda \leq 10$. at low tip speed ratio, the

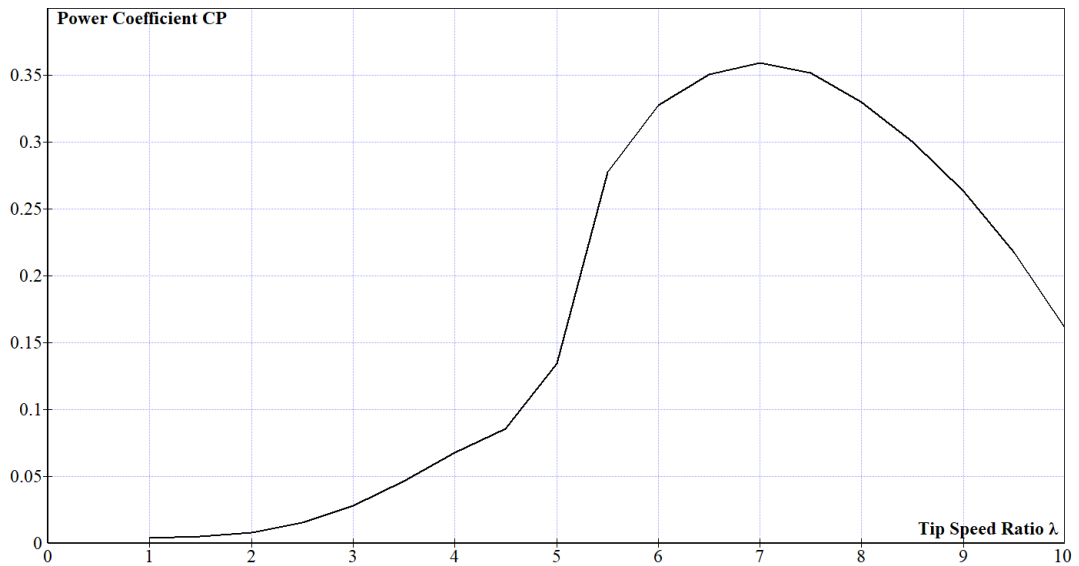


Figure 4.1: Power Coefficient versus Tip Speed Ratio.

rotor is not rotating and the power cannot be extracted from the wind. At high tip speed ratio, the blades run so fast with respect to wind velocity. Thus, the rotor acts as a blocked disk and the extracted power from the wind is very small. Maximum power is extracted from the wind at the design tip speed ratio. From the curve 4.1, the optimum power coefficient of 0.36 occurs at the design tip speed ratio of 7. Figure 4.2 shows the power extracted from the wind versus tip speed ratio.

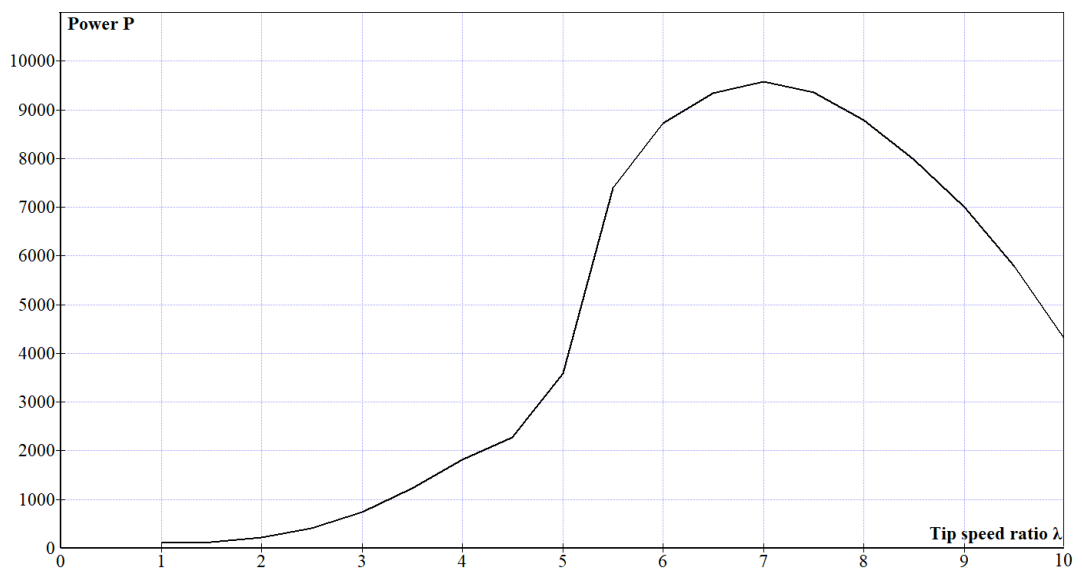


Figure 4.2: Power versus Tip Speed Ratio.

During the design process, the rated power must be taken into account. This wind turbine is designed for a rated power of 10 kW. At design tip speed ratio of 7, the power extracted from the wind is 9.7 kW with a power coefficient of 0.36. Small wind turbines are typically operate at relatively low wind speed. The manufacturers of the wind turbine determines the cut-in and cut-out speeds of the turbine to avoid the rotor damage. Based on the information from the manufacturers, the appropriate cut-in speed is in the range of (3-5) m/s. Figure 4.3 shows the power curve versus the wind speed from cut-in to cut-out.

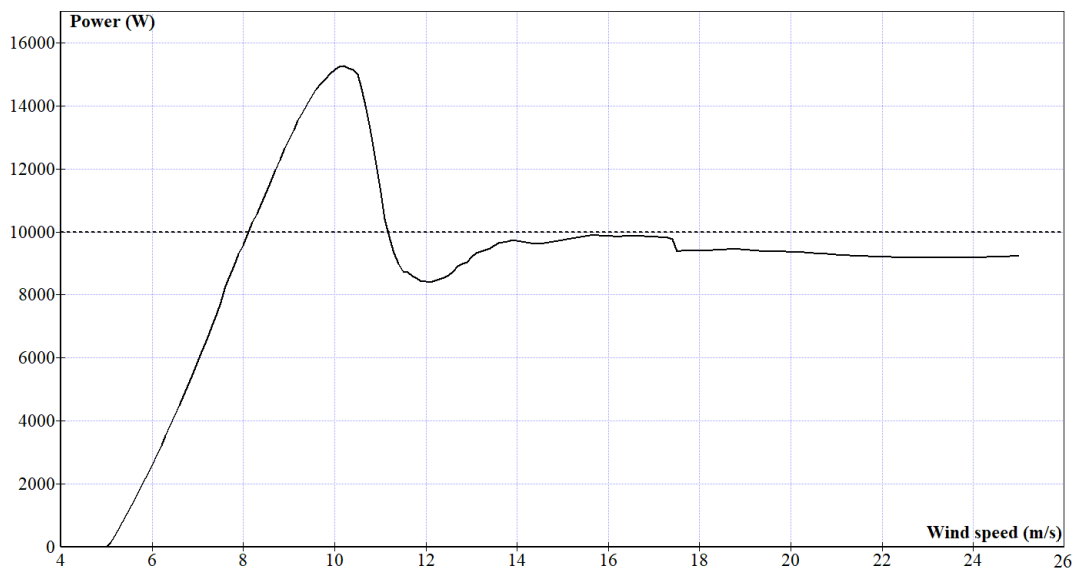


Figure 4.3: Power versus Wind Speed.

From the Figure 4.3, it is clearly apparent that the nature of the power curve is similar to the traditional stall-regulated wind turbine. The stall-regulated strategy relies on the rotor blades' aerodynamic design to limit the power output at high wind velocity. The rotational speed is kept constant and the angle of attack increases with wind speed. At higher angle of attack (higher velocity), the stall occurs. The aerodynamic torque and the power extracted decrease with increasing wind speed above a certain value. This value is usually not the same as the rated wind speed. Power in stall-regulated

turbines peaks at higher than rated wind speeds, then gradually decreases until the cut-out wind speed is reached. This is clearly shown in the Figure 3.4. At the rated wind speed of 8 m/s, the power extracted reaches the rated power of 10 kW, then the power continues in increasing until reaches the peak power at 10 m/s. After wind speed of 10 m/s, the power decreases then becomes approximately constant. The decrease in power with increasing wind speeds because regions of the blade are stalled and the separation occurs between the flow and the airfoil. The stall is unsteady phenomenon. Thus the forces on the blade cannot be predicted precisely. As a result the power output is fluctuated around the ideal rated power.

4.2 BEM Results and Analysis: 2nd Configuration

This part of the study discusses using the fixed trailing edge flap for wind turbine applications. The flap with a fixed inclined angle of 10° clockwise will be the point of focus of this study. The trailing edge flap used in this analysis is a sealed gap flap. The design and analysis of this blade configuration is done in QBlade software with the same optimization options. Figure 4.4 shows the power coefficient versus tip speed ratio for both design configurations.

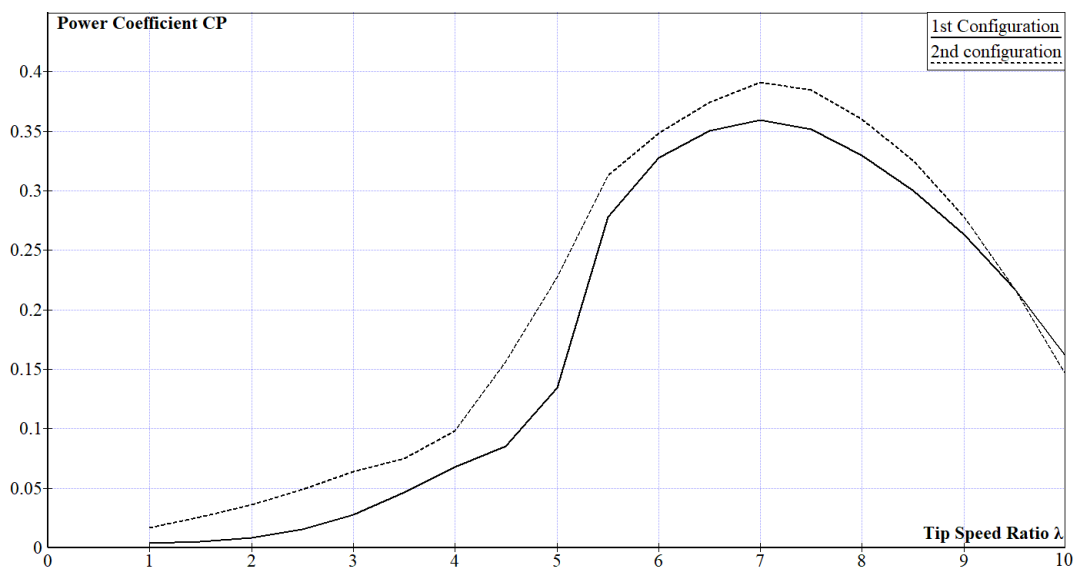


Figure 4.4: Power Coefficient versus Tip Speed Ratio for both Configurations.

From the Figure 4.4, the power coefficient has increased for the 2nd configuration. This is because the flap increases the aerodynamic lift and decreases the aerodynamic drag. This modifications in polar curves enhances the power coefficient and thus the power. At the design tip speed ratio of 7, the power coefficient in the 2nd design configuration is 8.3% higher than the 1st design configuration. In term of power, the power increases from 9.7 kW in the 1st configuration to 10.5 kW in the 2nd configuration at the design tip speed ratio of 7 as show in Figure 4.5.

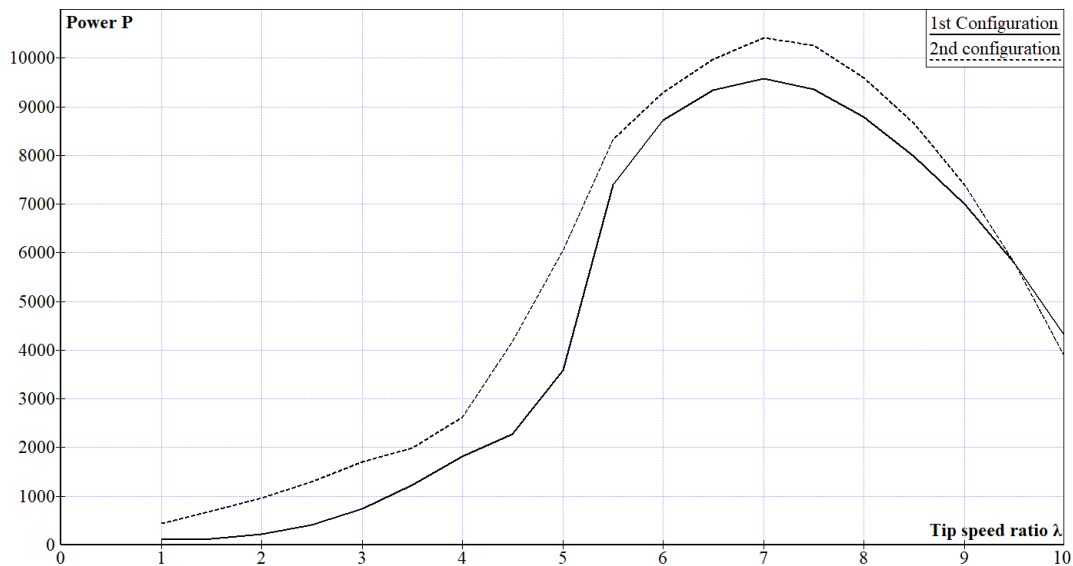


Figure 4.5: Power versus Tip Speed Ratio for both Design Configurations.

4.3 CFD Results and Validation: 2nd Configuration

The CFD method will be employed only for the 2nd configuration because of time limit. The mesh is done in ICEM CFD and the simulation process is carried into Ansys Fluent. For the three cases, the torque was calculated in transient mode with the transition SST model and converged with the residuals 1×10^{-5} . The torque, power and power coefficient at the design condition (tip speed ratio of 7 and wind speed 8 m/s) for the three meshes are presented in table 4.1.

Table 4.1: The Torque, Power and Power Coefficient at the Design Condition.

Mesh	Hub included	Torque (N.m)	Power (W)	Power coefficient
Mesh #1	No	365.13212	11,698.83	0.4391
Mesh #2	No	366.06473	11,728.71	0.4402
Mesh #3	Yes	359.81717	11,528.54	0.4327

From the table above, the case#1 and case#2 show acceptable agreement. Case #2 contains more than 14 millions cells which is more expensive and time consuming. Thus, it can be concluded that case #1 contains sufficient cells in the domain and the blade to solve the case with a good accuracy. In comparison with BEM results from QBlade software, The CFD method over-predicts the power and thus the power coefficient compared with the BEM method. The power coefficient from 3D CFD simulation is approximately 12% higher. BEM method depends on the 2D aerodynamic data to simulate the 3D flow and the corrections models must be implemented to give better results. It is noted that the 2D flow characterizations cannot be able to simulate the 3D flows, while the CFD method is a very detailed method and provide accurate results at stall. According to case #3, the a solid cylindrical hub has a negligible effect on the power and power coefficient. Thus, simulating the wind turbine without hub is much better and gives the user a full control without restrictions on the mesh refinement and adding more prism layers in the boundary layer. Figure 4.6 shows the power coefficient versus tip speed ratio. It important to consider that the CFD method has a weak area when applied away from the design conditions. The CFD method is more appropriate and gives high accurate results around the design point. This is clearly appears in the Figure 4.6.

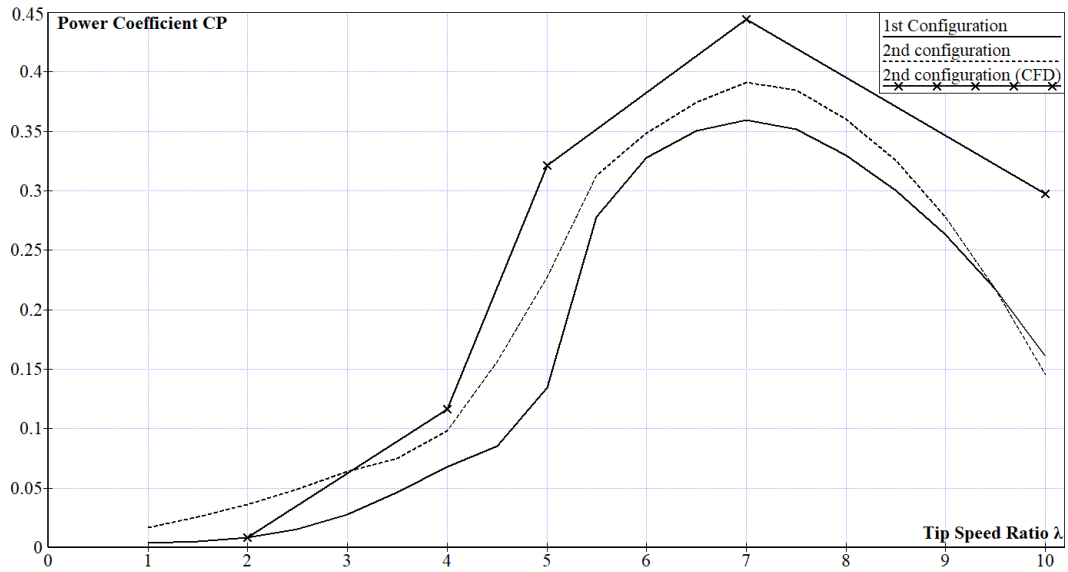


Figure 4.6: Power coefficient comparison for both Design Configurations.

At a fixed rotor RPM, CFD calculations are done to evaluate the power curve. The comparison between both configurations are shown in Figure 4.7.

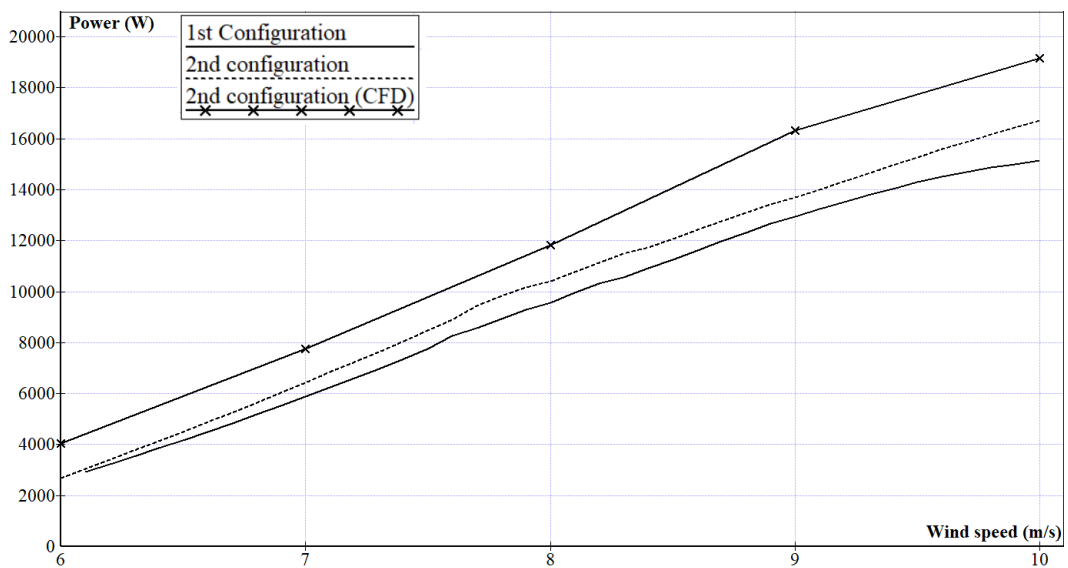


Figure 4.7: The Power Output for both Design Configurations.

The 3D CFD computed power curve follows the same trend as the BEM curves. When compared to the QBlade software, the CFD approach over-predicts the power. The CFD technique is significantly more expensive and more time consuming. The BEM is an iterative method which can provide accurate results with a short time. Figure 4.8

and 4.9 show the velocity streamlines plot.

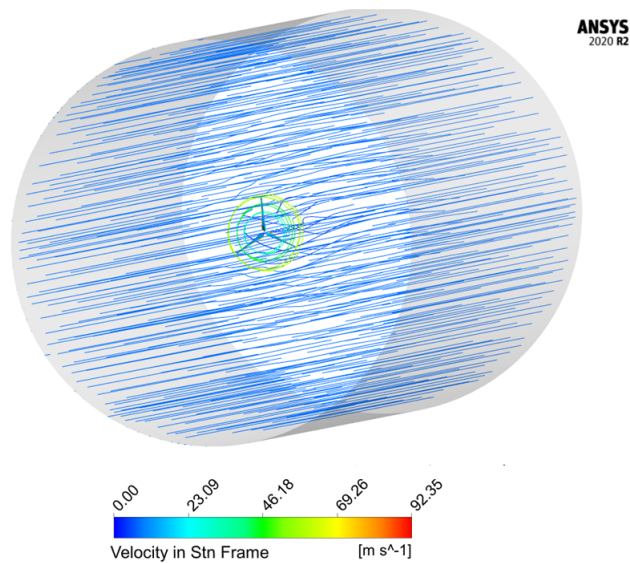


Figure 4.8: The Velocity Streamlines in a Stationary Frame of Reference.

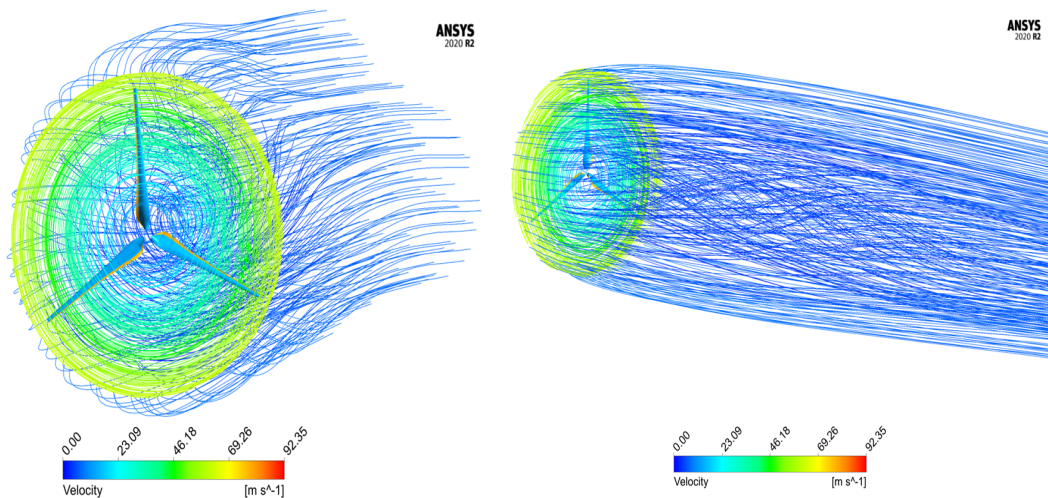


Figure 4.9: The Velocity Streamlines Plot.

The Figure 4.8 fulfills the actuator disk theory. The velocity decreased behind the rotor as expected from the mass and momentum balance. It is worth noting that the speed of the blade increases from the root to the tip. As compared to the streamlines of the fluid domain, the wake formation is obvious, which lead to energy losses. The more wake generation, the more energy is lost. The downstream is chaotic especially at the center

of the flow. Figure 4.10 shows the blades velocity vector with respect to a stationary frame of reference.

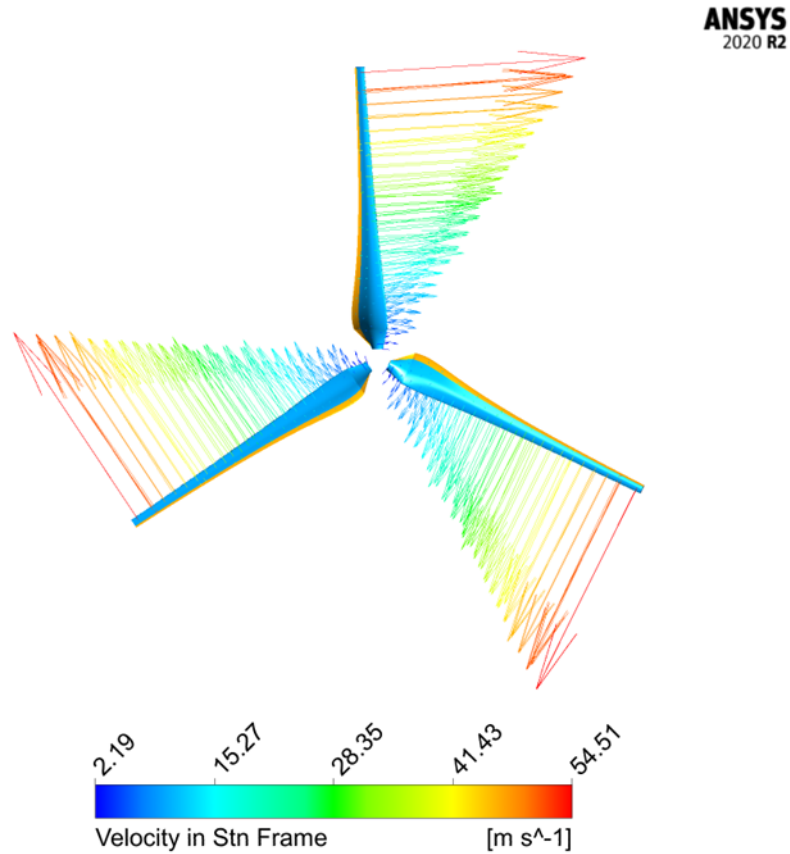
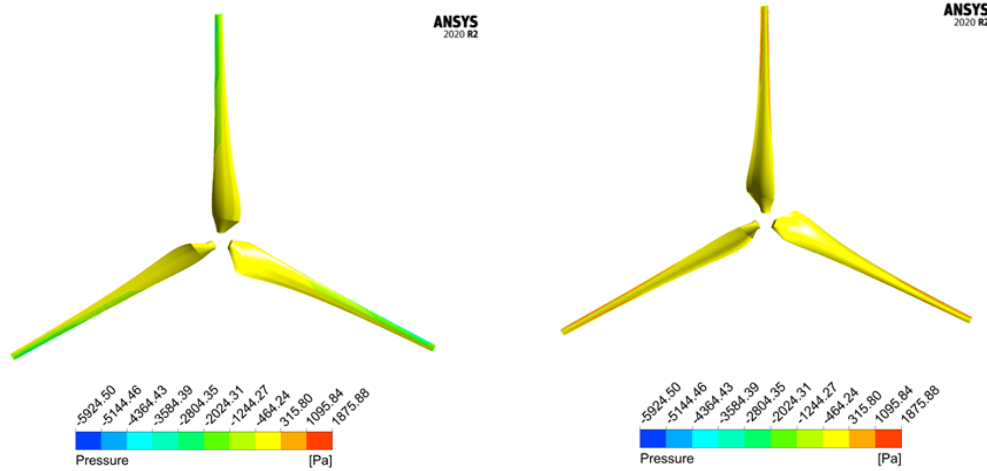


Figure 4.10: Velocity Vector in Standard Frame of Reference.

It's obvious that the blade velocity rises as the local radius of the blade increases. The blade tip has the highest velocity, while the blade root has the lowest velocity. Figure 4.11 shows the pressure distribution on the surface of the blade. As expected, there is pressure difference between the upward and downward surface. This is clearly appears at the blade tip , the pressure difference is significant due to a high tip speed. The blade root has a small pressure difference compared with the blade tip.



(a) Upward Side of the blade

(b) Downward Side of the blade

Figure 4.11: Pressure Distribution on the Surface of the Blade

Figure 4.12 shows the Y+ distribution on the surface of the blade. The value of Y+ on the blade surface is preferred to be around 1. Figure 4.13 presents the velocity vectors and pressure contours of different sections of the blade at the design conditions. At the design wind speed of 8 m/s, the flow is attached and the separation occurs at the flap.

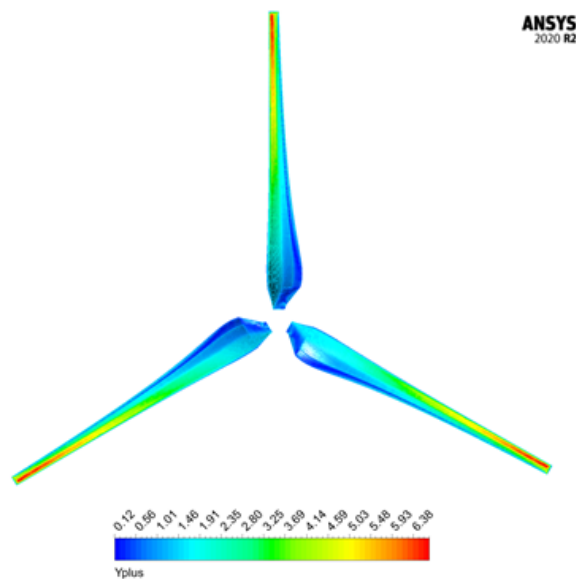
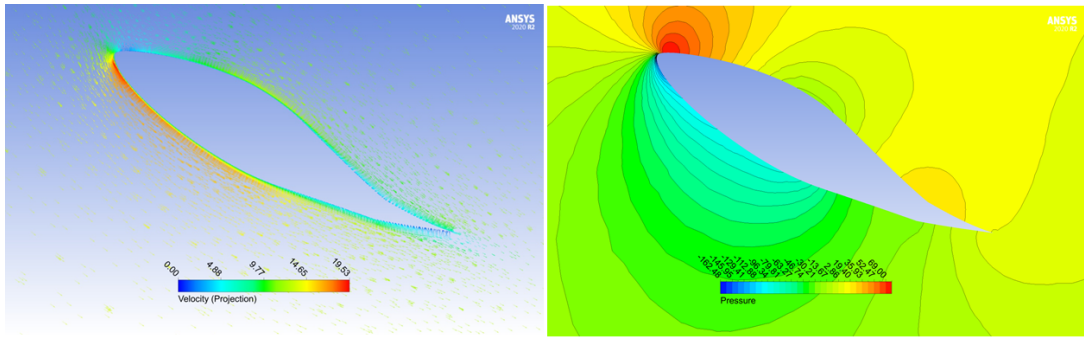
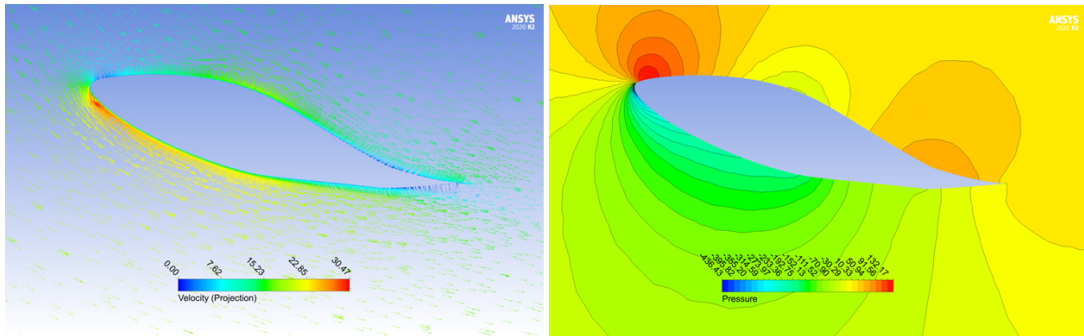


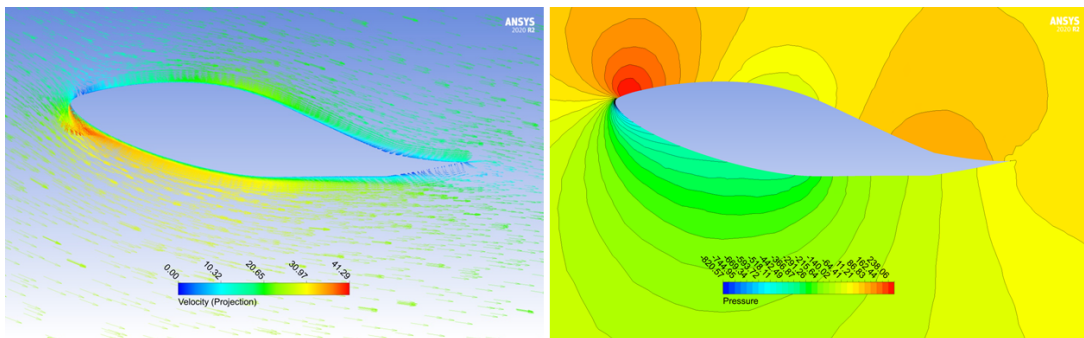
Figure 4.12: Y+ Distribution on the Surface of the Blade.



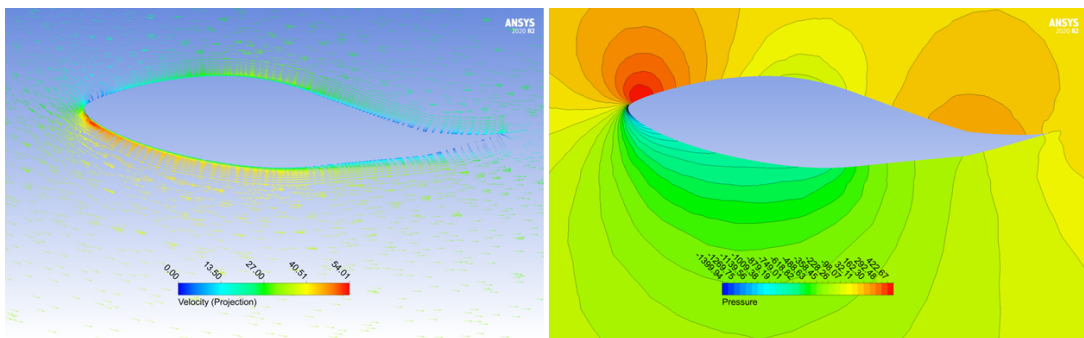
(a) 0.15R of the Span.



(b) 0.25R of the Span.

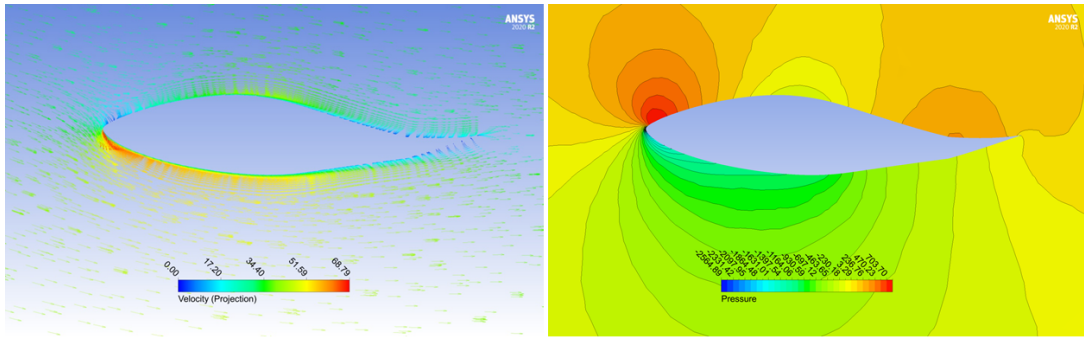


(c) 0.37R of the Span.

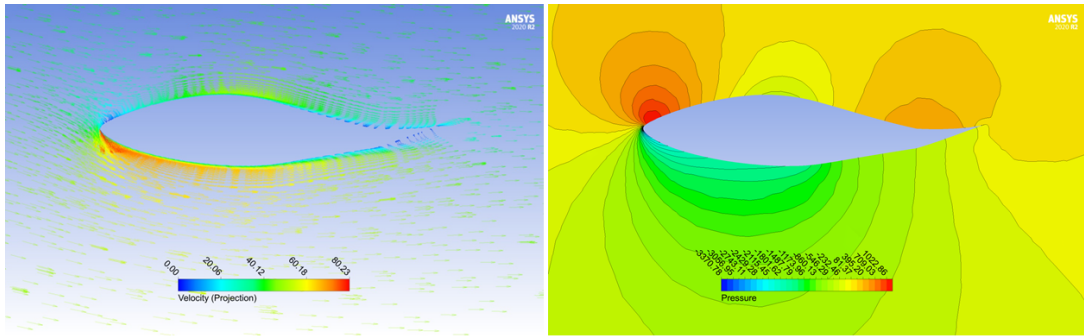


(d) 0.5R of the Span.

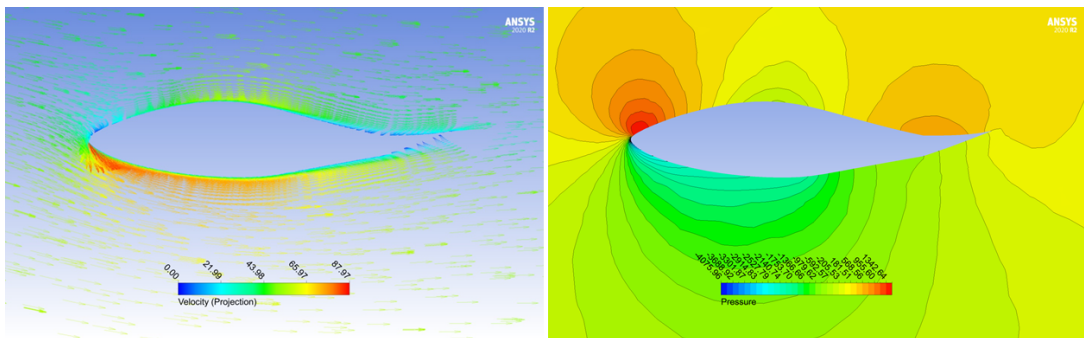
Figure 4.13: The Velocity Vectors and Pressure Contours of Different Sections of the Blade at the Design Conditions .



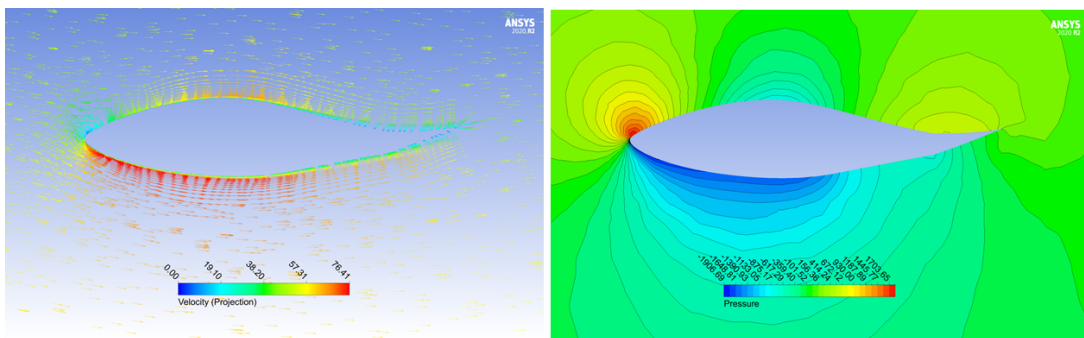
(e) 0.65R of the Span.



(f) 0.79R of the Span.



(g) 0.9R of the Span.



(h) Blade Tip Location.

Figure 4.13: The Velocity Vectors and Pressure Contours of Different Sections of the Blade at the Design Conditions.

4.4 Annual Yield Results

Once a turbine simulation has been performed, the annual yield of the turbine can be calculated by setting an annual wind speed distribution using the WEIBULL distribution's parameters k and A . INCEK region-ANKARA with Latitude of 39.828540 and Longitude of 32.736850 is considered as a case study with a specific wind speed data. The values of WEIBULL parameters k and A are determined as 1.4743 and 3.303 respectively (Please see: Section 3.3). The mean wind speed is calculated at height of 20 m as 2.9859 m/s. By using both design configurations with predetermined design parameters, annual energy production (AEP) can be estimated. Thanks to QBlade software, annual energy output for the proposed design is automatically estimated by setting the k and A values for the WEIBULL distribution. Table 4.2 presents the annual yield for both design configuration.

Table 4.2: Annual Yield for both Design Configurations.

Configuration	C_P (QBlade value)	annual yield ($\frac{kWh}{year}$)
1st configuration	0.36	6378
2nd configuration	0.39	6944

Its clear from the table that the 2nd configuration (blade with flap deflected angle of 10°) has better annual yield than the 1st configuration. The improvement of aerodynamic coefficients (increasing C_L and decreasing C_D by using a trailing edge flap) has a direct impact on the annual yield generated by wind turbines.

Chapter 5

CONCLUSIONS

5.1 Findings and Conclusions

Recently, wind turbines were developed with the lowest energy cost. The Levelized Cost Of Energy (LCOE) must be kept as low as possible during the design process. All turbine components are designed using a multidisciplinary approach. A turbine blade is a critical part of this system since it rotates and is subjected to cyclic and aerodynamic loads.

This thesis discussed the design and performance of small scale HAWT with different blade configurations. A trailing edge flap is used in the 2nd configuration and compared with the 1st configuration. The rotor performance is found by using two methods, BEM and CFD. QBlade is a software based on BEM approaches which allow the user to design different geometries in short time. The classical BEM approach is very cost efficient and the computational time is significantly less than other methods. As a result, only design and assessment tools based on the BEM technique are utilised in the industry to estimate the efficiency of HAWT. Other approaches, such as CFD, RANS, and vortex models, are thus limited to research environments. The BEM model, which is actually a two-dimensional technique extrapolated into the third dimension, accounts for three dimensions using semi-empirical correction models obtained from correlations with observations or complete CFD calculations. The conclusions are described below:

- The main advantage of stall controlled wind turbine is that it eliminates the

need for moving parts in the rotor and a complicated control mechanism. Stall control wind turbine is a complicated aerodynamic design task with corresponding design problems in the structural dynamics of the entire wind turbine. The blades of a stall-regulated wind turbine, are built so that when wind speeds are high, the aerodynamic torque, and hence the power output, drops when wind speeds exceed a specific value (this value of wind speed is higher than rated wind speed). That is, The rotor is designed to perform worse (in terms of energy extraction) to safeguard the wind turbine without using active pitch mechanism.

- The 3D effects cannot be accounted for by the BEM approach due to its 2D nature. This results in significant difference between the computed and measured turbine data, especially when stall is present. As a result, semi empirical correction models are used in the BEM method to consider these effects. On the other hand, The wind turbine CFD simulation requires no empirical corrections models compared with the BEM method. The CFD simulation can also be used to validate existing correction models and development of new models.
- The classical BEM technique produces accurate results, is highly cost-efficient, and takes much less computational time than the CFD method. On the other hand, CFD is more accurate and provides a complete flow characterization, but it is also a high-cost method in term of time consuming.
- The solid cylindrical hub profile has a negligible effect on the efficiency of HAWT. Thus, a 3D CFD simulation of blade without hub is more convenient and decrease the number of cells and computational time without any significant changes in results.
- A sealed gap flap with a fixed clockwise Angle can be used for wind turbine

applications. the flap is accounted for the modified lift and drag coefficient table. Thus, a higher efficiency is resulted. In this case, the designer may face problems in controlling the output power, especially at high wind speed (the blade have to be designed to perform worse at high wind speed). Trial and error is a method to deal with this problem in which several attempts are made to reach a desired output (stall at high wind speed).

- The improvement of aerodynamic coefficients (increasing the lift coefficient and decreasing the drag coefficient by using a trailing edge flap) has a direct impact on the annual yield generated by wind turbines.

5.2 Future Works

the further works are recommended to be attempted in future works:

- In this study the rotor blades and hub are only included. The other major parts of HAWT such as tower, nacelle and yaw control can be added to the study for a complete model analysis. These parts have major effects on the overall efficiency of HAWT.
- This study applies a single airfoil for the blade design. Blade profile can be changed by applying a mixed airfoils along the blade length, which will change the performance of HAWT also.
- Different flap angles can be inspected from -15° to 15° to choose an angle which provides high power output and annual yield.

REFERENCES

- [1] R. Lindsey, “Climate change: Global sea level,” 2021. [Online]. Available: <https://www.climate.gov/news-features/understanding-climate/climate-change-global-sea-level>.
- [2] “U.s. energy information administration (EIA),” 2019. [Online]. Available: <https://www.eia.gov/international/data/world>.
- [3] Enerdata, “global energy statistical yearbook,” 2020. [Online]. Available: <https://yearbook.enerdata.net/renewables/renewable-in-electricity-production-share.html>.
- [4] R. W. Righter, *Wind energy in America: A history*. University of Oklahoma Press., 1996.
- [5] B. Woodcraft, “The pneumatics of hero of alexandria, london, taylor walton and maberly,” *This is a translation and compilation from the ancient Greek of the work of Hero (10 AD-70 AD)*., 1851.
- [6] J. F. Manwell, J. G. McGowan, and A. L. Rogers, *Wind energy explained: theory, design and application*. John Wiley & Sons, 2010.
- [7] D. Wood, “Smeaton’s law?” *Wind Engineering*, vol. 23, no. 6, pp. 373–375, 1999. [Online]. Available: <http://www.jstor.org/stable/43749907>

- [8] J. Smeaton, “Xviii. an experimental enquiry concerning the natural powers of water and wind to turn mills, and other machines, depending on a circular motion.” *Philosophical transactions of the Royal society of London*, no. 51, pp. 100–174, 1759.
- [9] M. Pasqualetti, R. Richter, and P. Gipe, *History of Wind Energy*, 01 2004, pp. 419–433.
- [10] P. Putnam, “Power from the wind, vannostrand company,” *Inc. New York*, 1948.
- [11] L. Martin, “Wind energy—the facts: A guide to the technology, economics and future of wind power,” 2010.
- [12] “Rüzgar enerji santralleri (in turkish),” 2017. [Online]. Available: <https://www.enerjiatlası.com/ruzgar/>
- [13] “Turkish wind energy association,” 2021. [Online]. Available: <http://www.tureb.com.tr/>
- [14] I. E. Agency, “World energy balances,” 2020. [Online]. Available: <https://www.oecd-ilibrary.org/content/data/be0c09b9-en>
- [15] P. Clausen and D. Wood, “Research and development issues for small wind turbines,” *Renewable Energy*, vol. 16, no. 1-4, pp. 922–927, 1999.

- [16] A. Das, K. B. Chimonyo, T. R. Kumar, S. Gourishankar, and C. Rani, "Vertical axis and horizontal axis wind turbine- a comprehensive review," in *2017 International Conference on Energy, Communication, Data Analytics and Soft Computing (ICECDS)*, 2017, pp. 2660–2669.
- [17] A. A. Alsultan, "Computational and experimental study on innovative horizontal-axis wind turbine blade designs," 2015.
- [18] H. Glauert, "Airplane propellers," in *Aerodynamic theory*. Springer, 1935, pp. 169–360.
- [19] M. O. Hansen, *Aerodynamics of wind turbines*. Routledge, 2015.
- [20] E. Benini and A. Toffolo, "Optimal design of horizontal-axis wind turbines using blade-element theory and evolutionary computation," *J. Sol. Energy Eng.*, vol. 124, no. 4, pp. 357–363, 2002.
- [21] M. Ozair, S. Sarfaraz, M. Hussain, and M. Qureshi, "Aerodynamic design and analysis of horizontal axis wind turbine," 12 2011.
- [22] A. J. Rosenberg, "A computational analysis of wind turbine and wind farm aerodynamics with a focus on dual rotor wind turbines," 2016.
- [23] Y. Kim, "Computational airfoil optimization for the improvement of the performance of horizontal axis wind turbines (hawt) with a 3d model," 2020.

- [24] L. Cantoni, “Load control aerodynamics in offshore wind turbines,” 2021.
- [25] X. Tang, “Aerodynamic design and analysis of small horizontal axis wind turbine blades,” Ph.D. dissertation, University of Central Lancashire, 2012.
- [26] B. Montgomerie, “Methods for root effects, tip effects and extending the angle of attack range to $\{\pm\}$ 180 deg., with application to aerodynamics for blades on wind turbines and propellers,” 2004.
- [27] H. Himmelskamp, “Profile investigations on a rotating airscrew.”
- [28] R. Mikkelsen *et al.*, “Actuator disc methods applied to wind turbines,” Ph.D. dissertation, PhD thesis, Technical University of Denmark, 2003.
- [29] L. A. Viterna and R. D. Corrigan, “Fixed pitch rotor performance of large horizontal axis wind turbines,” in *NASA Lewis Research Center: Energy Production and Conversion Workshop, Cleveland, OH, United States January*, vol. 1, 1982.
- [30] W. Z. Shen, R. Mikkelsen, J. N. Sørensen, and C. Bak, “Tip loss corrections for wind turbine computations,” *Wind Energy: An International Journal for Progress and Applications in Wind Power Conversion Technology*, vol. 8, no. 4, pp. 457–475, 2005.
- [31] H. Snel, R. Houwink, J. Bosschers, W. Piers, G. J. Van Bussel, and A. Bruining, “Sectional prediction of sd effects for stalled flow on rotating blades and

comparison with measurements,” 1993.

- [32] J. Hernandez and A. Crespo, “Aerodynamic calculation of the performance of horizontal axis wind turbines and comparison with experimental results,” *Wind Engineering*, pp. 177–187, 1987.
- [33] B. Sanderse, S. Van der Pijl, and B. Koren, “Review of computational fluid dynamics for wind turbine wake aerodynamics,” *Wind energy*, vol. 14, no. 7, pp. 799–819, 2011.
- [34] L. A. M. Tossas and S. Leonardi, “Wind turbine modeling for computational fluid dynamics: December 2010-december 2012,” National Renewable Energy Lab.(NREL), Golden, CO (United States), Tech. Rep., 2013.
- [35] F. R. Menter, “Two-equation eddy-viscosity turbulence models for engineering applications,” *AIAA journal*, vol. 32, no. 8, pp. 1598–1605, 1994.
- [36] H. K. Versteeg and W. Malalasekera, *An introduction to computational fluid dynamics: the finite volume method*. Pearson education, 2007.
- [37] M. M. Hasan, “Design and performance analysis of small scale horizontal axis wind turbine for nano grid application,” 2017.
- [38] M. R. Islam, L. Bin Bashar, and N. S. Rafi, “Design and simulation of a small wind turbine blade with qblade and validation with matlab,” in 2019

4th International Conference on Electrical Information and Communication Technology (EICT), 2019, pp. 1–6.

- [39] M. Refan and H. Hangan, “Aerodynamic performance of a small horizontal axis wind turbine,” *Journal of Solar Energy Engineering-transactions of The Asme*, vol. 134, p. 021013, 2012.
- [40] N. Tobin, A. Hamed, and L. Chamorro, “An experimental study on the effects of winglets on the wake and performance of a model wind turbine,” *Energies*, vol. 8, pp. 11 955–11 972, 10 2015.
- [41] M. Ozair, S. Sarfaraz, M. Hussain, and M. Qureshi, “Aerodynamic design and analysis of horizontal axis wind turbine,” 12 2011.
- [42] N. Trolborg, “Computational study of the risø-b1-18 airfoil equipped with actively controlled trailing edge flaps,” *Technical University of Denmark*, 2004.
- [43] J. Sloof, W. de Wolf, H. van der Wal, and J. Maseland, “Aerodynamic and aero-acoustic effects of flap tip fences,” in *40th AIAA Aerospace Sciences Meeting & Exhibit*, 2002, p. 848.
- [44] “Flying turtle company.” [Online]. Available: <http://www.ftexploring.com>
- [45] J. Ma, Y. Duan, M. Zhao, W. Lv, J. Wang, Q. Meng Ke, and Y. Ren, “Effect of airfoil concavity on wind turbine blade performances,” *Shock and Vibration*, vol. 2019, 2019.

- [46] V. V. Agrawal, “Design and aero-acoustic analysis of a counter-rotating wind turbine,” Ph.D. dissertation, Purdue University, 2010.
- [47] W. Timmer and R. Van Rooij, “Summary of the delft university wind turbine dedicated airfoils,” *J. Sol. Energy Eng.*, vol. 125, no. 4, pp. 488–496, 2003.
- [48] J. L. Tangler and D. M. Somers, “Nrel airfoil families for hawts,” National Renewable Energy Lab., Golden, CO (United States), Tech. Rep., 1995.
- [49] M. Drela, “Xfoil: An analysis and design system for low reynolds number airfoils,” in *Low Reynolds number aerodynamics*. Springer, 1989, pp. 1–12.
- [50] S. J. Miley, “Catalog of low-reynolds-number airfoil data for wind-turbine applications,” Rockwell International Corp., Golden, CO (USA). Rocky Flats Plant; Texas A . . . , Tech. Rep., 1982.
- [51] R. E. Wilson, P. B. Lissaman, and S. N. Walker, “Aerodynamic performance of wind turbines. final report,” Oregon State Univ., Corvallis (USA). Dept. of Mechanical Engineering, Tech. Rep., 1976.
- [52] M. Yurdusev, R. Ata, and N. Çetin, “Assessment of optimum tip speed ratio in wind turbines using artificial neural networks,” *Energy*, vol. 31, no. 12, pp. 2153–2161, 2006.
- [53] R. Gasch, J. Twele, and G. Windkraftanlagen, “Entwurf, planung und betrieb,” 2007.

- [54] D. Marten, J. Wendler, G. Pechlivanoglou, C. N. Nayeri, and C. Paschereit, “Qblade: an open source tool for design and simulation of horizontal and vertical axis wind turbines,” *Int. J. Emerging Technol. Adv. Eng.*, vol. 3, no. 3, pp. 264–269, 2013.
- [55] S. Miller, P. Migliore, and G. Quandt, “An evaluation of several wind turbine trailing-edge aerodynamic brakes,” 1996.
- [56] S. Miller, “Experimental investigation of aerodynamic devices for wind turbine rotational speed control: Phase ii,” National Renewable Energy Lab., Golden, CO (United States), Tech. Rep., 1996.
- [57] S. Jain, N. Sitaram, and S. Krishnaswamy, “Computational investigations on the effects of gurney flap on airfoil aerodynamics,” *International scholarly research notices*, vol. 2015, 2015.
- [58] S. Salcedo, F. Monge, F. Palacios, F. Gandía, A. Rodriguez, and M. Barcala, “Gurney flaps and trailing edge devices for wind turbines,” *Proc. of EWEC 2006*, 2006.
- [59] J. Alber, R. Soto-Valle, M. Manolesos, S. Bartholomay, C. N. Nayeri, M. Schönlaue, C. Menzel, C. O. Paschereit, J. Twele, and J. Fortmann, “Aerodynamic effects of gurney flaps on the rotor blades of a research wind turbine,” *Wind Energy Science*, vol. 5, no. 4, pp. 1645–1662, 2020.

- [60] S. J. Johnson and D. E. Berg, "Active load control techniques for wind turbines," 2008.
- [61] D. Marten and J. Wendler, "Qblade guidelines," *Ver. 0.6, Technical University of (TU Berlin), Berlin, Germany*, 2013.
- [62] L. Bilir, M. İmir, Y. Devrim, and A. Albostan, "Determination of weibull parameters for wind speed distribution at incekk region–ankara," *Int. J. Hyrdogen Energ*, 2014.
- [63] K. Rogowski, G. Królak, and G. Bangga, "Numerical study on the aerodynamic characteristics of the naca 0018 airfoil at low reynolds number for darrieus wind turbines using the transition sst model," *Processes*, vol. 9, no. 3, p. 477, 2021.

APPENDICES

Appendix A: The Blade Radial Position, Chord, and Twist Angle Distribution of the 2nd Configuration

Table A.1: The Chord and Twist Distribution of the 2nd Blade Configuration.

Radial distance (m)	Radial position (r/R)	Chord (m)	Twist angle
0.25	0.05	0.7107	37.740
0.50	0.10	0.7077	25.2788
0.75	0.15	0.6420	17.5332
1.00	0.20	0.5686	12.4259
1.25	0.25	0.5028	8.8573
1.50	0.30	0.4472	6.2417
1.75	0.35	0.4010	4.2500
2.00	0.40	0.3624	2.6863
2.25	0.45	0.3301	1.4277
2.50	0.50	0.3028	0.3937
2.75	0.55	0.2794	-0.4702
3.00	0.60	0.2592	-1.2026
3.25	0.65	0.2416	-1.8312
3.50	0.70	0.2262	-2.3764
3.75	0.75	0.2126	-2.8537
4.00	0.80	0.2005	-3.2751
4.25	0.85	0.1897	-3.6497
4.50	0.90	0.1800	-3.9850
4.75	0.95	0.1712	-4.2867
5.00	1.00	0.1632	-4.5597

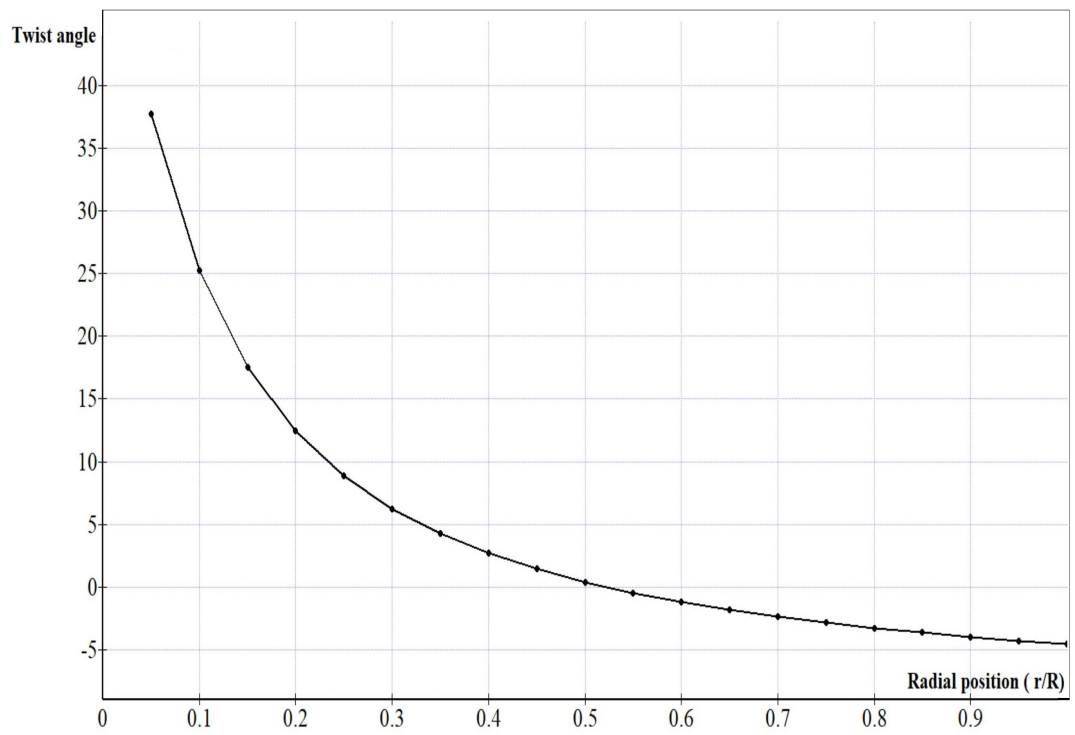
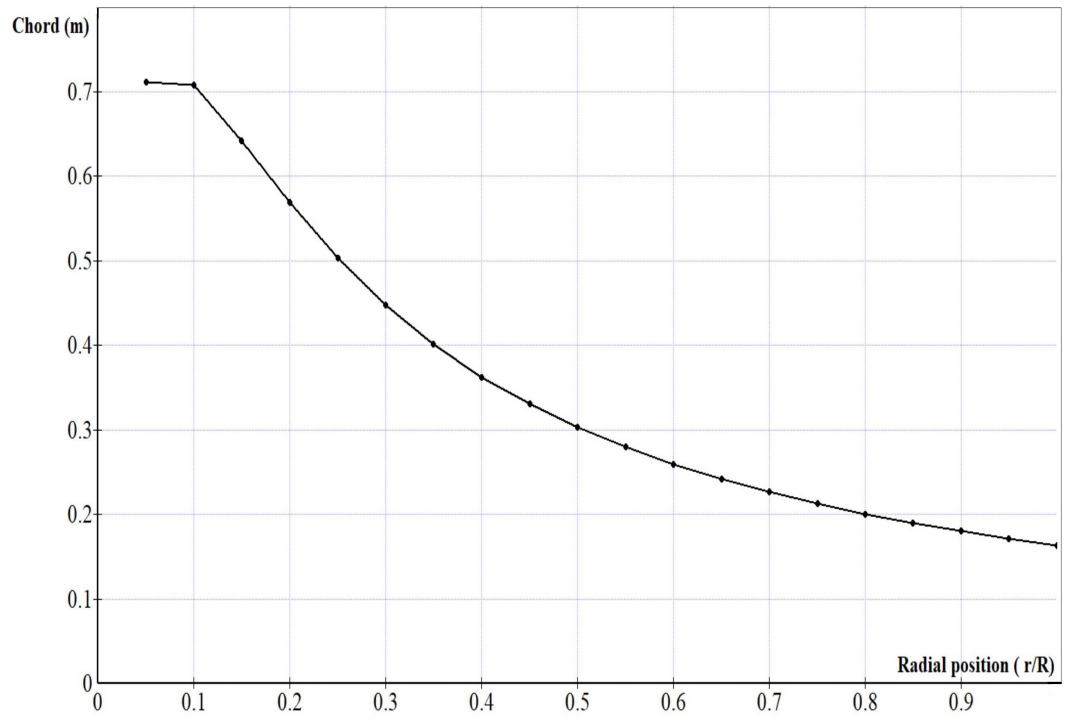


Figure A.1: The Chord and Twist Distribution of the 2nd Blade Configuration.

Appendix B: QBlade Graphical User Interface

QBlade software is based on the Blade Element Momentum (BEM) algorithm. Appendix B shows the views of the design process and results from QBlade software (version v0.963).

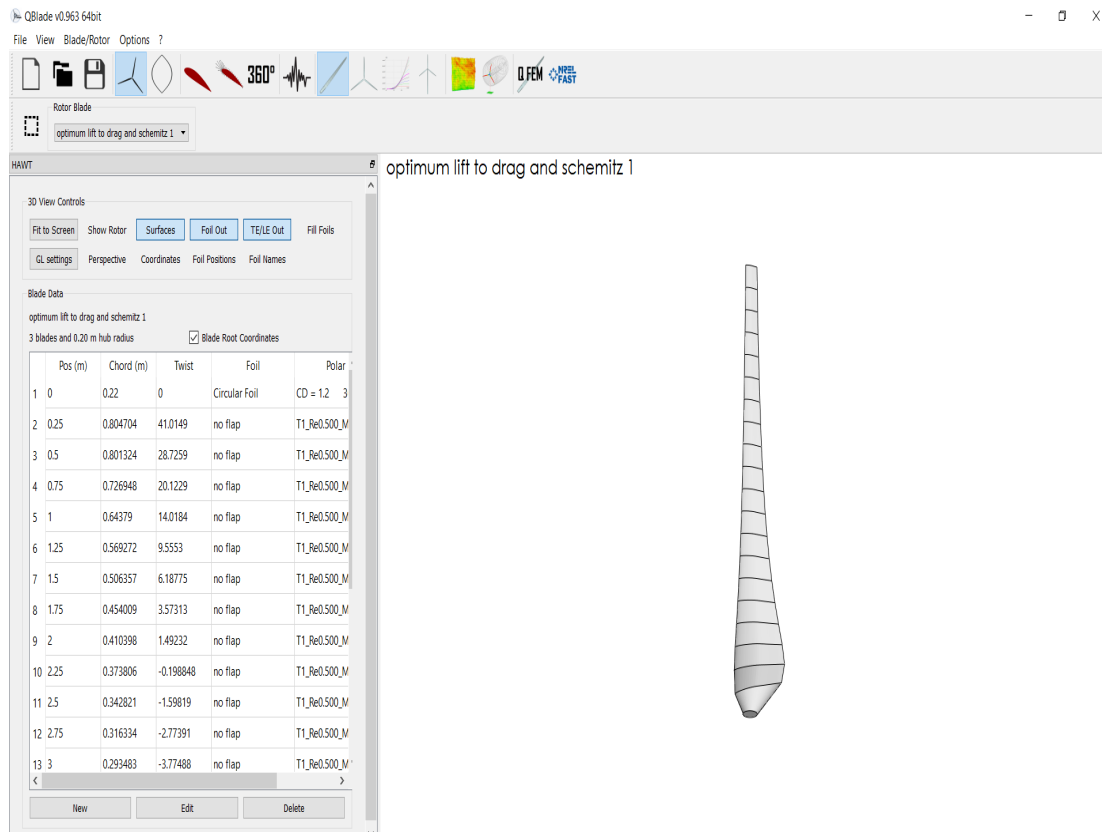


Figure B.1: Blade Design and Optimization Process.

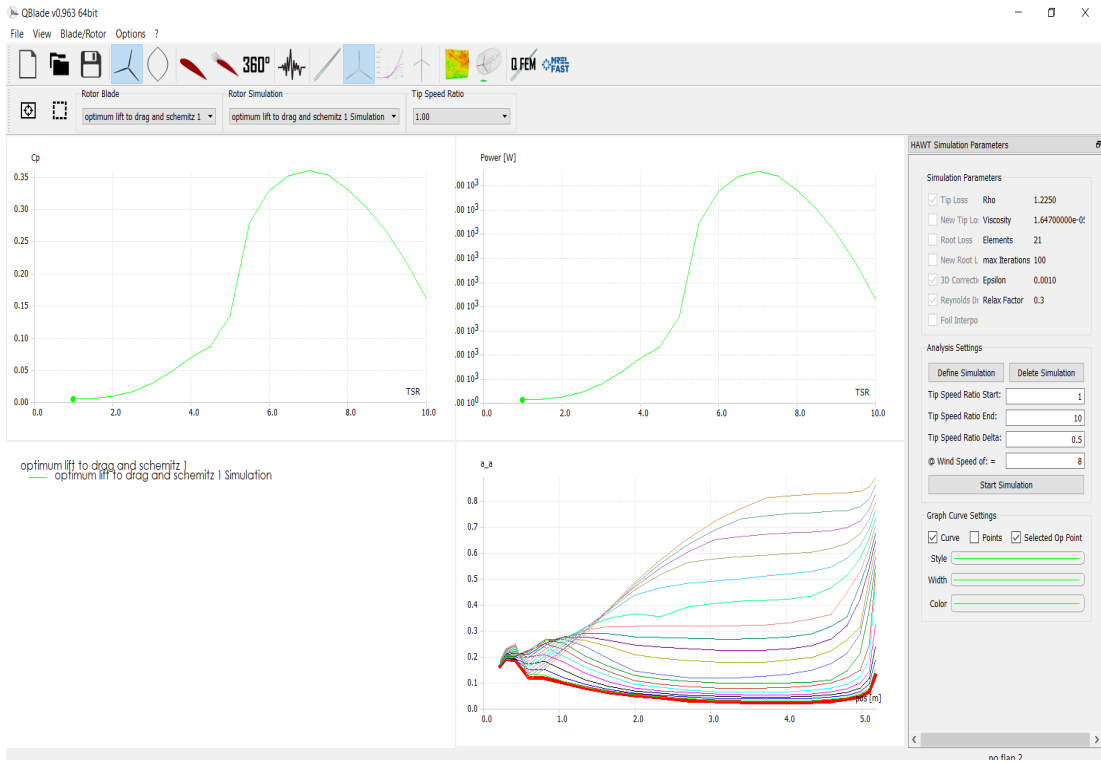


Figure B.2: Rotor BEM Simulation.

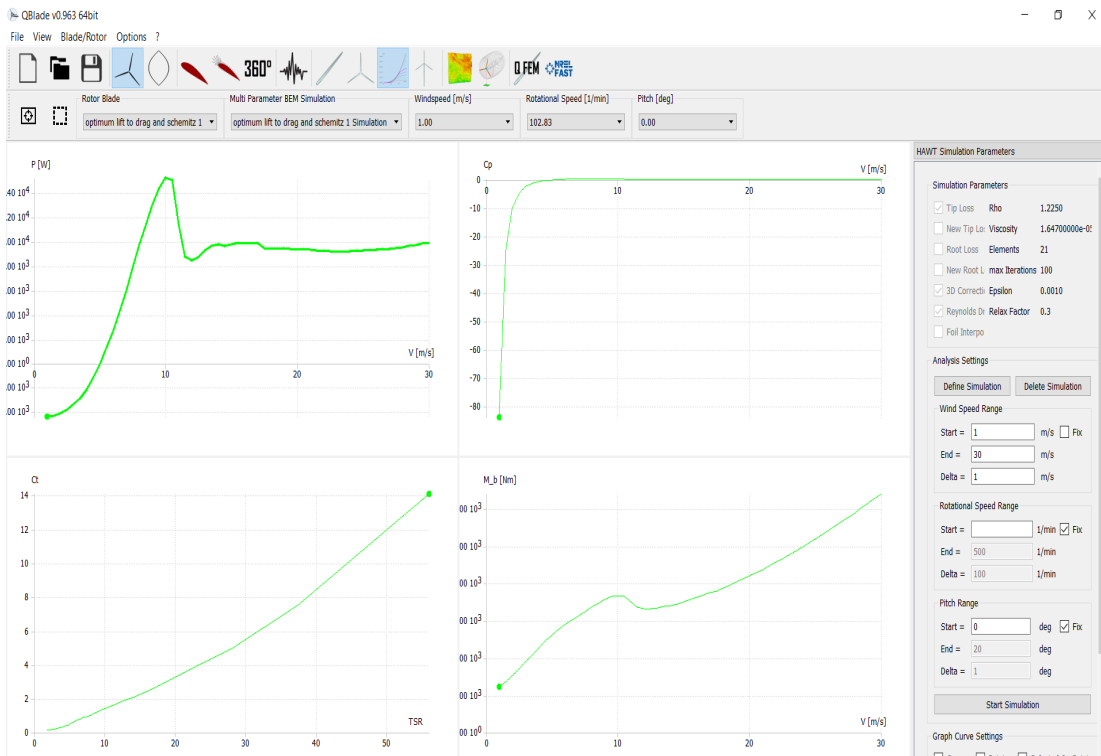


Figure B.3: Multi Parameter BEM Simulation.

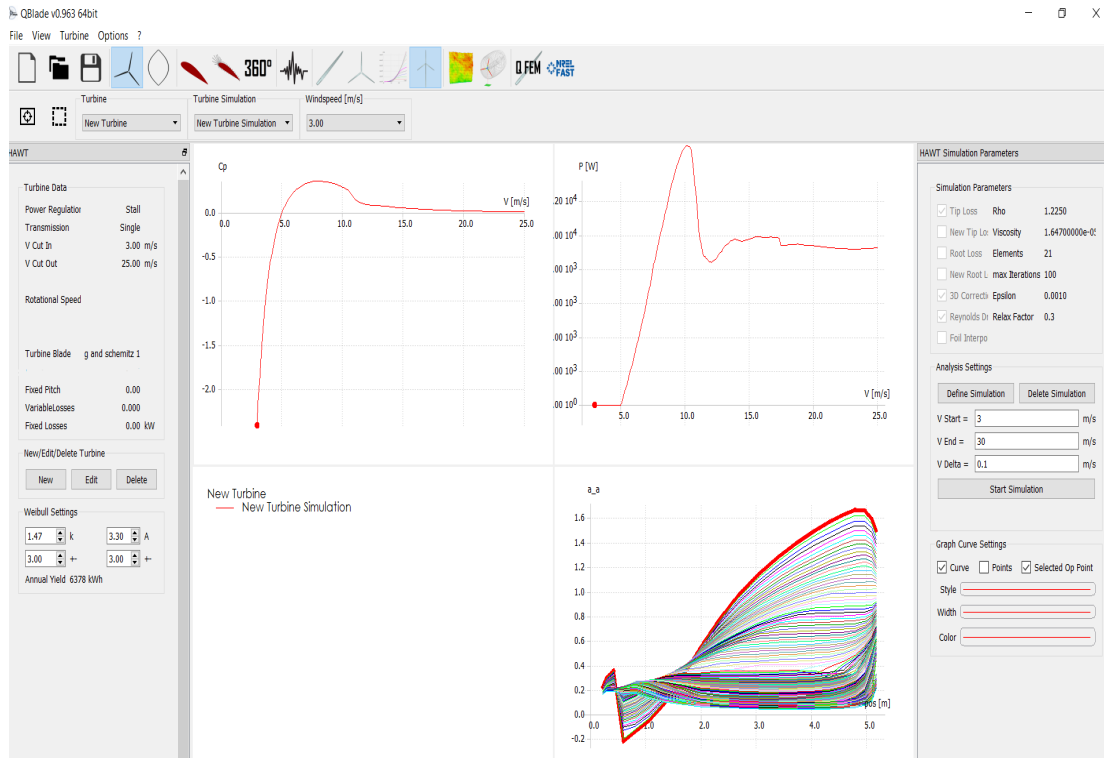


Figure B.4: Turbine BEM Simulation.

Appendix C: CFD Data Visualisation

In this appendix, more CFD data visualisation are shown. Figure C.1 shows the 2D coarse, medium and fine mesh. A solid cylindrical hub of length 0.6 m and radius of 0.2m is shown in Figure C.3.

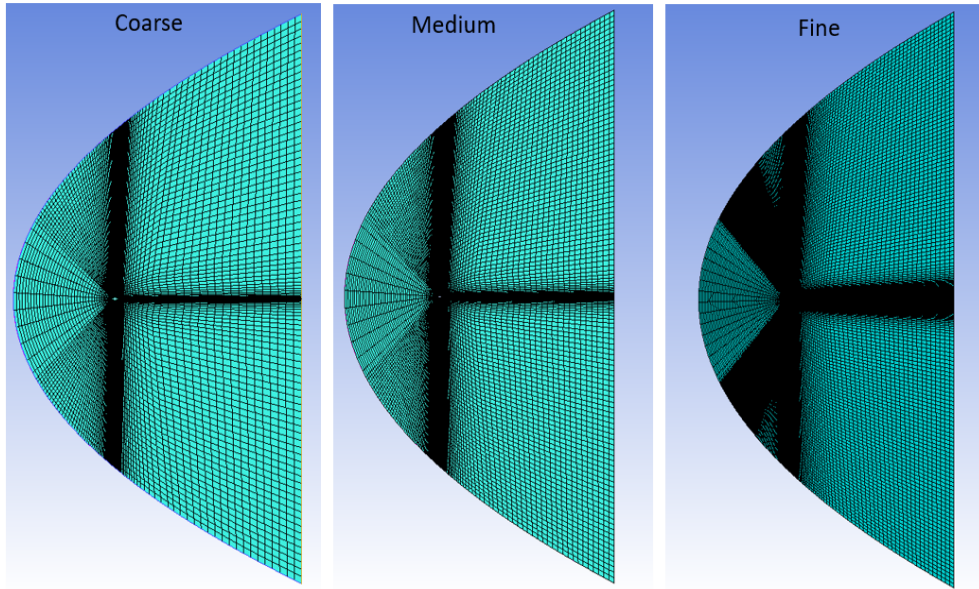


Figure C.1: 2D Coarse, Medium and Fine Mesh.

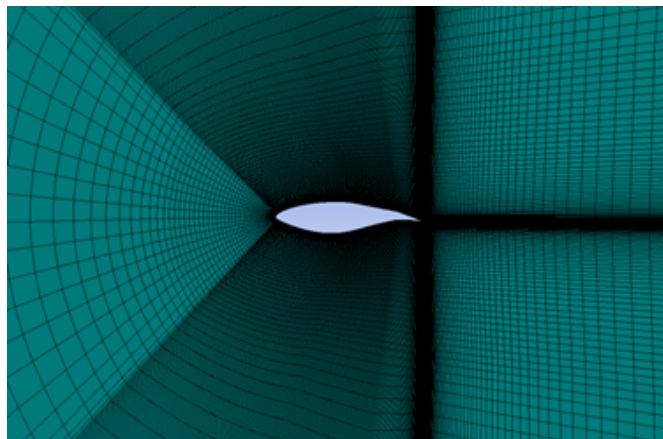


Figure C.2: Zoom View of 2D Mesh.

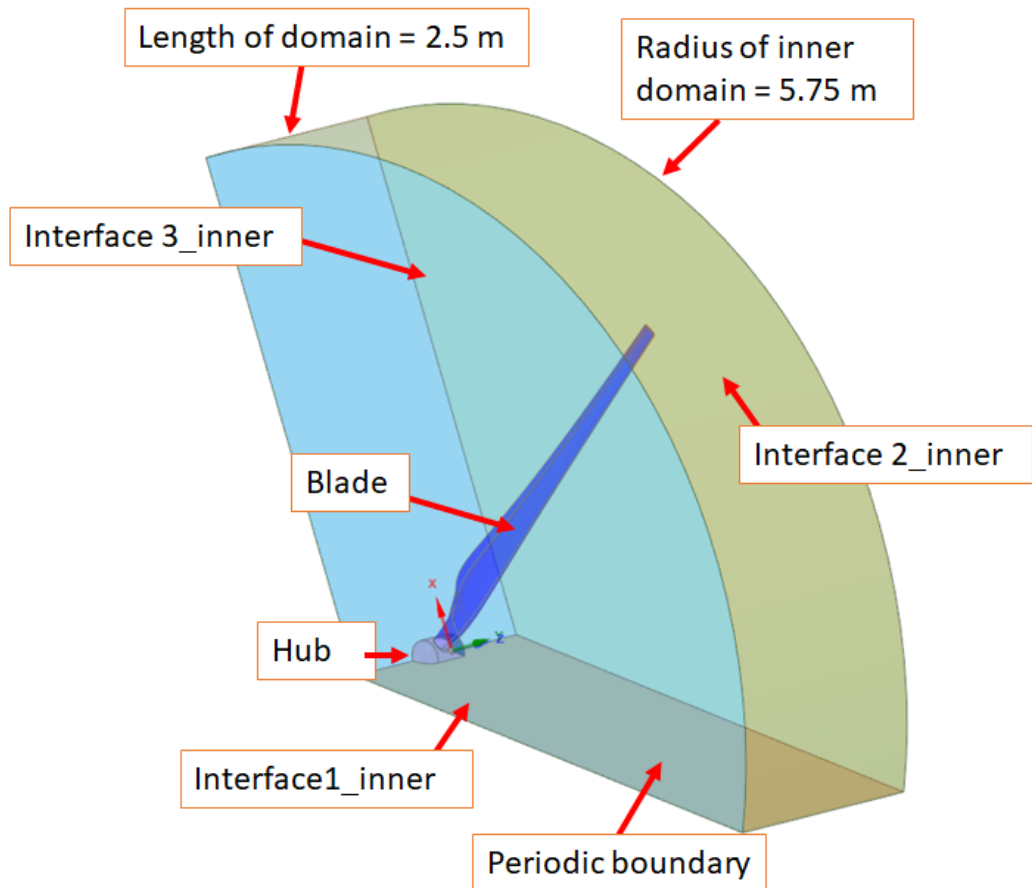


Figure C.3: Inner Domain Showing a Solid Cylindrical Hub.

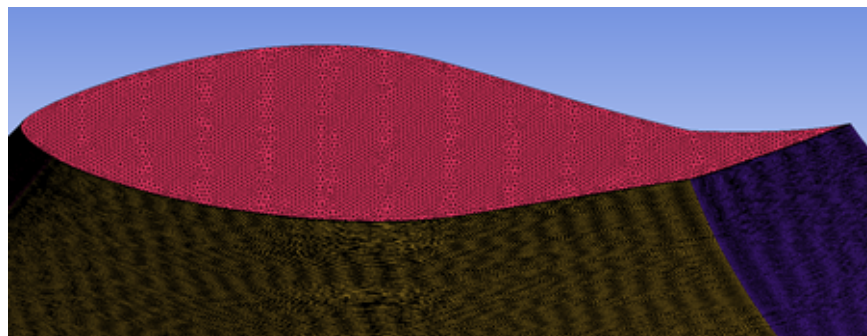


Figure C.4: Blade Mesh at the Tip.

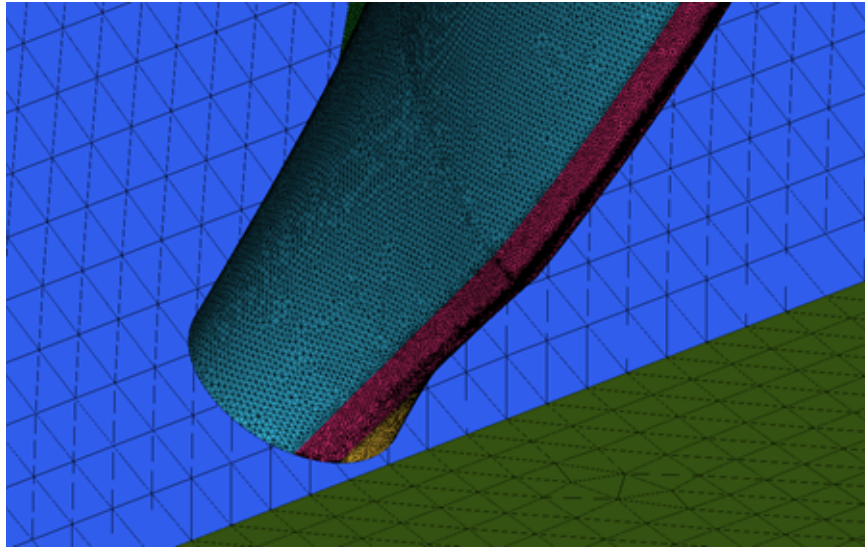


Figure C.5: Blade Mesh at the Root.

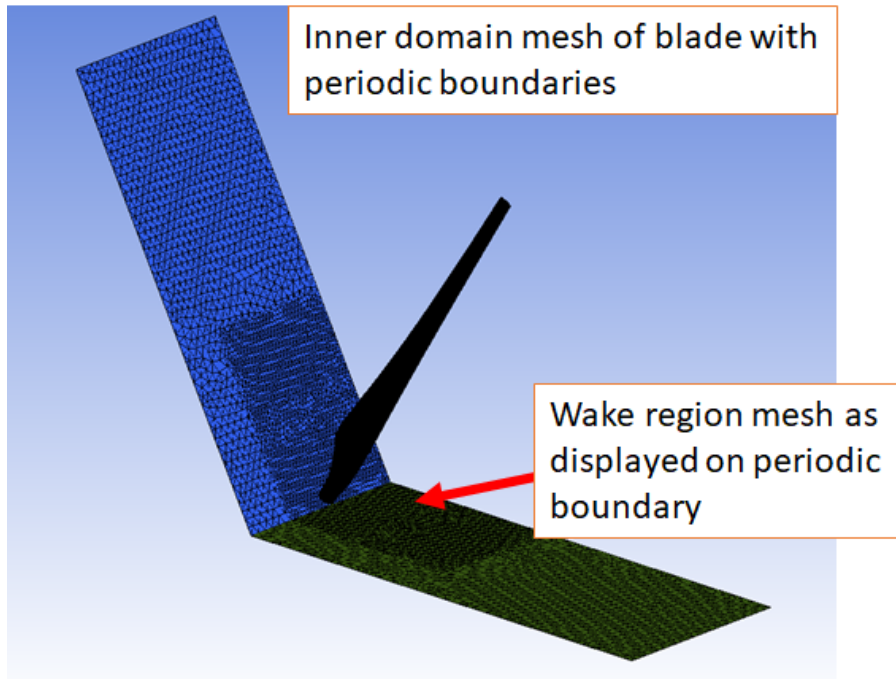


Figure C.6: The Unstructured Mesh #2 Showing the Cells Refinement at the Wake Region.

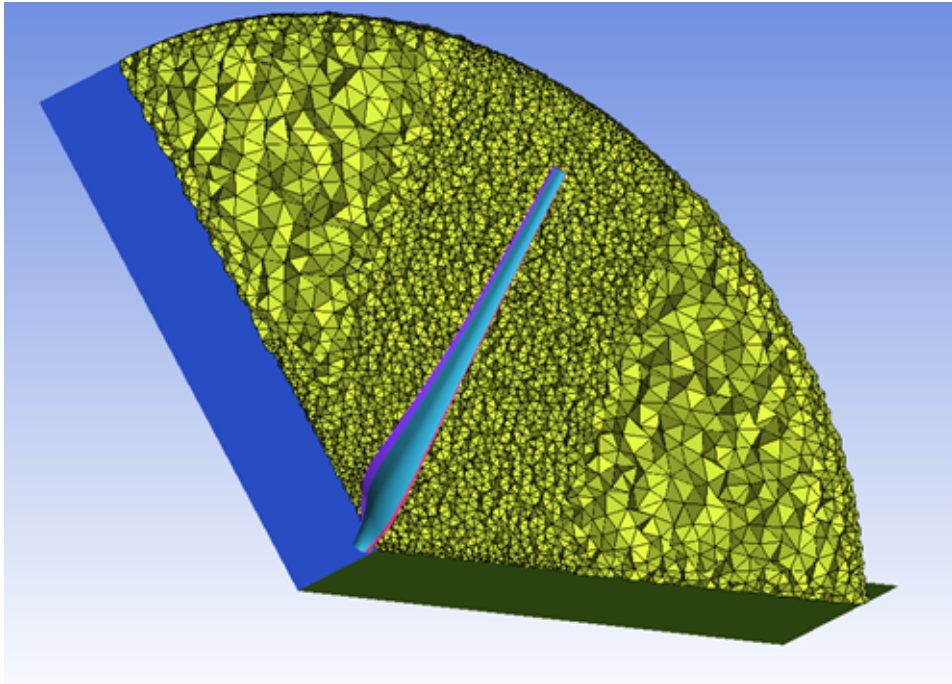


Figure C.7: A 3D Cutting Plane View in the Inner Domain.